# Journal of Electromagnetic Analysis and Applications

ISSN: 1942-0730

Volume 2, Number 9, September 2010

www.scirp.org/journal/jemaa

Scientific Research

ISSN: 1942-0730

9 771942 073001 09

# JOURNAL EDITORIAL BOARD

ISSN: 1942-0730 (Print) 1942-0749 (Online)

http://www.scirp.org/journal/jemaa

*J. Electromagnetic Analysis & Applications*, **2010, 2, 513-579**
Published Online September 2010 in SciRes (http://www.SciRP.org/journal/jemaa/)

# TABLE OF CONTENTS

**Volume 2 Number 9 September 2010**



 

# Journal of Electromagnetic Analysis and Applications (JEMAA)

# Journal Information

## SUBSCRIPTIONS

The *Journal of Electromagnetic Analysis and Applications* (Online at Scientific Research Publishing, www.SciRP.org) is published monthly by Scientific Research Publishing, Inc., USA.

### Subscription rates:

Print: $50 per issue.
To subscribe, please contact Journals Subscriptions Department, E-mail: sub@scirp.org

## SERVICES

**Advertisements**
Advertisement Sales Department, E-mail: service@scirp.org

**Reprints (minimum quantity 100 copies)**
Reprints Co-ordinator, Scientific Research Publishing, Inc., USA.
E-mail: sub@scirp.org

## COPYRIGHT



## PRODUCTION INFORMATION

For manuscripts that have been accepted for publication, please contact:
E-mail: jemaa@scirp.org

*J. Electromagnetic Analysis & Applications*, 2010, 2, 513-518
doi:10.4236/jemaa.2010.29067 Published Online September 2010 (http://www.SciRP.org/journal/jemaa)

# Analysis of Auxiliary Winding Effect on the Leakage Inductance Reduction in the Pulse Transformer Using ANSYS

**Alireza Khodakarami[1], Seyyed Mohammad Pedramrazi[2], Hassan Feshki Farahani[3]**

[1]Islamic Azad University, Shahre Ghods Branch, Tehran, Iran; [2] Islamic Azad University, Tehran North Branch, Tehran, Iran;
[3]Islamic Azad University, Ashtian Branch, Ashtian, Iran.
Email: {aqukh, m_pedram_razi, hfeshki}@yahoo.com

Received July 20th, 2010; revised August 18th, 2010; accepted August 18th, 2010

## ABSTRACT

*Several applications need high voltage and low rise time pulses that increasing of the voltage level can be done by using transformer. The rise time is increased because of transformer leakage inductance. One of the methods to decrease the rise time is using auxiliary windings between primary and secondary. In this paper, one type of pulse transformer included auxiliary windings is modeled and simulated in ANSYS software. In this study, at first the transformer has been simulated without auxiliary windings and the leakage and self inductances are obtained then the auxiliary windings are considered in the model to calculate the leakage and self inductances of the transformer. Simulation results can be used to investigate the effect of auxiliary winding on the leakage inductance.*

***Keywords*:** *Auxiliary Windings, Leakage Inductances, Finite Element Method and ANSYS*

## 1. Introduction

High-voltage pulses are often obtained from a pulse generating circuit driving a high-voltage pulse transformer. The large number of turns in the secondary windings and also insulation gap between layers of winding and windings increase the leakage inductance of pulse transformers. The rise time of high voltage pulse is depending on the leakage inductance. Many applications, such as medical, technology and military need high-voltage fast rising pulses. This requires efficient and flexible pulsed power circuits with optimization of all components [1-5]

However, if the leakage inductance in the high-voltage pulse transformer needs to be reduced, two subtractive connected windings can be added to the transformer. If these windings are fitted with the same number of turns, the electromotive force generated in the auxiliary windings is due only to the primary and secondary leakage flux. The current across them produces a magnetic field reducing only the leakage flux and, therefore, the leakage inductance in the transformer [6-8]. The most attractive winding configuration for high voltage, the core-type transformer with primary and secondary on different core legs, is seldom used in pulsed application, because of its weak magnetic coupling between windings, which would result in a slow-rising output voltage pulse. The exceptional improvement achieved in the output pulse shape of high-voltage core-type transformer, with separated primary and secondary, fitted with two auxiliary windings, for plasma immersion ion implantation applications, where almost rectangular negative high-voltage pulses are used to bias a plasma-immersed target to achieve conformal ion implantation [9].

To contribute to a better understanding of transformer operation with auxiliary windings, a mathematical model based on the theory of electromagnetic coupled circuits [10]. Alongside the new design methods [11], [12] used today to manufacture high-voltage pulse transformers using the latest materials, a common way to overcome the problems caused by parasitic elements is to use resonant topologies [12-14]. Finite element simulation is a robust method to calculation flux and inductance leakage. So a high voltage pulse transformer was modeled and simulated with ANSYS software in this paper. At first the pulse transformer is simulated without auxiliary windings and then with auxiliary

 

windings. The inductance is calculated with energy method. The simulation results show the decreasing of leakage inductance with using the auxiliary windings.

## 2. Transformer Mathematical Equations with Auxiliary Windings [9]

The structure of four windings transformer is shown in **Figure 1**.

Using the Faraday's induction law in each winding, neglecting the distributed capacitances of the windings, yields

$$v_i = R_i i_i + \frac{d\psi_i}{dt} = R_i i_i - e_i \tag{1}$$

where the subscript:

i: Refers to the index of the winding
v: The instantaneous terminal voltage
i: The instantaneous current
Ψ: The instantaneous flux linkage
e: The induced instantaneous voltage
R: The effective resistance

The average flux linkage is written as:

$$\psi_i = N_i \left( \Phi + \Phi_{ii} + \Phi_{ij} \right) \tag{2}$$

That is divided into three main components.

Φ: The resultant flux, linking all the windings
$\Phi_{ii}$ : The self-flux of the winding
$\Phi_{ij}$: The mutual flux between pairs of windings

The linkage flux for the primary winding is defined as:

$$\psi_1 = N_1 \left( \Phi + \Phi_{11} + \Phi_{12} + \Phi_{13} + \Phi_{14} \right) \tag{3}$$

The equation (3) can be rewritten as:

$$\psi_1 = N_1 \Phi + l_{11} i_1 + l_{12} i_2 + l_{13} i_3 + l_{14} l_4 \tag{4}$$

where the subscript $l_{ii}$ is Self inductance and $l_{ij}$ is Mutual inductance. According to (1) and (3) the instantaneous terminal voltage at primary winding is the sum of the winding resistance voltage drop, the induced electromotive force due to the time varying resultant flux, and induced electromotive forces associated with the self and mutual leakage fluxes.

$$v_1 = R_1 i_1 + N_1 \frac{d\Phi}{dt} + l_{11} \frac{di_1}{dt} + l_{12} \frac{di_2}{dt} + l_{13} \frac{di_3}{dt} + l_{14} \frac{di_4}{dt} \tag{5}$$

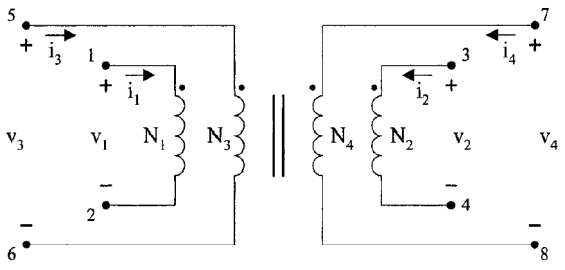


**Figure 1. The circuit of mathematical model of a transformer with four windings [9].**

As shown in **Figure 2**, the auxiliary windings of transformer are connected in subtractive mode (terminals 5 and 6 are connected to terminals 7 and 8, respectively). Considering that $i_4 = -i_3 = i_{aux}$ and $v_3 = v_4$ in **Figure 2**, applying to (5) and taking into consideration that $N_3 = N_4 = N_{aux}$, yields,

$$v_1 = R_1 i_1 + N_1 \frac{d\Phi}{dt} + l_{11} \frac{di_1}{dt} - l_{12} \frac{di_o}{dt} + (l_{14} - l_{13}) \frac{di_{aux}}{dt} \tag{6}$$

Also Equations (7) to (9) for other three windings are derived like Equation (6) respectively.

$$v_2 = -R_2 i_o + N_2 \frac{d\Phi}{dt} + l_{21} \frac{di_1}{dt} - l_{22} \frac{di_o}{dt} + (l_{24} - l_{23}) \frac{di_{aux}}{dt} \tag{7}$$

$$v_3 = -R_3 i_{aux} + N_{aux} \frac{d\Phi}{dt} + l_{31} \frac{di_1}{dt} - l_{32} \frac{di_o}{dt} + (l_{34} - l_{33}) \frac{di_{aux}}{dt} \tag{8}$$

$$v_4 = R_4 i_{aux} + N_{aux} \frac{d\Phi}{dt} + l_{41} \frac{di_1}{dt} - l_{42} \frac{di_o}{dt} + (l_{44} - l_{43}) \frac{di_{aux}}{dt} \tag{9}$$

In this connection $v_3 = v_4$ which yields

$$(l_{31} - l_{41}) \frac{di_1}{dt} + (l_{42} - l_{32}) \frac{di_o}{dt} = R_{aux} i_{aux} + l_{aux} \frac{di_{aux}}{dt} - M_{aux} \frac{di_{aux}}{dt}$$

$$R_{aux} = R_2 + R_4 \qquad l_{aux} = l_{33} + l_{44} \qquad M_{aux} = l_{34} + l_{43} \tag{10}$$

The current across the auxiliary windings is ruled by (10). It is interesting to observe that $i_{aux}$ is independent of the time derivative of the resultant flux, Φ. If the auxiliary windings have the same number of turns, $i_{aux}$ exists only as the consequence of the leakage coupling between the primary and secondary leakage flux linking the auxiliary windings.

The auxiliary current, $i_{aux}$ function of the leakage flux coupling between the primary and secondary with the third and fourth windings, generates a magnetic flux that reduces the

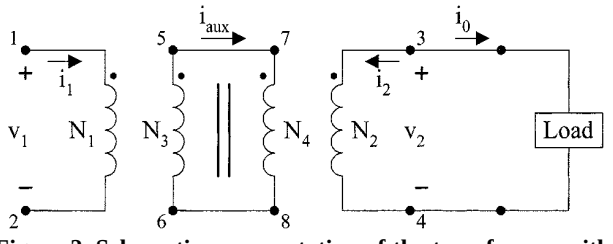


**Figure 2. Schematic representation of the transformer with loaded secondary, $N_2$ and the two auxiliary windings connected in subtractive mode $N_3$ and $N_4$ [9].**

 

leakage flux of the primary and secondary windings. Consequently, the leakage inductance in the transformer is reduced. The resultant flux, Φ, is not affected by the auxiliary windings.

## 3. Finite Element Analysis of Transformer

To evaluate the effects of auxiliary windings on the leakage inductances reduction, a pulse transformer with auxiliary windings is modeled in ANSYS software. ANSYS is a finite element analysis (FEA) code widely used in the computer-aided engineering (CAE) field. It is powerful software to analyze the magnetic energy with finite element method. The leakage and magnetic inductances are function of the stored energy in the window of pulse transformer and in the core of pulse transformer respectively. The current density is needed to simulate the magnetic and leakage flux of pulse transformer (as loads). So the current density is applied to windings area. The potential is equal to zero in boundary and it is considered as boundary condition. At first the pulse transformer is simulated without using the auxiliary windings and then the auxiliary windings is considered in simulation to reach desired results.

The pulse transformer modeled in ANSYS is shown in **Figure 3**. Primary winding includes two 25 turns' layers in window of pulse transformer. The dimension of each layer of primary winding is 34 mm × 1.5 mm. The line spacing between two layers is 0.1 mm that the electric insulation is found in this space. The line spacing between the primary and third windings is 0.1 mm and it is 0.1 mm between the third winding and the main leg of the pulse transformer.

The secondary winding is 500 turns in eight layers. The line spacing between secondary and auxiliary (forth) windings is 0.1 mm. The width of each layer of secondary winding is 0.5 mm and because the layers length isn't equal so the mean length of layers is 25 mm.

Two auxiliary windings, with 25 turns in one layer, are shown in **Figure 3**. The length of third auxiliary winding is 34 mm and its width is 0.5 mm. The dimension of forth winding is the same as third winding. Core type of pulse transformer is ferrite (high frequency) with 10 kHz nominal frequency. The B-H curve of ferrite core is shown in **Figure 4**.

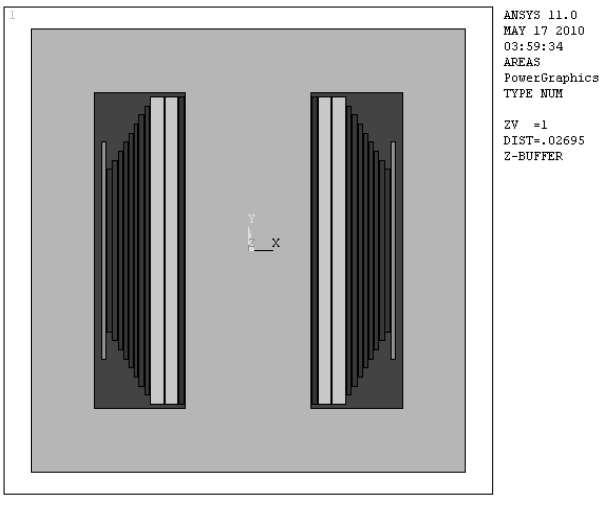


**Figure 3. The model of pulse transformer with auxiliary windings.**

## 4. Simulation of Pulse Transformer without the Auxiliary Windings

The leakage inductances of primary and secondary windings are calculated without the effects of auxiliary windings. The energy method is used to calculate leakage inductance that is explained in following.

### 4.1. Calculation of Magnetic and Leakage Inductances of the Primary Winding

In this case, the current density is just applied to primary winding, and then the magnetic stored energy in the pulse transformer is obtained.

The stored magnetic energy in the transformer is shown in **Figure 5**. According to this figure, the total stored energy in the transformer is equal to 104.348 J for one meter of depth. But the depth of the modeled transformer is 0.007m, so the total stored energy in transformer is 0.730436J (104.348 × 0.007). Distribution of magnetic energy in each element of the core is shown in **Figure 6**. Also by attention to this figure, the total stored energy in the core is 104.319J for 1 meter of depth and so for 0.007 m of depth, the stored energy will be 0.730233J. The self primary inductance can be obtained from Equation (11).

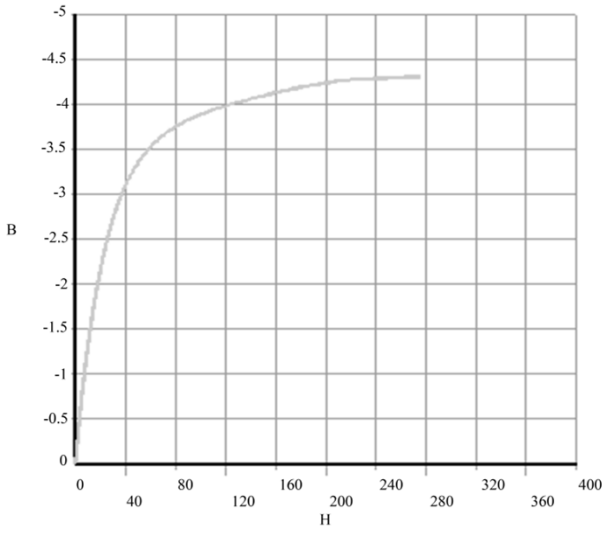


**Figure 4. ferrite core B-H curve of pulse transformer.**

 

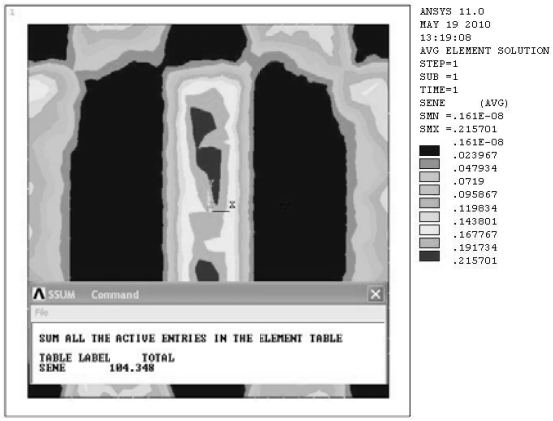


**Figure 5. The energy distribution in the whole model elements and total magnitude of saved energy.**

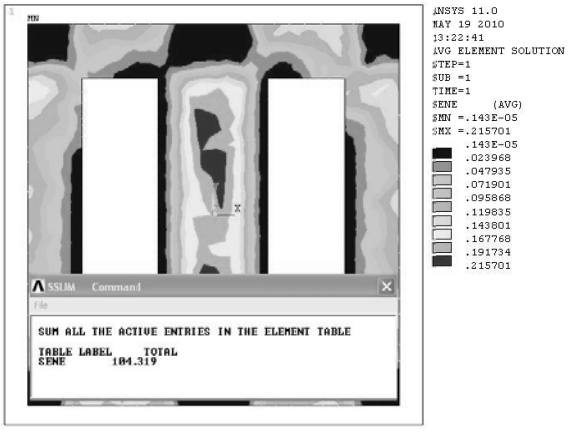


**Figure 6. The energy distribution in the core elements and magnitude of saved energy (just core).**

$$L = \frac{2W}{i^2} \tag{11}$$

Leakage inductance can be calculated by using the difference between the stored energy in the transformer and the core.

$$\begin{aligned} W_{total} &= 0.730436J \\ W_{core} &= 0.730233J \\ W_{lekage} &= W_{total} - W_{core} = \\ 0.730436 &- 0.730233 = 0.203mJ \end{aligned} \tag{12}$$

The leakage energy is 0.203mJ for 7 mm depth. According to Equation (11), the leakage and self inductances are equal to 1.8 μH and 6.5 mH respectively.

### 4.2. Calculation of Magnetic and Leakage Inductances of Secondary Winding

Similar to primary winding, the transformer and core stored energy are obtained from simulation and the secondary self and leakage inductances are calculated that they are 645mH and 273 μH respectively. The self and leakage inductances of primary and secondary windings without auxiliary windings are listed in **Table 1**.

## 5. Simulation of Primary Winding with Third Auxiliary Winding

In this case, the auxiliary windings are connected in deferential mode and the inductances are obtained.

### 5.1. Simulation of Primary Winding of Pulse Transformer with Third Auxiliary Winding

To simulate the flux leakage of pulse transformer with auxiliary windings, two current densities are applied to primary and third auxiliary winding, then the stored energy in transformer and the core is obtained which is shown in **Figure 7** and **Figure 8** respectively.


**Figure 7. Distribution and total magnitude magnetic energy in depth unit of model.**


**Figure 8. Distribution and magnitude saved energy in core at unit depth.**

 

**Table 1. The magnetic and leakage inductances of primary-secondary windings without auxiliary windings.**

| winding | Self inductance | Leakage inductance |
|---|---|---|
| primary | 6.5 mH | 1.8 μH |
| secondary | 645 mH | 273 μH |

The energy stored in the transformer and core for 1 m depth are 103.217 J and 103.195 J respectively which for the 0.007 m of core depth are 0.722519 J and 0.722365 J respectively. Using the stored energy value and Equation (11), the self primary inductance is 6.42 mH and the leakage inductance is 1.37 μH.

### 5.1. Simulation of Secondary Winding of Pulse Transformer with Forth Auxiliary Winding

The current direction of auxiliary windings is opposite to main windings (primary and secondary winding), so the direction of the current density in secondary winding is opposite to that of the forth auxiliary winding. As a result, the opposite flux density of forth auxiliary winding is the main reason of flux density reduction of secondary winding that it leads to the leakage inductance reduction. The self inductance of secondary winding is calculated equal to 640 mH, and also total leakage energy in this case is 0.000217 J. Therefore, the leakage inductance is obtained equal to 193 μH. The self and leakage inductances of pulse transformer with auxiliary winding is shown in **Table 2.**

## 6. Conclusions

In this paper, the effect of auxiliary windings used in a pulse transformer is investigated. The auxiliary windings were placed in proximity of primary and secondary windings. It has been shown that the auxiliary current, $i_{aux}$ function of the leakage flux coupling between the primary and secondary with the third and fourth windings, generates a magnetic flux that reduces the leakage flux of the primary and secondary windings. Consequently, the leakage inductance in the transformer is reduced. The resultant flux, Φ, is not affected by the auxiliary windings. To this aim, a pulse transformer with auxiliary windings was modeled in ANSYS software. At first, the simulation has done without using of auxiliary windings and then the auxiliary windings were added to the transformer model. By using the obtained result from the first case (without auxiliary windings), the primary and secondary leakage inductances are calculated equal to 1.8 μH, 273 μH respectively. In second case (with auxiliary windings), the primary and secondary inductances are reduced to 1.36 μH, 193 μH respectively. The result shows that the self inductances don`t considerably change in two cases of simulations.

**Table 2. The magnetic and leakage inductances of primary-secondary windings with auxiliary windings.**

| Winding | Self inductance | Leakage inductance |
|---|---|---|
| Primary(with third) | 6.42 mH | 1.36 μH |
| Secondary(with forth) | 640 mH | 193 μH |

## 7. Acknowledgements

This paper is extracted from the research project as title: "Design, Simulation and Construction of Low Rise Time High-Voltage Pulse Transformers Using Auxiliary Windings" in Islamic Azad University, Shahre Ghods Branch.

## REFERENCES

[1] Y.-H. Chung and C.-S. Yang, "All Solid-State Switched Pulser for NO Control," 36*th* *IEEE Industry Applications Conference*, 30 September-4 October 2001, Vol. 4, 2001, pp. 2533-2540.

[2] N. Grass, W. Hartmann and M. Romheld, "Microsecond Pulsed Power Supply for Electrostatic Precipitators," 36*th* *IEEE Industry Applications Conference*, 30 September-4 October 2001, Vol. 4, 2001, pp. 2520-2524.

[3] J. Jethwa, E. E. Marinero and A. Muller, "Nanosecond Rise Time Avalanche Transistor Circuit for Triggering a Nitrogen Laser," *Review of Scientific Instrument*, Vol. 52, No. 7, 1981, pp. 989-991.

[4] M. P. J. Gaudreau, T. Hawkey, J. Petry and M. A. Kempkes, "A Solid State Pulsed Power System for Food Processing," *Pulsed Power Plasma Science*, Digital Techniques Papers, Vol. 2, 2001, pp. 1174–1177.

[5] Y. C. Cheng, K. Ping, X. Tian, X. Wang, B. Tang and P. Chu, "Special Modulator for High Frequency, Low- Voltage Plasma Immersion Ion Implantation," *Review of Scientific Instrument*, Vol. 70, No. 3, 1999, pp. 1824-1828.

[6] A. M. Pernía, J. M. Lopera, M. J. Prieto and F. Nuño, "New Family of ZVS QRC and MRC with PWM Control Based on Magnetic Elements Modification," *European Power Electronics EPE Journal*, Vol. 8, No. 12, 1999, pp. 25-32.

[7] A. M. Pernía, J. M. Lopera, M. J. Prieto and F. Nuño, "Analysis and Design of A New Constant Frequency Control for QRC and MRC Based on Magnetic Elements Modification," *IEEE Transactions Power Electronics*, Vol. 13, No. 2, 1998, pp. 244-251.

[8] L. M. Redondo, E. Margato and J. F. Silva, "Low-Voltage Semiconductor Topology for Kv Pulse Generation Using a Leakage Flux Corrected Step-Up Transformer," *Proceedings of IEEE Power Electronics Specialists Conference*, 2000, pp. 326-331.

[9] L .M. Redondo, E. Margato and J. F. Silva, "Rise Time Reduction in High-Voltage Pulse Transformer Using Auxiliary Windings," *IEEE Transactions Power Electronics*, Vol. 17, No. 2, 2002, pp. 196-206.

[10] L. M. Redondo, J. F. Silva and E. Margato, "Pulse Shape Improvement in Core-Type High-Voltage Pulse Trans-

 

formers with Auxiliary Windings," *IEEE Transactions Magnetics*, Vol. 43, No. 5, 2007, pp. 1973-1982.

[11] M. H. Kheraluwala, D. W. Novotny and D. M. Divan, "Coaxial Wound Transformers for High-Power High-Frequency Applications," *IEEE Transactions Power Electronics*, Vol. 7, No. 1, 1992, pp. 54-62.

[12] M. García, C. Viejo, M. Secades and J. González, "Design Criteria for Transformers in High Voltage Output, High Frequency Power Converter Application," *European Power Electronics EPE Journal*, Vol. 4, No. 4, 1994, pp. 37-40.

[13] J. Kein and M. Padberg, "A Modular Low-Cost, High-Voltage Pulse Generator that is Highly Effective in Terms of Pulse Energy and Repetition Frequency," *Measurement Science Technology*, Vol. 6, No. 5, 1995, pp. 550-553.

[14] J. M. Sun, S. P. Wang, T. Nishimura and M. Nakaoka, "Resonant Mode PWM DC-DC Converter with a High-Voltage Transformer-Link and its Control Methods for Medical-Use X-Ray Power Supply," *Proceedings of 8th European Conference of Power Electronics Applicant*, Lausanne, Switzerland, 7-9 September 1999, Proc. on CD-ROM.

 

*J. Electromagnetic Analysis & Applications*, 2010, 2, 519-528
doi:10.4236/jemaa.2010.29068 Published Online September 2010 (http://www.SciRP.org/journal/jemaa)

# Beam Dynamics and Electromagnetic Design Studies of 3 MeV RFQ for SNS Programme

**Rahul Gaur, Purushottam Shrivastava**

Raja Ramanna Centre for Advanced Technology, Indore, India
Email: rahul@rrcat.gov.in

Received June 30th, 2010; revised August 13th, 2010; accepted August 13th, 2010

## ABSTRACT

*The physics design of a* 3 *MeV*, 30 *mA*, 352.2 *MHz Radio Frequency Quadrupole* (*RFQ*) *is done for the future Indian Spallation Neutron Source* (*ISNS*) *project at RRCAT, India. The beam dynamics design of RFQ and the error analysis of the input beam parameters are done by using standard beam dynamics code PARMTEQM. The electromagnetic studies for the two-dimensional and three-dimensional cavity design are performed using computer codes SUPERFISH and CST Microwave Studio. The physics design of RFQ consisting of the beam dynamics design near the beam axis and the electromagnetic design for the RFQ resonator is described here.*

***Keywords*:** *Radio Frequency Quadrupole* (*RFQ*), *Beam Dynamics, Error Analysis, Cavity Design, End-Cells Optimization*

## 1. Introduction

A 1 GeV proton synchrotron facility is envisaged for ISNS (Indian Spallation Neutron Source) project at RRCAT, India. The front-end 100 MeV linac will serve as an injector to the synchrotron facility. Presently RRCAT is building a low energy front-end upto 3 MeV as a first phase development for the linac. Being very much efficient accelerator for ions in low energy region, Radio Frequency Quadrupole (RFQ) [1,2] is one of the main components in the front-end system which accelerates 30 mA beam current of $H^-$ particles at 50 keV from ion source to 3 MeV. A special feature of RFQ is that it adiabatically bunches, strongly focuses and efficiently accelerates the charged particles simultaneously with the help of RF electric field set inside.

The design specifications of the RFQ are listed in **Table 1.**

To meet the demand for 20 mA beam current in the synchrotron, the RFQ is decided to be designed for 30 mA. The choice of higher frequency is preferred from rf power economy point of view because of the improved shunt impedance at higher frequencies due to reduction in cavity dimensions. But the power dissipation capability of the structure is higher for low frequency structures. Additionally the machining and alignment tolerances become too stringent at higher frequencies. Requirement from spallation neutron source leads to the choice of injector linac and hence RFQ to be operated in pulsed mode. The RFQ is decided to be pulsed with the duty factor of 1.25%, hence, the constraint of higher power dissipation capability of the structure can be relaxed in pulsed operation. Considering these facts as well as due to the availability of high power RF sources, the operating frequency of RFQ is selected to be 352.2 MHz. The structure of RFQ is selected to be four-vane type because of higher efficient at higher frequency.

We have followed the generalized method of RFQ beam dynamics proposed by LANL in which the RFQ is divided in four sections namely Radial Matching Section (RMS), Shaper Section, Gentle Bunching (GB) Section

**Table 1. The design specifications of the RFQ.**

| Parameters | Value | |
|---|---|---|
| Input Energy | 50 | keV |
| Output Energy | 3 | MeV |
| Beam Current | 30 | mA |
| Particle | $H^-$ | |
| Operating Mode | Pulsed | |
| Duty Factor | 1.25% | |
| Pulse Length | 500 | μs |
| Repetition Rate | 25 | Hz |
| Frequency | 352.2 | MHz |
| Structure | 4-vane type | |

 

and Accelerating Section. The various studies which were performed for the design of the RFQ are described in the following sections.

## 2. Beam Dynamics Design

The beam dynamics design of an RFQ is performed keeping in view a given ion species, input energy, beam current and emittances, operating frequency, inter-electrode voltage, through choosing proper dynamics parameters, to reach the requirement of output energy, beam current and emittances. The beam loss control and the minimization of the emittance growth are considered to be the main issues while optimizing the linac configuration and the operating parameters.

The input normalized root mean square (rms) emittance of beam from ion source is taken as 0.02 π cm-mrad. The initial particle distribution is selected to be 4-D Waterbag for which total emittance is equal to 6 times the total, normalized rms emittance.

Various RFQ design parameters are optimized and the effects of space charge, image charge and multipole terms of electric potential are also included in the calculation with the help of standard code PARMTEQM [3] for maximum transmission efficiency with minimum emittance growth. The variation of RFQ beam dynamics parameters along the length of RFQ is shown in **Figure 1**. The beam dynamics design for the ion beam, *i.e.* the design of the shape of the RFQ electrodes, results in a continuous change of aperture, vane modulation and cell length along the RFQ.

Intervane voltage is one of the very important parameters for the design and reliable working of RFQ. Higher intervane voltage results in higher energy gain, shorter cavity and better performance, but on the other hand it requires more RF power and face the danger of RF sparking. So the maximum vane voltage is decided by the Kilpatrick Criterion. In this design the peak electric field is limited to 1.7 times the Kilpatrick criterion. The intervane voltage is kept constant at 79.97 kV along the structure, so that adjusting the field distribution along the length will be easier [4,5].

Our RFQ design starts with an adiabatic radial matcher which transforms the dc input beam into a radially time-varying beam matched to the FODO focusing structure of the time-varying quadrupole field in the RFQ. In this design, the radial matching section (RMS) occupies six cells, each of length $\beta\lambda/2 = 0.4391$ cm, where $\beta=v/c$ is the ratio of the particle velocity v to speed of light in vacuum c and λ is the free space rf wavelength; hence the total length of RMS is 2.6346 cm. In the RMS, the focusing strength 'B' is brought up from zero by ramping the vane tip radius '$a$' from large value down to average radius '$r_0$' = 0.3495 cm without modulation (m=1). The synchronous phase '$\varphi_s$' is kept constant at $-90^0$, for which the separatrix has the largest phase width and the longitudinal acceptance is maximum.

In the RFQ, the next is the shaper section, following the RMS, which contains 75 cells. In the shaper section, the bunching process is initiated with a slow increase of stable phase from $-90^0$ to $-83^0$ and with a slow increase of

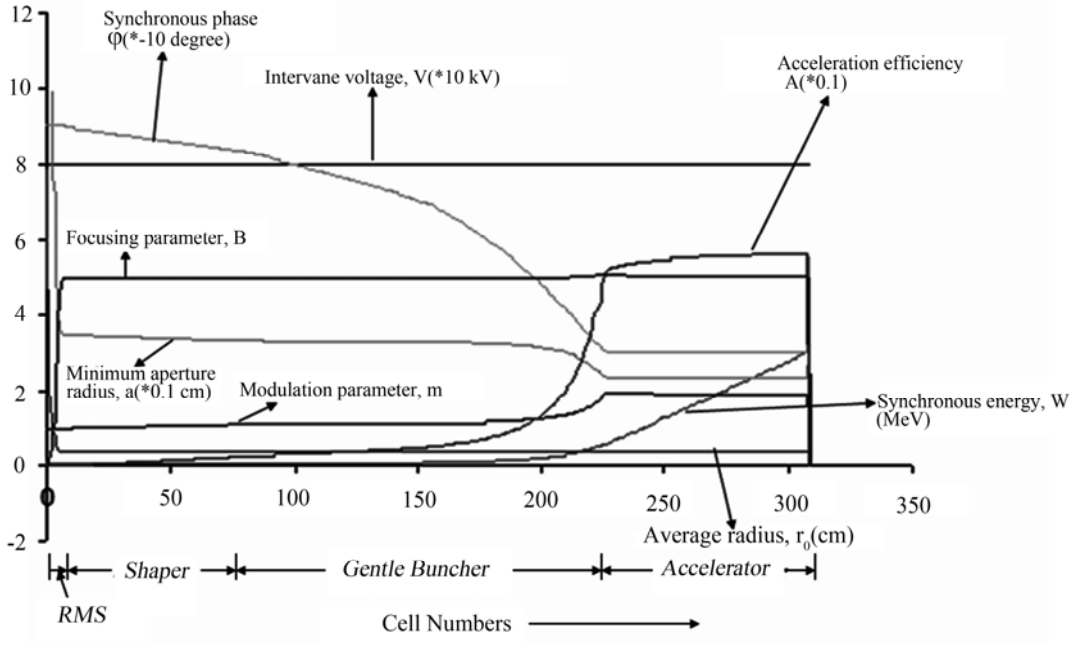


**Figure 1. Variation of parameters along the length of RFQ.**

 

modulation parameter 'm' from 1 to 1.1142 which increases the acceleration efficiency 'A' from zero (in the RMS) to 0.026. The energy of synchronous particle is slowly increased from 50 keV to 55 keV.

Downstream to shaper section, there is 145 cells long gentle buncher (GB) section which adiabatically bunch the beam. In the GB, longitudinal electric field, '$E_z$' is turned on gradually by increasing the modulation index 'm' in a controlled fashion. The stable phase is gradually then increased to $-30^0$ and the modulation is increased to 1.9523. In the GB section, the parameters are chosen such as to keep bunching as well as to keep a nearly constant charge density for reducing the effect of space-charge. The beam is brought to 560 keV and fully bunched at the end of GB section. The most critical point in the RFQ is the end of the buncher section where the beam energy is not significantly higher than at injection, but the bunch charge density is highest. This results in maximum space-charge force on the beam at the end of GB; therefore the aperture is reduced to its minimum value to have the maximum focusing strength.

After matching radially and longitudinally, the ion beam enters the accelerating section consisting of 81 cells. Here, synchronous phase '$\varphi_s$', modulation 'm' and focusing parameter 'B' are kept nearly constant for high accelerating efficiency and to reach the final accelerating energy of 3 MeV.

After the accelerating section a transition cell of length 2.9083 cm is included. The purpose of the transition region is to end the RFQ vane tips with quadrupole symmetry, which eliminates the nonzero axial potential (and hence accelerating field) at the end of the RFQ vanes. Particles experience no energy change after the end of the vanes because there is no modulation (m = 1) in this region. The transition region also provides a convenient way to control the orientation of the output transverse phase-space ellipses, which eases matching the beam into a following accelerating structure or focusing channel.

Following the transition region, an exit fringe-field region is also included. The most important function of the exit fringe-field region is to provide a well-defined geometry at the end of the RFQ, where the RF fields are known and can be included in the beam-dynamics simulation by PARMTEQM. The fringe-field region consists of one cell having length 1.118 cm and also serves as a radial matching section at the end of the RFQ. This also insures the transport of the beam through the transverse RF focusing fields that exist in this region.

The average radius, '$r_0$', and the vane tip transverse radius of curvature, 'ρ' are kept constant for the ease of mechanical fabrication; and the ratio of the vane tip transverse radius of curvature to the average radius, '$\rho/r_0$', is kept constant to maintain a constant capacitance per unit length along the axis of RFQ [6,7].

The total 309 cells of all sections are combined to give the total length of 346.6316 cm for RFQ.

The main design parameters of this RFQ are listed in **Table 2**. In this table '$\varepsilon_{x,y,rms,n}$' is representing the transverse normalized rms emittances and '$\varepsilon_{z,rms,n}$' stands for the longitudinal normalized rms emittance. **Figures 2 and 3** show the beam simulation results by PARMTEQM.

In the PARMTEQM, 10000 macroparticles are simulated and observed the dynamics along the length of RFQ. With the input transverse normalized rms emittance of $0.02\pi$ cm-mrad of beam, the output emittance is found to grow by less than 14% and the transmission efficiency of 98% with 10000 macroparticles is obtained.

**Figure 2** shows the transverse (x vs $x_p$ and y vs $y_p$, where x, y are the transverse beam size coordinates and

**Table 2. The design parameters of the RFQ.**

| Design Parameters | Value | |
|---|---|---|
| Intervane Voltage, V | 79.97 | kV |
| Beam Current | 30 | mA |
| Modulation Parameter, m | 1-1.9523 | |
| Minimum Aperture, a | 0.2307 | cm |
| Average Radius, $r_0$ | 0.3495 | cm |
| Transverse Radius of Curvature of Vane tip, ρ | 0.3104 | cm |
| Synchronous Phase, $\varphi_s$ | -90 to -30 | degrees |
| Maximum Surface Electric Field | 31.72 (1.7 kilpatrick) | MV/m |
| Transmission Efficiency | 98 % | |
| Beam Power | 88 | kW |
| Total Length | 346.63 | cm |
| Input Emittance, $\varepsilon_{x,y,rms,n}$ | 0.02 | π cm-mrad |
| Output Emittance, $\varepsilon_{x,rms,n}$ | 0.0227 | π cm-mrad |
| $\varepsilon_{y,rms,n}$ | 0.0227 | π cm-mrad |
| $\varepsilon_{z,rms,n}$ | 0.113 | MeV-deg |

 

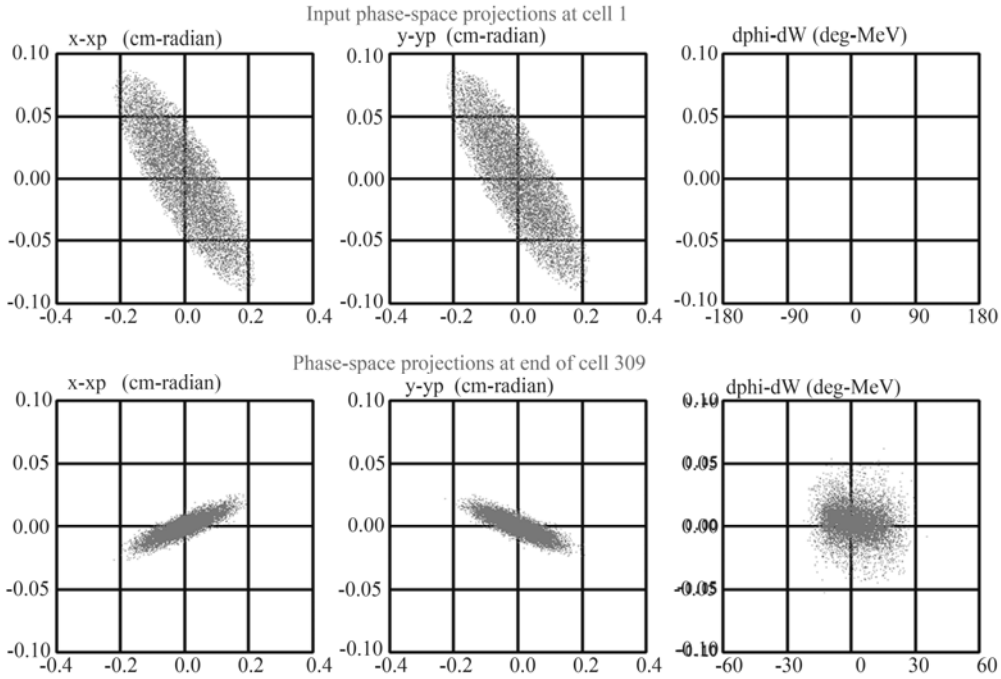


**Figure 2. The phase-space projections at input of cell 1 and output of cell 309.**

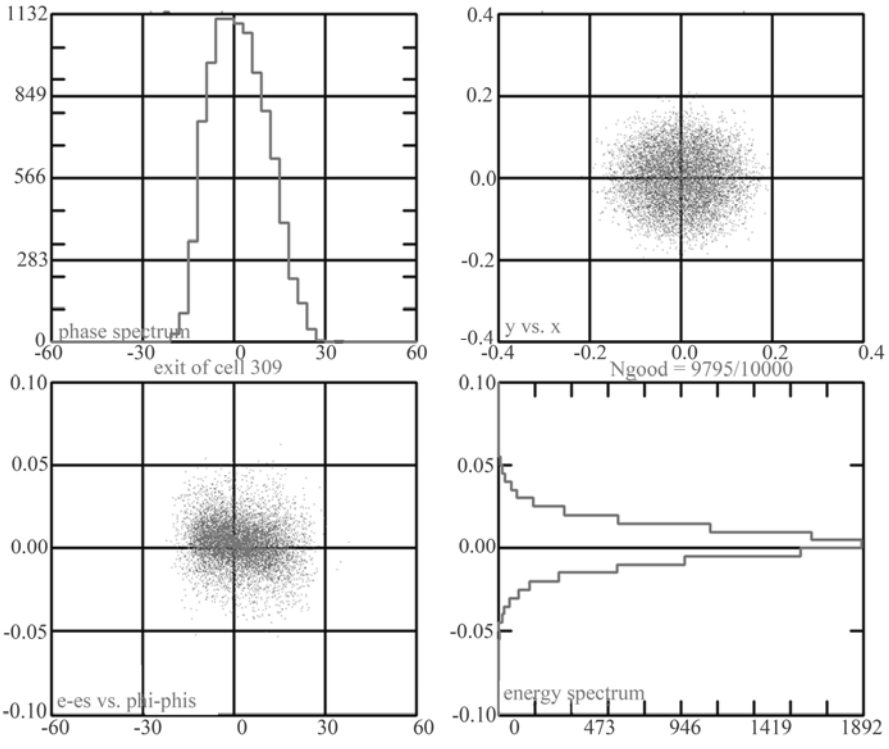


**Figure 3. Phase spectrum (top left) and the energy spectrum (bottom right) at the exit of cell 309. The top right and the bottom left shows the distributions in x vs y and dw vs dphi respectively.**

$x_p$, $y_p$ are the transverse beam divergence coordinates) and longitudinal (dphi vs dw, where dphi and dw are the phase spread and energy spread of the particles respectively) phase space projections at the entrance and exit of RFQ. Here, the phase space projections are representing the unnormalized emittances. The unnormalized trans-

 

verse emittance is reduced at the output of RFQ because of the reason that the divergences of the particles are reduced during longitudinal acceleration. The acceleration does not affect the normalized emittance. The initial longitudinal beam entering the RFQ has no phase space area because of zero energy spread. The bunching and acceleration of the beam takes place along the RFQ. As the bunch picks up energy spread, the separatrix height dw increases to contain the particle orbits, and the beam has a non-zero longitudinal emittance at the exit of RFQ.

**Figure 3** shows the transverse (y vs x) and longitudinal (dw vs dphi) beam profiles; and the phase spectrum (number of macroparticles vs phase spread) and energy spectrum (number of macroparticles vs energy spread) at the output of RFQ. The transverse beam profile is showing the beam radius of ~1.6 mm which is calculated from the twiss parameters at the end of RFQ. It can be noticed from the spectrum that 98% transmitted particles are distributed around the peak at zero energy spread and zero phase spread.

## 3. Error Analysis of Input Beam Parameters

Transmission efficiency of RFQ depends on the various design parameters. In reality there are some fluctuations in the value of ion source parameters, beam parameters etc which greatly affect the transmission of the particles through RFQ. To set some tolerance limits on the various parameters, the error study [4] is performed. The study of the effect of errors on the beam dynamics of the 3 MeV RFQ is carried out with the help of code PARMTEQM. The variation of transmission efficiency is studied with the various effects, *i.e.* input beam displacement, beam angle divergence, voltage factor, input emittance, input energy deviation, input current etc. **Figures 4-9** show the various effects. The acceptance criterion is taken as 95% transmission. Based on this criterion, the tolerance limits are set on the various parameters.

**Figure 4** shows the variation of transmission effi-

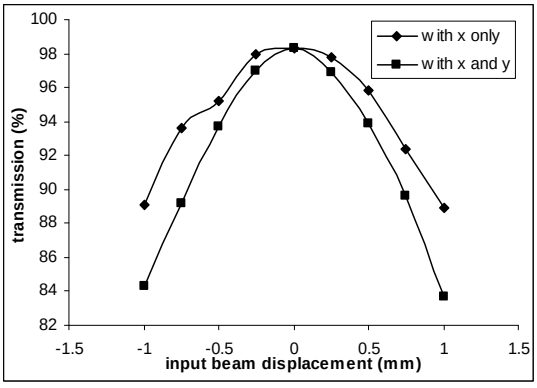


**Figure 4. Transmission vs Input beam displacement.**

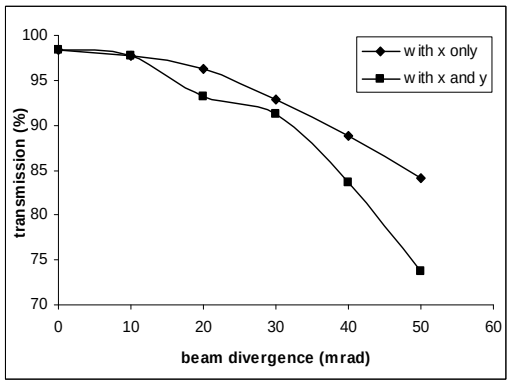


**Figure 5. Transmission vs Beam divergence.**

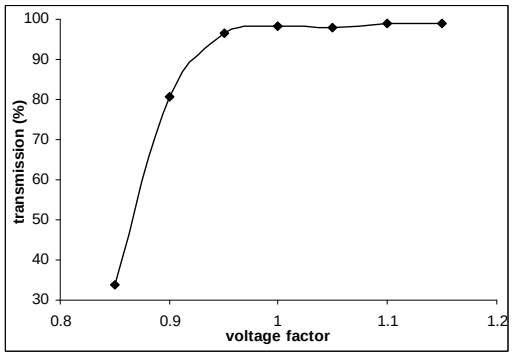


**Figure 6. Transmission vs Voltage factor.**

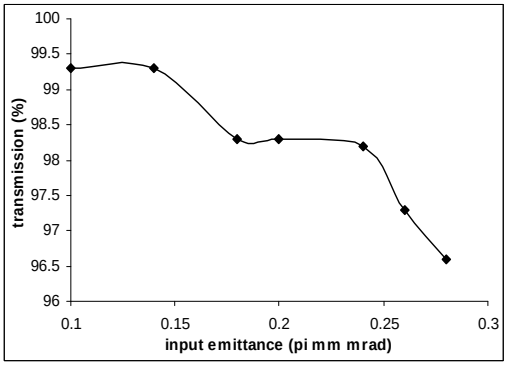


**Figure 7. Transmission vs Input emittance.**

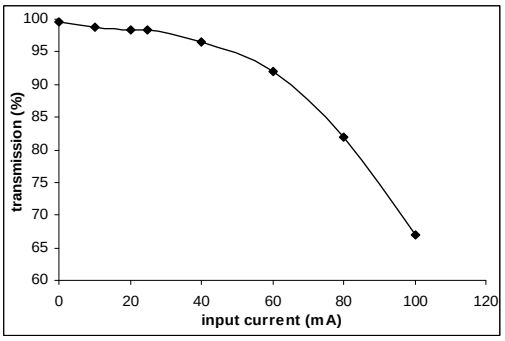


**Figure 8. Transmission vs Input Current.**

 

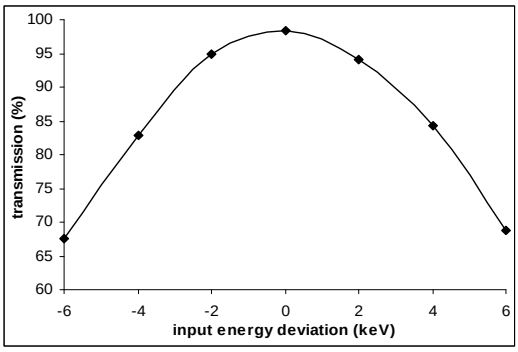


**Figure 9. Transmission vs Input energy deviation.**

ciency with the input beam displacement in transverse directions. With the displacement of beam the transmission efficiency goes down. From the graph shown, the input beam displacement of ± 500 μm is acceptable.

**Figure 5** is the graph between transmission efficiency and beam angle divergence. As the angle of divergence increases, percentage transmission reduces. For obtaining the transmission more than 95%, beam angle divergence of ~15 mrad is acceptable.

**Figure 6** shows the transmission efficiency vs the voltage factor. Voltage factor is a vane-voltage multiplier. It can be seen from the graph that below the value 0.95 of voltage factor the transmission reduces sharply, therefore the voltage factor has to be kept greater than 0.95 for better transmission.

From the graphs for transmission vs input emittance and current, which are shown in **Figures 7 and 8** respectively, it can easily be observed that the transmission will be better for lower emittance and lower current. The input beam current upto ~50 mA is acceptable.

**Figure 9** shows how transmission behaves with the variation in the energy of the beam coming to the input of RFQ. From the graph the input energy deviation of ± 2 keV is acceptable for the transmission greater than 95%.

## 4. Design of Two-Dimensional RFQ Cavity

For the designing of CW or pulsed structures, some parameters have to be optimized accordingly. The main consideration while designing the CW RFQ is to keep the power dissipation minimum. The lower power dissipation per unit length is required to ease the cooling. The power dissipation should be kept much below 1 kW/cm of the structure; otherwise cooling related problems will arise. Therefore, a lower vane voltage should be preferred for the high duty factor/CW operation, which results in low power dissipation per unit length. On the other hand, for the pulsed accelerators, there is no problem of cooling because power dissipation is reduced due to low duty factor. Since in our case, a pulsed beam is needed from linac, we need not worry about the power dissipation and cooling problems. However, we have paid much attention on the alignment and tolerance limits, for fabrication purpose, which become too stringent at higher frequencies, as in this case 352.2 MHz. The RFQ cavity is designed with the 2-D simulation code SUPERFISH [8].

The two-dimensional cavity is designed in SUPERFISH and the various geometrical parameters are optimized to obtain the designed frequency of 352.2 MHz. **Figure 10** is showing the cross-section of one quadrant of RFQ cavity and **Figure 11** is highlighting the details near the vane-tips. The geometrical parameters, *i.e.*, average bore radius '$r_0$', vane-tip transverse radius of curvature '$\rho$' are determined from the beam dynamics design and used in SUPERFISH for cavity design. The voltage difference between adjacent vane tips (at the peak of the rf waveform) is called the gap voltage '$V_g$'. The gap voltage is set to 79.97 kV to normalize the fields.

In **Figure 11**, the lower left corner is the RFQ beam axis. The unmachined tip of the vane is often referred as the "vane blank." Before the numerically controlled machining of the tip, the vane blank would have a rectangular cross section in these views. The break-out angle '$\alpha_{bk}$' for the tool bit cutting the vane is selected to be 15 degrees. Thus, the half width '$B_W$' of the vane blank must always exceed the vane-tip radius of curvature '$\rho$' for cross sections at any longitudinal position along the vane, otherwise it would be very difficult to machine the tip without leaving a ridge along one side of the vane. A raised ridge would be especially undesirable because of the high electric field near the tip. Therefore, the vane blank half width is optimized to be 0.6 cm. The vane blank depth '$B_D$' is the distance from the RFQ axis to the vertex of angle '$\alpha_1$'. At this point, the vane width increases at distances farther from the RFQ axis until it reaches the limit set by '$W_s$', the half width of the vane shoulder. The shoulder segment of length '$L_s$' is parallel to the vane axis. At the end of the shoulder segment farthest from the RFQ axis is the vertex of angle '$\alpha_2$'. Again, the vane width increases farther from the RFQ axis until it reaches the limit set by '$W_b$', the half width of the vane base.

The various geometrical parameters are listed in **Table 3**.

With these geometrical parameters, a quadrant of RFQ cavity was designed. After setting these parameters, the appropriate boundary conditions were applied to calculate the quadrupole ($TE_{210}$-like) and the dipole ($TE_{110}$-like) modes. For the quadrupole mode, the Neumann boundary condition was applied to upper and right edges and the Dirichlet boundary condition was applied to lower and left edges in the problem geometry. The quadru-

 

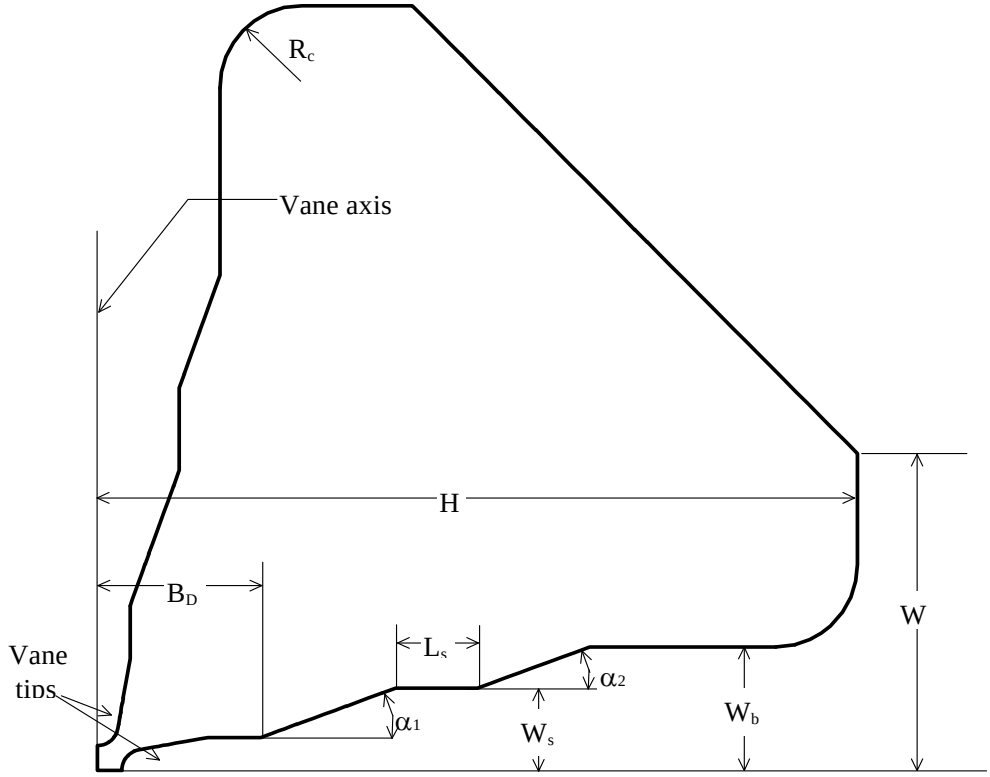


**Figure 10. Cross-section of one quadrant of an RFQ cavity.**

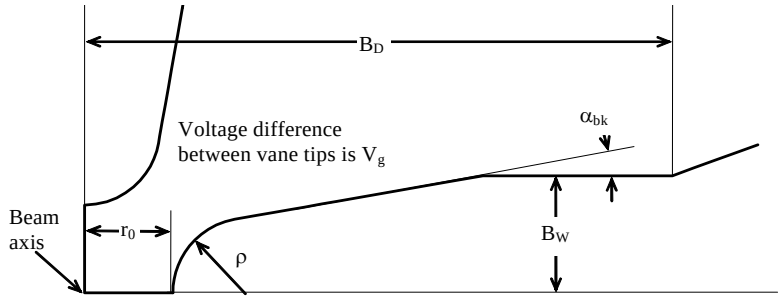


**Figure 11. Details near the vane tips for the RFQ quadrant.**

**Table 3. Geometrical parameters of the RFQ.**

| Parameters | Values | |
|---|---|---|
| Average Bore Radius, $r_0$ | 0.3495 | cm |
| Vane-Tip Transverse Radius of Curvature, $\rho$ | 0.3104 | cm |
| Gap voltage, $V_g$ | 79.97 | kV |
| Breakout Angle, $\alpha_{bk}$ | $15^0$ | |
| Vane-Blank Half Width, $B_w$ | 0.6 | cm |
| Vane-Blank Depth, $B_D$ | 2.5 | cm |
| Vane Shoulder Half Width, $W_S$ | 1.0 | cm |
| Vane Base Half Width, $W_b$ | 1.5 | cm |
| Vane height, H | 9.2052 | cm |

pole mode frequency of the cavity was optimized at 352.1996 MHz; and the quality factor for this mode was calculated to be 10030. To calculate the dipole mode frequency, the left edge of the problem geometry was changed to Neumann boundary. The adjacent dipole mode frequency was obtained as 342.0099 MHz.

The total power dissipation on the walls per quadrant is 230 W/cm, hence the total structure power loss for

 

whole the RFQ cavity of the length 346.6316 cm was calculated to be 319 kW. Since the beam power from the beam dynamics calculation was found to be 88 kW; thus the total power dissipation in the RFQ is the sum of structure power dissipation and beam power, hence calculated to be 407 kW. This power dissipation is calculated for the CW beam. In our case of pulsed RFQ, the power dissipation will be greatly reduced by the duty factor.

The frequency sensitivities in horizontal and vertical directions are much higher at the vane-tips than any other points, so the special care has to be taken for the mechanical design near vane-tips.

The two-dimensional design parameters of the RFQ are listed in **Table 4**.

## 5. Three-Dimensional RFQ Cavity Design

To look into the more details of electromagnetic field properties required by the beam dynamics in the RFQ, the three-dimensional model of RFQ cavity was prepared in CST Microwave Studio code [9].

After the beam dynamics design, done in PARMTEQM code, the electromagnetic design of RFQ cavity was done in two-dimensional code SUPERFISH. But for the detailed study of electromagnetic design of RFQ, a three-dimensional model was required. Due to the complexity of the RFQ structure, a three-dimensional model with large mesh ratio was required to adequately model the necessary details of the structure. To solve the model with large mesh ratio, an accurate enough three- dimensional code is needed to predict the correct resonant frequency and electromagnetic field of the structure. CST Microwave Studio code is a three-dimensional electromagnetic code which is accurate enough due to Perfect Boundary Approximation (PBA) technique. The three-dimensional model of RFQ was prepared in CST MWS as per the dimensions optimized from two-dimensional code SUPERFISH. The unmodulated RFQ cavity model is shown in **Figure 12**.

To determine the resonant frequency of the structure, the right boundary conditions should be applied. In the transverse directions (x and y), the boundaries are electric ($E_t = 0$); and in the longitudinal direction (z), the magnetic boundaries ($H_t = 0$) are applied. RFQ is a symmetric structure; it has two symmetry planes at the axis. To save the memory and the CPU time, only a quadrant of the structure was simulated. To simulate the quadrupole mode, the magnetic boundary conditions ($H_t = 0$) were put at the both xz- and yz- planes. For calculating the dipole mode, the boundary conditions at xz- and yz-planes should not be same, which means that either put electric boundary in xz-plane and magnetic boundary in yz-plane, or magnetic boundary in xz-plane and electric boundary in yz-plane [10].

**Table 4. Two-dimensional design parameters of RFQ.**

| Parameters | Values | |
|---|---|---|
| Resonant Frequency | 352.1996 | MHz |
| Adjacent Dipole Mode Frequency | 342.0099 | MHz |
| Power Dissipation | 920 | W/cm |
| Total Structure Power Loss | 319 | kW |
| Beam Power | 88 | kW |
| Total Power Dissipation | 407 | kW |
| Quality Factor | 10030 | |
| Material of Fabrication | OFHC Cu | |

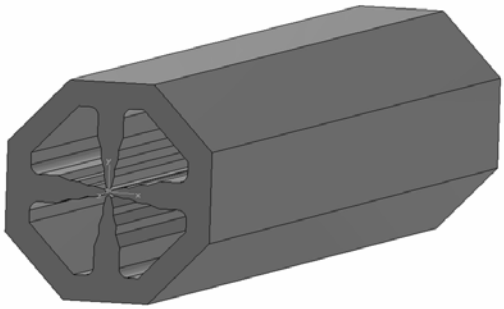

**Figure 12. The unmodulated RFQ model.**

The quadrupole mode and dipole mode frequencies were calculated with the eigenmode solver. The calculated frequencies from CST MWS code were close to those calculated from two-dimensional SUPERFISH code but not exactly matching because of limitation of 3D code in handling a large number of mesh points. Due to this reason the operating quadrupole mode frequency for the 3-dimensional unmodulated RFQ structure was considered to be 350.913 MHz optimized from CST MWS.

### 5.1. Study of Vane-Ends

The RFQ resonator has, of course, to be closed at both ends. In this situation, the longitudinal magnetic field will be perpendicular to the end cover; but to satisfy the boundary condition, the magnetic field must be parallel to the end cover. For the solution of this problem the vane-ends should be designed in such a way so that the magnetic field must turn round and this change of direction must not influence the constant vane potential. Therefore, the vanes should not extend right up to the end covers and, in addition the cut-backs are given at the both ends, entrance and exit, to facilitate the U- turn of the magnetic field. The 'end region' can also be represented by an equivalent circuit shown in **Figure 13**. It must resonate at the quadrupole frequency, *i.e.* $L_e C_e = LC$, which is a condition necessary to keep the vane potential constant. Here $L$ and $C$ are representing the inductance and capacitance respectively of the RFQ

 

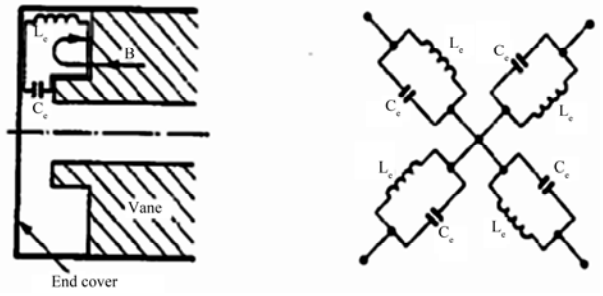


**Figure 13. Equivalent circuit of RFQ vane-ends.**

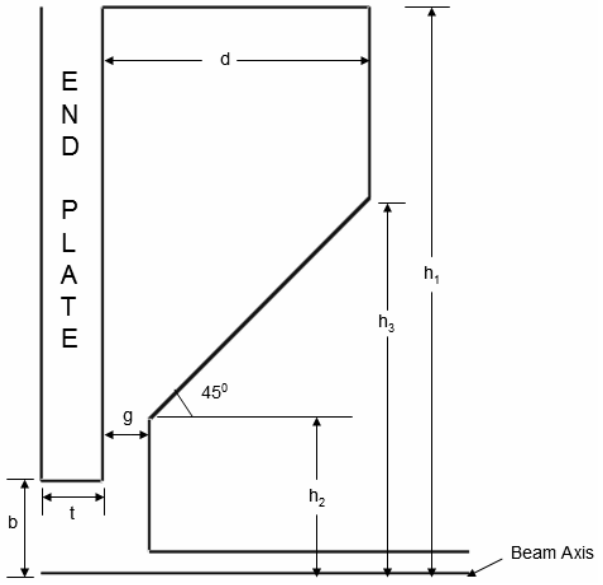


**Figure 14. Cutback dimensions at the entrance and exit of RFQ.**

cavity, whereas $L_e$ and $C_e$ stand for vane-end region.

**Figure 14** is showing the parameters optimized for cut-back at the entrance and exit ends of RFQ [11,12]. Keeping the value of g, $h_1$ and slope of $45^0$ constant, we optimized the entrance and exit cutbacks by varying the parameters, *i.e.*, cutback thickness d, end plate thickness t, beam port radius b and heights $h_2$, $h_3$. The optimized values of the parameters are shown in the **Table 5**.

These parameters are optimized such that these end cells resonate at the quadrupole frequency of 350.913 MHz.

## 6. Conclusions

An RFQ is designed for 352.2 MHz operating frequency and 30 mA beam current of $H^-$ particles, which has to be accelerated from 50 keV to 3 MeV, to serve as a low energy front-end injector of 100 MeV linac.

The beam dynamics study of RFQ is done with the help of PARMTEQM simulation code. The various beam dynamics parameters are optimized for the maximum transmission of particles and the minimum emittance growth while beam passes through RFQ. With the optimization of various parameters, the transmission efficiency of 98% is achieved with less than 14% emittance growth at the exit of RFQ.

**Table 5. The geometric parameters of the end cells.**

| Parameters | Value (for RMS end) | | Value(for fringe- field end) | |
|---|---|---|---|---|
| g | 0.7652 | cm | 0.5149 | cm |
| $h_1$ | 9.2052 | cm | 9.2052 | cm |
| $h_2$ | 2.5 | cm | 2.5 | cm |
| $h_3$ | 6.1034 | cm | 5.846 | cm |
| d | 4.3686 | cm | 3.8609 | cm |
| t | 1.0 | cm | 1.0 | cm |
| b | 1.5 | cm | 1.5 | cm |

Due to fluctuations in various parameters, the transmission of the particles is greatly affected, so the error analysis is performed to study the effect of these parameters on the transmission efficiency.

For the electromagnetic study of RFQ, the two-dimensional cavity is designed with the help of SUPERFISH simulation code. The various geometrical parameters of RFQ cavity are optimized to attain the desired operating frequency 352.2 MHz. The total power dissipation of ~407 kW and the quality factor of 10030 are calculated of the RFQ cavity for the quadrupole mode. The nearest dipole mode frequency is obtained at 342.0099 MHz. For the detailed electromagnetic analysis of fields inside the cavity, a three-dimensional model of RFQ cavity was created and analysed in CST Microwave Studio as per the geometric dimensions optimized from the PARMTEQM and SUPERFISH code. In the end, to make the U-turn of magnetic field and to flatten the field in the four quadrants the cut-backs at the both ends, entrance and exit, are studied. Based on these studies, the fabrication of a prototype RFQ has been started.

## 7. Acknowledgements

We thank Dr. P. D. Gupta (Director, RRCAT) and Dr. P. Singh (Incharge, IAP, RRCAT) for the constant encouragement and keen interest in the project. We are also thankful to Mrs. Nita Kulkarni, P. K. Jana and Chirag Patidar for the useful discussions.

## REFERENCES

[1] T. P. Wangler; "Principles of RF Linear Accelerators," John Wiley & Sons, New York, 1998.

[2] J. W. Staples, "RFQs- An Introduction," LBL-29472.

[3] K. R. Crandall, T. P. Wangler, L. M. Young, J. H. Billen, G. H. Neuschaefer and D. L. Schrage, "RFQ Design Codes," LA-UR-96-1836.

[4] Z. H. Luo, X. L. Guan, S. N. Fu, L. L. Wang and Z. Y.

 

Guo, "Beam Dynamics Design and Error Study of the 5MeV RFQ," *Proceedings of the Second Asian Particle Accelerator Conference*, Beijing, 17-21 September 2001, pp. 439-441.

[5] H. J. Kwon, Y. S. Cho, J. H. Jang, H. S. Kim and Y. H. Kim, "Fabrication of the PEFP 3 MeV RFQ Upgrade," *Proceedings of* 2005 *Particle Accelerator Conference*, Knoxville, Tennessee, 16-20 May 2005, pp. 3010-3012.

[6] J. M. Han, Y. S. Cho, B. J. Yoon, B.H. Choi, Y. S. Bae, I. S. Ko, and B. S. Han, "Design of the KOMAC $H^+/H^-$ RFQ Linac," *Proceedings of XIX International Linear Accelerator Conference*, Illinois, 23-28 August 1998, pp. 774-776.

[7] H. F. Ouyang, S. Fu, "Study of CSNS RFQ Design," *Proceedings of LINAC* 2006, Knoxville, Tennessee, 21-25 August 2006, pp. 746-748.

[8] J. H. Billen and L. M. Young, "Poisson Superfish," LA-UR-96-1834.

[9] CST Studio Suite, "CST Microwave Studio," 2008. http://www.cst.com

[10] D. Li, J. W. Staples and S. P. Virostek, "Detailed Modeling of the SNS RFQ Structure with CST Microwave Studio," *Proceedings of LINAC* 2006, Knoxville, Tennessee, 21-25 August, 2006, pp. 580-582.

[11] H. F. OuYang, T. G. Xu, X. L. Guan, Z. H. Luo and W. W. Xu, "The Study on RF Field of an RFQ," *Proceedings of the Second Asian Particle Accelerator Conference*, Beijing, 17-21 September 2001, pp. 722-724.

[12] G. Romanov and A. Lunin; "Complete RF Design of the HINS RFQ with CST MWS and HFSS," *Proceedings of LINAC*08, Victoria, BC, 29 September-3 October 2008, pp. 163-165.

 

*J. Electromagnetic Analysis & Applications*, **2010, 2, 529-542**
doi:10.4236/jemaa.2010.29069 Published Online September 2010 (http://www.SciRP.org/journal/jemaa)

# Elevated Ferrite Film Circulator with Different Permittivities for Layers: An Analytical Expression for the Input Conductance Employing Perturbation Method

**Arash Rashidi [1], Ali Banai [2]**

[1]Electrical and Computer Engineering Department, Northeastern University, Boston, USA; [2]Electrical Engineering Department, Sharif University of Technology, Tehran, Iran.
Email: rashiditarha.a@neu.edu, banai@sharif.ir

Received July 9th, 2010; revised July 31st, 2010; accepted July 31st, 2010

## ABSTRACT

*The main idea of this paper is to find an analytical formula for the input conductance of an elevated ferrite film circulator to match it systematically to the desired matching network. For solving the ferrite loaded dielectric resonator included in stripline elevated ferrite film circulator, the off diagonal components of the permeability tensor are taken as the perturbation. The electromagnetic fields computations are done for unperturbed structure. The dipolar resonant frequencies corresponding to* $\pm 1$ *harmonics of the resonant modes are then calculated using the perturbation integrals. The quality factor of the circulator is derived in terms of these dipolar resonant frequencies. Energy integrals are calculated to find the energy stored in the ferrite and dielectic layers. An analytical expression for the input conductance of the elevated ferrite film circulators is derived by using the quality factor and energy integrals. In this expression the ferrite and dielectric layers can have different permittivities. Some discussions about the effect of ferrite film thickness and permittivity mismatch on the bandwidth of the circulator are investigated by HFSS commercial software.*

***Keywords*****:** *Elevated Ferrite Circulator, Perturbation Integral, Splitting Factor, Dipolar Resonant Frequencies*

## 1. Introduction

Y-junction ferrite circulators are important devices in today microwave circuits and have been studied in literature in recent years [1-5]. This significance is initiated and spread out from the directional properties of ferrimagnetic devices allowing the control of microwave signals through a bias magnetic field [6]. Ferrite circulators with minimal size, weight and cost can be used in phased array antenna modules [7]. The other applications of Y-junction ferrite circulators can be in transmit receive functions where a shared antenna is required to be used for both transmission and reception of the signal [8].

Design theory for stripline Y-junction ferrite circulators was flourished by Bosma's Green's function [9]. According to Bosma's assumptions the electric field is normal to the plane of the device ( $z-$ direction) and the magnetic field is in the plane of the device ( $\rho-$ and $\varphi-$ components ) [6]. The most important point in Bosma's formulation is the relation between resonance (in which the peripheral of ferrite cylinders becomes PMC, perfect magnetic conductor) and Green's function. If the off diagonal components of the permeability tensor of the ferrite, which are effectively shown by $\kappa/\mu$, go to zero, the ferrite becomes an isotropic medium. In this situation, just like a dielectric resonator, there is no difference between resonant frequency of clockwise mode, proportional to $e^{-jn\varphi}$, and that of counterclockwise mode, proportional to $e^{jn\varphi}$, where $n$ is an integer number. As $\kappa/\mu$ increases, the resonant frequencies $\omega_n^+$ and $\omega_n^-$, which correspond to $e^{jn\varphi}$ and $e^{-jn\varphi}$ respectively, separate each other; That is why $\kappa/\mu$ is called splitting factor. The variation of resonant frequencies versus splitting factor gives a mode chart for operating of a Y-junction ferrite circulator which is very well demonstrated in Bosma's paper. Among these splitting modes, those which are proportional to $e^{\pm j\varphi}$, dipolar modes,

 

catch the attention of circulator designers since they result in a minimum diameter of the ferrite cylinders [10]. According to Bosma's mode chart, we can place the circulator in dipolar mode regime by choosing the value for operational frequency, $\omega_0$, near the dipolar resonant frequencies, $\omega_1^+$ and $\omega_1^-$, and far from other resonant frequencies $\omega_n^{\pm}$, where $n \neq 1$ for a given splitting factor, $\kappa / \mu$.

In addition to Bosma's essential works about Y-junction ferrite circulators, the immense efforts of Fay and Comstock [10] are really praiseworthy. The main work of Fay and Comstock is the presentation of an equivalent circuit modeling the Y-junction circulator viewed from the input port when its other two ports are terminated to matched load in dipolar mode regime. This equivalent circuit was presented originally by Butterweck [11] for waveguide circulators. At the operational frequency, the input admittance of the circuit will be pure real, $G_c$. This input conductance, $G_c$, is the most essential parameter for a circulator because without that we are sightless to choose stripline widths to match our circulator to 50 $\Omega$ network. By using the equivalent circuit the external quality factor of the circulator, $Q$, is determined in terms of dipolar resonant frequencies. Fay and Comstock [10] presented an electromagnetic expression for finding the quality factor. This expression for $Q$ includes total electric energy stored in ferrite cylinders as well as the input power coming to the circulator, which is in terms of input conductance, $G_c$. If we make the expression for $Q$ achieved from circuit analysis equal to that achieved from electromagnetic computations, we can reach to a closed form for $G_c$. Then to find $G_c$ we need not only to compute dipolar resonant frequencies but also we need to solve Maxwell's equations to find the profile of electric field vector within the ferrite cylinders.

Integration of ferrite-film non-reciprocal devices into microwave front-end electronic could lead to significant cost savings in T/R modules [12]. In conventional circulators a ferrite cylinder fills completely the space between the central metal disk and the ground plane in stripline or microstrip structure so they are not good remedies for integration of circulators. In elevated substrate circulators a circular ferrite thin film is deposited on dielectric substrate with a fabrication technology such as chemical vapor deposition [13] and then the central metal disk is placed on the ferrite thin film. Then between the ground and central metal disk we have two cylindrical layers: ferrite thin film and dielectric substrate layer.

The first microstrip junction ferrite film circulator for use in MICs was demonstrated by Hartwig and Readey [14]. For simplicity they assumed the ferrite has the same dielectric constant as the substrate. They applied perturbation theory to find the dipolar resonant frequencies for the ferrite loaded dielectric cavity. Indeed they made the splitting factor, $\kappa / \mu$, as the perturbation and then the unperturbed structure would be a dielectric resonator with magnetic wall as its peripheral and two circular electric walls or metals as its top and bottom. The dipolar electromagnetic field profile for this unperturbed cavity is in $TM_{110}$ form and has no variation normal to the plane of the device because the permittivity of ferrite film has been assumed to be equal to that of dielectric layer. Having dipolar resonant frequencies, Hartwig and Readey computed the quality factor of the circulator. Finally, they designed a matching network by using Anderson's approximate formulation [15] and without electromagnetic computations for energy calculation to find input conductance of the circulator. Later Jones *et al.* [13] reported the design of an elevated substrate ferrite film circulator having 20 dB isolation over 12-12.6 GHz without any details about the matching of their circulator. How *et al.* [12] calculated S-parameters and losses in ferrite-film junction circulators using a new effective-field theory assuming TEM-like propagation. Oshiro *et al.* [16] designed a microstrip Y-junction circulator with ferrite thin film and analyzed its transmission characteristics by the 3D finite-element method. In addition to Bosma [9] and Fay [10], Helszajn [2,17,18] worked on a lot of numerical and analytical formulations about ferrite circulators.

The main question is to how find the input conductance of the elevated ferrite film circulator to manipulate and tailor the matching network systematically and not with trial and error or any convoluted iteratively optimization to find a desired width for the stripline (or microstrip) matching network. This question has not been answered since Hartwig [14] in 1970 until now. This paper answers the question by presenting more general case in which ferrite and dielectric layers no longer have the same permittivities. First we compute the electromagnetic fields profile for unperturbed structure in which splitting factor is zero. For unperturbed resonator, we have a cylindrical resonator containing two elevated dielectic cylinders with different permittivities. A less naive computation is needed for computing the electromagnetic field profile of this resonator because of the non-uniform permittivity in $z-$ direction. Unlike the case in which permittivities of ferrite and dielectric layers are the same, in this case the modes are in the form $TM_{11\delta}$ in which $\partial / \partial z \neq 0$. Also the electric filed vector has $\rho-$ and $\varphi-$ components in addition to $z-$component. Our gain from electromagnetic computa-

 

tions of unperturbed structure can be used in three procedures. First, we can take our operational frequency as a known value and then from a transcendental characteristic equation of unperturbed resonator, an expression for the radius of the circulator can be found. Second, the perturbation theory for computing dipolar resonant frequencies of the perturbed resonator needs the electromagnetic fields profiles. In this procedure we achieve to $\omega_1^+$ and $\omega_1^-$ analytically by computing perturbation integrals and then the quality factor of the circulator can be derived. Third, as we mentioned before we can reach to input conductance for the elevated ferrite film circulator by an electromagnetic method which needs energy stored in the resonator. These computations must be done for both ferrite and dielectrics layers and they deal with integrals including Bessel's functions which are brought in the appendix. After that we achieve an analytical formula for the input conductance of an elevated substrate ferrite film circulator operating in dipolar regime with different permittivities for its ferrite and dielectric layers. Having the input conductance, $G_c$, we can find the necessary quarter wave matching transformer impedance, or at least to design a broader band-width matching network we know the external 50 Ω line should be matched to our analytically achieved impedance, $G_c^{-1}$. So the main gain which can be achieved through this paper is that by having $G_c$, designing of the matching network for elevated substrate circulator will be highly simplified and convoluted iteratively optimizations, for the required width of the quarter wave length transformer, tapered line, or any other matching circuit, are no longer needed. We make some simulations using HFSS [19] at the end to find the frequency behavior of the scattering parameters of the circulator matched by using the conductance formula in this paper.

## 2. Configuration and Equivalent Circuit of an Elevated Ferrite Film Circulator

**Figure 1** is a schematic diagram of an elevated stripline ferrite film circulator. Like conventional stripline ferrite circulators the central metal includes a metal disk of radius $R$ attached to three metal strips at points $120^\circ$ apart around its peripheral. Between the ground and metal disk we have two layers: ferrite film with the same radius $R$ and thickness $t$ and dielectric layer which is the substrate of the stripline structure. The total thickness of ferrite and dielectric layers is $b$. $G_c$ is the input conductance of the circulator when the other two ports are terminated to matched load of reference impedance $Z_0$. To match the bare circulator, quarter wavelength transformers are used with characteristic impedance

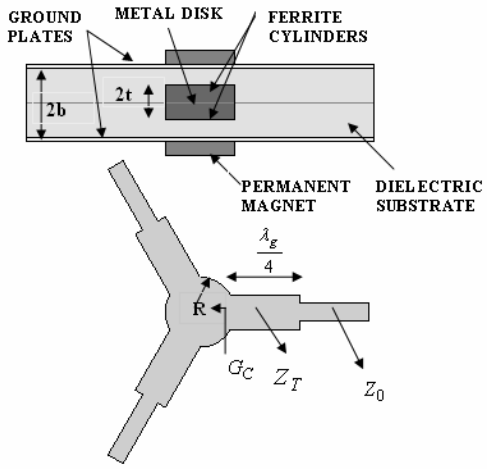


**Figure 1. Ferrite film circulator configuration.**

$Z_T = \sqrt{Z_0 / G_c}$. It is worth mentioning that choosing the quarter wave length transformer is just for simplicity and other matching circuits can be used as well. The permittivities of the dielectric substrate and ferrite cylinders are $\varepsilon_d = \varepsilon_{rd}\varepsilon_0$ and $\varepsilon_f = \varepsilon_{rf}\varepsilon_0$ respectively.

The ferrite is just saturated along $z-$direction, normal to the plane of the device, which means the magnetic flux density produced by the permanent magnet equals to saturation magnetization of the ferrite, $4\pi M_S$. In this case the permeability tensor is [20]

$$[\mu] = \begin{bmatrix} \mu & j\kappa & 0 \\ -j\kappa & \mu & 0 \\ 0 & 0 & \mu_0 \end{bmatrix} = \mu_0 \begin{bmatrix} 1 & -jp & 0 \\ jp & 1 & 0 \\ 0 & 0 & 1 \end{bmatrix} \quad (1)$$

where $p$ is the normalized magnetization frequency or splitting factor defined as

$$p = \frac{\kappa}{\mu} = \frac{\gamma\ 4\pi M_S}{f_0} \quad (2)$$

In Equation (2), $\gamma = 2.8\dfrac{\text{MHz}}{\text{Gauss}}$ is gyromagnetic ratio, $4\pi M_S$ is the saturation magnetization in Gauss and $f_0$ is the operating frequency.

Resonant modes for which the peripheral of the metal disk becomes PMC or H-wall are very important in ferrite junction circulators design [9]. As we mentioned in introduction, when the splitting factor, $p = \kappa/\mu$, goes to zero, the resonant frequencies, $\omega_n^+$ and $\omega_n^-$, corresponding to clockwise and counterclockwise modes, which are proportional to $e^{jn\varphi}$ and $e^{-jn\varphi}$ respectively, will be degenerated (*i.e.* $\omega_n^+ = \omega_n^-$). As splitting factor increases the difference between $\omega_n^+$ and $\omega_n^-$ goes up. Also we discussed in introduction about why dipolar modes, which are proportional to $e^{j\varphi}$ and $e^{-j\varphi}$, are

 

more interesting. To put the circulator in dipolar regime, in which the dominant modes are dipolar modes, we must choose the operational frequency, $\omega_0 = 2\pi f_0$, near the dipolar resonant frequencies, $\omega_1^+$ and $\omega_1^-$. The conventional choice for operational frequency satisfying this condition for operating the circulator in dipolar regime, is

$$\omega_0 = \frac{\omega_1^+ + \omega_1^-}{2} \tag{3}$$

The equivalent circuit of the ferrite junction circulator from the input port when it operates in dipolar regime is shown in **Figure 2** [10]. In this circuit the other two ports assumed to be connected to the matched load. As shown in **Figure 2** this circuit is the series connection of two shunt R-L-C resonators having resonant frequencies $\omega_1^+$ and $\omega_1^-$. The quality factors of the resonators are $Q^+$ and $Q^-$. Indeed all other non-dipolar resonators are effectively short circuited when the circulator operates in dipolar regime. At the operating frequency which is between the dipolar resonant frequencies, according to Equation (3), one of the shunt resonators has a capacitive property and the other resonator has an inductive property and these capacitive and inductive properties cancel each other. In this situation the input admittance of the equivalent circuit is pure real and equals to $G_c$ which is the key parameter. Without $G_c$ we can not design a matching network systematically.

In practical cases in which the splitting factor is not so large, $0.2 < |\kappa/\mu| < 0.5$ [10], detailed analysis of the equivalent circuit shows that the quality factors of each circulator resonators are approximately the same, $Q^+ \approx Q^-$, and we can denote them by a unit symbol $Q$ that is

$$Q = \frac{\omega_0}{\sqrt{3}(\omega_1^+ - \omega_1^-)} \tag{4}$$

Equation (4) shows that the quality factor of the circulator is known, providing we find dipolar resonant frequencies. Finding $\omega_1^+$ and $\omega_1^-$ needs to analyze the resonator depicted in **Figure 3** [14]. The top of this resonator is the metal disk in the circulator structure; the bottom of this resonator is the ground of the stripline structure. Indeed the elevated stripline ferrite film circulator has one such resonator in each side of the central metal disk. The peripheral wall of the resonator is PMC to find dipolar resonant frequencies.

Full analytical computation of $\omega_1^+$ and $\omega_1^-$ is a thorny procedure. In this problem because the splitting factor is small, we can take it as a perturbation and find the electromagnetic fields profile for unperturbed resonator in which ferrite becomes a dielectric. Having the electromagnetic fields for unperturbed structure dipolar

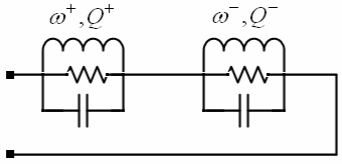


**Figure 2. Equivalent circuit looking in the input port of a matched Y-circulator.**

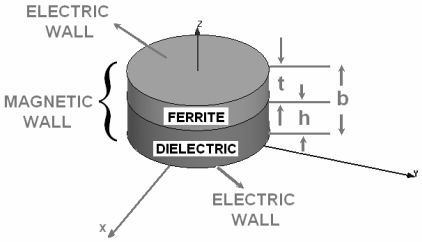


**Figure 3. Ferrite loaded resonator.**

resonant frequencies for perturbed resonator can be found by computing perturbation integrals. We do these procedures in sections III and IV.

## 3. Electromagnetic Field Computations for the Unperturbed Structure

For the unperturbed resonator depicted in Fig. 3 in which $p$ goes to zero, using (1), the ferrite becomes a homogeneous dielectric with dielectric constant $\varepsilon_{rf}$. Consequently we can fiend $\mathrm{TM}_z$ electromagnetic fields for this unperturbed resonator with mixed dielectrics.

For a homogeneous source free region having permittivity $\varepsilon$ and permeability $\mu_0$, if $A$ is a wave function in cylindrical coordinates $(\rho, \varphi, z)$ then it satisfies the scalar Helmholtz equation

$$\frac{1}{\rho}\frac{\partial}{\partial\rho}(\rho\frac{\partial A}{\partial\rho}) + \frac{1}{\rho^2}\frac{\partial^2 A}{\partial\varphi^2} + \frac{\partial^2 A}{\partial z^2} + k^2 A = 0 \tag{5}$$

where $k = \omega\sqrt{\mu_0\varepsilon}$. The components of $\mathrm{TM}_z$ electromagnetic fields are [21]

$$E_\rho = \frac{1}{j\omega\varepsilon}\frac{\partial^2 A}{\partial\rho\,\partial z} \tag{6}$$

$$E_\varphi = \frac{1}{j\omega\varepsilon}\frac{\partial^2 A}{\rho\,\partial\varphi\,\partial z} \tag{7}$$

$$E_z = \frac{1}{j\omega\varepsilon}(\frac{\partial^2}{\partial z^2} + k^2)A \tag{8}$$

$$H_\rho = \frac{1}{\rho}\frac{\partial A}{\partial\varphi} \tag{9}$$

$$H_\varphi = -\frac{\partial A}{\partial\rho} \tag{10}$$

$$H_z = 0 \tag{11}$$

For the unperturbed resonator the suitable wave func-

 

tions which satisfy the boundary conditions on E-walls, $E_\rho = E_\varphi = 0$ at $z = 0$ and $z = b$ (see **Figure 3**), are

$$A_{d,n} = D_n\ J_n(k_c\rho)\ \cos(\beta_d z)\ e^{jn\varphi} \quad (12)$$

$$A_{f,n} = F_n\ J_n(k_c\rho)\ \cos(\beta_f (z-b))\ e^{jn\varphi} \quad (13)$$

where $J_n(k_c\rho)$ is the Bessel function of the first kind, $n = 0,\ \pm 1,\ \pm 2,\ \ldots$ and $k_c$ is the cut off wave number defined as

$$k_c{}^2 = \omega^2\mu_0\varepsilon_f - \beta_f{}^2 = \omega^2\mu_0\varepsilon_d - \beta_d{}^2 \quad (14)$$

The subscripts $d$ and $f$, also superscripts hereinafter, refer to the regions $z < h$, dielectric, and $z > h$, ferrite, as shown in **Figure 3** respectively. The electromagnetic fields components are obtained from equations (6)-(11)

$$E^f_{\rho,n} = \frac{-\beta_f k_c}{j\omega\varepsilon_f} F_n\ J'_n(k_c\rho)\ \sin(\beta_f (z-b))\ e^{jn\varphi} \quad (15)$$

$$E^f_{\varphi,n} = \frac{-n\beta_f}{\omega\varepsilon_f} F_n \frac{J_n(k_c\rho)}{\rho} \sin(\beta_f (z-b))\ e^{jn\varphi} \quad (16)$$

$$E^f_{z,n} = \frac{k_c{}^2}{j\omega\varepsilon_f} F_n\ J_n(k_c\rho)\ \cos(\beta_f (z-b))\ e^{jn\varphi} \quad (17)$$

$$H^f_{\rho,n} = jnF_n \frac{J_n(k_c\rho)}{\rho} \cos(\beta_f (z-b))\ e^{jn\varphi} \quad (18)$$

$$H^f_{\varphi,n} = -k_c F_n\ J'_n(k_c\rho)\ \cos(\beta_f (z-b))\ e^{jn\varphi} \quad (19)$$

$$H^f_{z,n} = 0 \quad (20)$$

$$E^d_{\rho,n} = \frac{-\beta_d k_c}{j\omega\varepsilon_d} D_n\ J'_n(k_c\rho)\ \sin(\beta_d z)\ e^{jn\varphi} \quad (21)$$

$$E^d_{\varphi,n} = \frac{-n\beta_d}{\omega\varepsilon_d} D_n \frac{J_n(k_c\rho)}{\rho} \sin(\beta_d z)\ e^{jn\varphi} \quad (22)$$

$$E^d_{z,n} = \frac{k_c{}^2}{j\omega\varepsilon_d} D_n\ J_n(k_c\rho)\ \cos(\beta_d z)\ e^{jn\varphi} \quad (23)$$

$$E^d_{z,n} = \frac{k_c{}^2}{j\omega\varepsilon_d} D_n\ J_n(k_c\rho)\ \cos(\beta_d z)\ e^{jn\varphi} \quad (24)$$

$$H^d_{\varphi,n} = -k_c D_n\ J'_n(k_c\rho)\ \cos(\beta_d z)\ e^{jn\varphi} \quad (25)$$

$$H^d_{z,n} = 0 \quad (26)$$

Equations (15)-(26) gives the electromagnetic fields profile for unperturbed resonator. For the circulator operating in dipolar regime, only the dipolar modes, $n = \pm 1$, are important. Indeed we deal with $TM_{11\delta}$ mode of the unperturbed resonator. Since the resonant length, $b$, for the $TM_{11\delta}$ mode is less than $(\lambda_g^f + \lambda_g^d)/2$, (where $\lambda_g^f$ and $\lambda_g^d$ are the guide wavelengths of the $TM_{11}$ dielectric waveguide modes when the permittivities are $\varepsilon_f$ and $\varepsilon_d$, respectively) the symbol $\delta = 2b/(\lambda_g^f + \lambda_g^d)$ is used to denote the $z-$variation of the resonant mode [22].

Matching tangential components of $\vec{E}$ and $\vec{H}$ at $z = h$ yields

$$F_{\pm 1}\cos(\beta_f t) = D_{\pm 1}\cos(\beta_d t) \quad (27)$$

$$-\frac{\beta_f}{\varepsilon_f}\tan(\beta_f t) = \frac{\beta_d}{\varepsilon_d}\tan(\beta_d h) \quad (28)$$

Where $t = b - h$, as shown in **Figure 3**. Equation (28) is a transcendental characteristic equation for the unperturbed structure. The splitting of dipolar resonant modes does not occur because the perturbation, splitting factor, is zero. So the dipolar clockwise and counterclockwise modes for the unperturbed structure have a degenerated resonant frequency which is denoted by $\omega_{unp}$. When we include the perturbation the splitting between the dipolar resonant frequencies, $\omega_1^+$ and $\omega_1^-$ will occur and so $\omega_1^- < \omega_{unp} < \omega_1^+$ or $\omega_1^+ < \omega_{unp} < \omega_1^-$. On the other hand if the operational frequency of the circulator is between the dipolar resonant frequencies, the circulator works in dipolar regime so we can take the unperturbed resonant frequency, $\omega_{unp}$, as our operational frequency, $\omega_0$.

In our design procedure, the resonant frequency of the unperturbed structure, $\omega_0$, is a known parameter and using electromagnetic fields profile for degenerated dipolar modes we can find the radius of the circulator, $R$. To do this, satisfying boundary condition of zero tangential $\vec{H}$ at $\rho = R$, magnetic wall, for $n = +1$ or $n = -1$ yields (see Equations (19) and (25))

$$R = \frac{x}{k_c} \quad (29)$$

Where $x = 1.841$ is the first positive root for the derivative of the Bessel function of the first order and of the first kind, $J'_1$. To find $k_c$ we should solve the transcendental characteristic equation (28) by substituting $\beta_f$ and $\beta_d$ from Equation (14). Then we have a transcendental Equation in terms of $k_c$

$$\frac{\tan(t\sqrt{\omega_0{}^2\mu_0\varepsilon_f - k_c{}^2})}{\tan(h\sqrt{\omega_0{}^2\mu_0\varepsilon_d - k_c{}^2})} = \frac{-\varepsilon_f\sqrt{\omega_0{}^2\mu_0\varepsilon_d - k_c{}^2}}{\varepsilon_d\sqrt{\omega_0{}^2\mu_0\varepsilon_f - k_c{}^2}} \quad (30)$$

To have a suitable range for $k_c$ in Equation (30) we must note that the resonant frequency, $\omega_0$, for the unperturbed structure with mixed dielectrics goes to the resonant frequency of the $TM_{110}$ mode, $\omega_0^f = k_c c/\sqrt{\varepsilon_{rf}}$, when the cavity is completely filled by dielectric $\varepsilon_f$ (where $c = 1/\sqrt{\mu_0\varepsilon_0}$). In an analogous manner $\omega_0$ goes to the resonant frequency of the

 

$TM_{110}$ mode, $\omega_0^d = k_c c / \sqrt{\varepsilon_{rd}}$, when the cavity is completely filled by dielectric $\varepsilon_d$. Assuming $\varepsilon_f > \varepsilon_d$, which is a practical case, we have

$$\frac{k_c}{c}\sqrt{\varepsilon_{rd}} < \omega_0 < \frac{k_c}{c}\sqrt{\varepsilon_{rf}} \Rightarrow \frac{\omega_0}{c}\sqrt{\varepsilon_{rd}} < k_c < \frac{\omega_0}{c}\sqrt{\varepsilon_{rf}} \quad (31)$$

Inequality given in (31) presents a good range for finding $k_c$. Finding $k_c$ from transcendental characteristic Equation (30) the radius of the circulator, $R$, by Equation (29) readily is obtained.

For simplicity we define the symbol $\zeta$ called effective permittivity by

$$\zeta = \left(\frac{k_c}{k_0}\right)^2 = \left(\frac{k_c c}{\omega_0}\right)^2 \quad (32)$$

Then from (31) we have $\varepsilon_{rd} < \zeta < \varepsilon_{rf}$. From (14) we can write

$$\beta_f = k_0\sqrt{\varepsilon_{rf} - \zeta} \quad (33)$$

$$\beta_d = k_0\sqrt{\zeta - \varepsilon_{rd}} \quad (34)$$

Then $\beta_f$ is pure real and $\beta_d$ is pure imaginary. In this situation we can write transcendental equation (30) as follows

$$\frac{\tan(k_0 t\sqrt{\varepsilon_{rf} - \zeta})}{\tanh(\kappa_0 h\sqrt{\zeta - \varepsilon_{rd}})} = \frac{\varepsilon_f\sqrt{\zeta - \varepsilon_{rd}}}{\varepsilon_d\sqrt{\varepsilon_{rf} - \zeta}} \quad (35)$$

In practical cases in which the distance between ground plates is rather small, *i.e.* $k_0 b << 2\pi$, we can replace tan and tanh functions by their arguments. In this situation transcendental Equation (35) takes an algebraic form and effective permittivity, $\zeta$, becomes

$$\zeta = \frac{1}{\frac{t/b}{\varepsilon_{rf}} + \frac{1-(t/b)}{\varepsilon_{rd}}} \quad (36)$$

In **Figure 4**, for $f_0 = \omega_0/2\pi = 4$GHz, $b = 1$ mm ($k_0 b = 2\pi/75$), $\varepsilon_{rf} = 14.5$, $\varepsilon_{rd} = 9$, one can plot $\zeta$ versus $t/b$, the ratio of ferrite thickness by the total thickness of ferrite-dielectric layers. We provide this plot using both transcendental Equation (35) and algebraic one (36). It is evident that as ferrite thickness goes down, $\zeta$ approaches to $\varepsilon_{rd}$ and in a similar manner as ferrite thickness goes up, $\zeta$ approaches to $\varepsilon_{rf}$. This figure can be applied for finding the radius of the circulator. For example if the ferrite and dielectric layers have the same thickness (*i.e.* $t/b = 0.5$) according to **Figure 4**, $\zeta = 11.1$ then $k_0 R = 1.841/\sqrt{11.1}$ or $R = 6.6$ mm ($f_0 =$ 4 GHz).

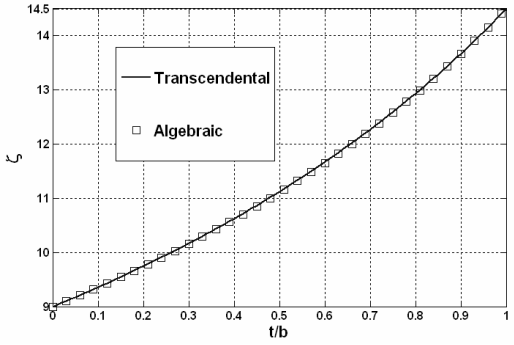


**Figure 4. Effective permittivity versus t/b for $k_0 b = 2\pi/75$, $\varepsilon_{rf} = 14.5$, $\varepsilon_{rd} = 9$ and $b = 1$ mm.**

## 4. Dipolar Resonant Frequencies and Quality Factor of the Perturbed Structure

The resonant frequency for the unperturbed structure analyzed in the previous section is $\omega_0$. For the perturbed structure, with non zero splitting factor, $p = \kappa/\mu$, by perturbation method described in [23], one can find the frequency separation for dipolar frequencies as follows

$$\frac{\omega_1^+ - \omega_1^-}{\omega_0} = \frac{-\int_{\Delta V}(\Delta[\mu]\vec{H}).\vec{H}^* dv}{\mu_0\int_V |\vec{H}|^2 dv} \quad (37)$$

where

$$\Delta[\mu] = [\mu] - \mu_0[I] \quad (38)$$

and $[I]$ is the identity matrix. $\vec{H}$ is the $TM_{11\delta}$ magnetic field for unperturbed structure which we computed its components in (18)-(20) and (24)-(26) for $n = 1$. In our especial case, $\Delta V$ is the volume of the ferrite cylinder and $V$ is the total volume of the resonator depicted in **Figure 3.** We begin with the expression $(\Delta[\mu]\vec{H}).\vec{H}^*$

$$(\Delta[\mu]\vec{H}).\vec{H}^* = \mu_0\begin{bmatrix} 0 & 1+jp & 0 \\ 1-jp & 0 & 0 \\ 0 & 0 & 0 \end{bmatrix}\begin{bmatrix} H^f_{\rho,1} \\ H^f_{\varphi,1} \\ 0 \end{bmatrix}\begin{bmatrix} H^{f\,*}_{\rho,1} & H^{f\,*}_{\varphi,1} & 0 \end{bmatrix} = 2\mu_0\,\mathrm{Re}\left\{(1+jp)H^f_{\varphi,1}H^{f\,*}_{\rho,1}\right\} \quad (39)$$

Substituting $H^f_{\rho,1}$ and $H^f_{\varphi,1}$, Equations (18) and (19) for n=1, in Equation (39) leads

$$(\Delta[\mu]\vec{H}).\vec{H}^* = \frac{-2p\mu_0 k_c}{\rho}|F_1|^2 J_1(k_c\rho)J_1'(k_c\rho)\cos^2(\beta_f(z-b)) \quad (40)$$

Then the integral of the numerator of Equation (37) can be calculated as below

 

$$\int_{\Delta V}(\Delta[\mu]\vec{H}).\vec{H}^{*}dv=-2p\mu_0\left|F_1\right|^2(2\pi)\int_h^b\cos^2(\beta_f(z-b))\,dz\times \int_0^R J_1(k_c\rho)J_1'(k_c\rho)\,k_c d\rho$$
$$=-p\pi\mu_0\left|F_1\right|^2 J_1^{\,2}(x)(t+\frac{\sin(\beta_f t)\cos(\beta_f t)}{\beta_f}) \quad (41)$$

Also in $v$ we have

$$\left|\vec{H}\right|^2=\begin{cases}\left|H^d_{\rho,1}\right|^2+\left|H^d_{\varphi,1}\right|^2 & 0<z<h\\ \left|H^f_{\rho,1}\right|^2+\left|H^f_{\varphi,1}\right|^2 & h<z<b\end{cases}$$
$$=k_c^{\,2}[(\frac{J_1(k_c\rho)}{k_c\rho})^2+(J_1'(k_c\rho))^2] \quad (42)$$
$$\begin{cases}\left|D_1\right|^2\cos^2(\beta_d z) & 0<z<h\\ \left|F_1\right|^2\cos^2(\beta_f(z-b)) & h<z<b\end{cases}$$

Using the notation given in the appendix we can write the integral in the denominator of the Equation (37) in this form

$$\int_V\left|\vec{H}\right|^2dv=k_c^{\,2}[\frac{I_{\rho 2}}{k_c^{\,2}}+I_{\rho 3}](2\pi)\times [\left|D_1\right|^2(\frac{h+\sin(\beta_d h)\cos(\beta_d h)/\beta_d}{2})+ \left|F_1\right|^2(\frac{t+\sin(\beta_f t)\cos(\beta_f t)/\beta_f}{2})] \quad (43)$$

Employing (A-1) and (A-4) to compute the radial integral $[(I_{\rho 2}/k_c^{\,2})+I_{\rho 3}]$ also by using (27) to relate $D_1$ and $F_1$ equation (43) takes this form

$$\int_V\left|\vec{H}\right|^2dv=\frac{\pi}{2}(x^2-1)J_1^{\,2}(x)\left|F_1\right|^2\times [t+\frac{\sin(\beta_f t)\cos(\beta_f t)}{\beta_f}+ (h+\frac{\sin(\beta_d h)\cos(\beta_d h)}{\beta_d})\frac{\cos^2(\beta_f t)}{\cos^2(\beta_d h)}] \quad (44)$$

Now we have computed the integrals in Equation (37). By substituting the computed integrals, Equations (41) and (44), in (37) we have

$$\frac{\omega_1^{+}-\omega_1^{-}}{\omega_0}=\frac{2p}{(x^2-1)}\frac{1}{[1+\frac{(h+\sin(\beta_d h)\cos(\beta_d h)/\beta_d)}{t+\sin(\beta_f t)\cos(\beta_f t)/\beta_f}\frac{\cos^2(\beta_f t)}{\cos^2(\beta_d h)}]} \quad (45)$$

Then the quality factor of the circulator is derived using (45) and (4)

$$\frac{1}{Q}=\frac{\sqrt{3}(\omega_1^{+}-\omega_1^{-})}{\omega_0}=\frac{2p\sqrt{3}}{x^2-1}\frac{1}{1+\frac{h\sec^2(\beta_d h)+(\tan(\beta_d h)/\beta_d)}{t\sec^2(\beta_f t)+(\tan(\beta_f t)/\beta_f)}} \quad (46)$$

In the practical cases in which $k_0 b<<2\pi$ we can easily substitute sec functions by unity and tan functions by their arguments so the transcendental complexity in equation (46) can be removed

$$\frac{1}{Q}=\frac{2p\sqrt{3}}{x^2-1}\frac{1}{1+\frac{h}{t}}=\frac{2p\sqrt{3}}{x^2-1}\frac{t}{b} \quad (47)$$

## 5. Input Conductance of the Ferrite Film Circulator Using Energy Integrals

The electromagnetic field components computed in equations (15)-(26) are proportional to $e^{jn\varphi}$. For operating the three port as a circulator in dipolar regime ($n=\pm 1$), the circulation condition must be satisfied as follows [10]

$$E_z^f(\rho=R,\varphi,z=b)=\begin{cases}E & \varphi=0\\ -E & \varphi=120\\ 0 & \varphi=240\end{cases} \quad (48)$$

where

$$E_z^f=E_{z,1}^f+E_{z,-1}^f \quad (49)$$

From equations (48)-(49) and (17), the amplitudes of dipolar modes, $F_1$ and $F_{-1}$ are found:

$$F_1=\frac{j\omega\varepsilon_f}{k_c^{\,2}}\frac{E}{2J_1(x)}(1+\frac{j}{\sqrt{3}}) \quad (50)$$

$$F_{-1}=\frac{j\omega\varepsilon_f}{k_c^{\,2}}\frac{E}{2J_1(x)}(-1+\frac{j}{\sqrt{3}}) \quad (51)$$

Having $F_1$ and $F_{-1}$ the sinusoidal standing wave form of $E_z^f$ is appeared from (49)

$$E_z^f=e_z^f J_1(k_c\rho)\cos(\varphi+30^\circ)\cos(\beta_f(z-b)) \quad (52)$$

where

$$e_z^f=\frac{2E}{\sqrt{3}J_1(x)} \quad (53)$$

According to (52) dipolar modes create a standing wave pattern proportional to $\cos(\varphi+30^\circ)$ for electric field on the peripheral of the ferrite cylinders in which $\varphi=0^\circ$, $\varphi=120^\circ$ and $\varphi=240^\circ$ correspond to the positions of the input port, output port and isolated port of the circulator respectively. This standing wave pattern makes the polarity of the electric field positive in the half of the peripheral of ferrite cylinders and negative in another half. So the mentioned standing wave pattern make the peripheral of the ferrite cylinders as a dipole and this is the origin of the so-called dipolar modes. Other compo-

 

nents of electrical field in ferrite and dielectric layer can be found using the amplitudes of dipolar modes (50)-(51)

$$E_\rho^f = E_{\rho,1}^f + E_{\rho,-1}^f = e_\rho^f J_1'(k_c\rho)\cos(\varphi+30^\circ)\sin(\beta_f(z-b)) \tag{54}$$

$$E_\varphi^f = E_{\varphi,1}^f + E_{\varphi,-1}^f = e_\varphi^f \frac{J_1(k_c\rho)}{\rho}\sin(\varphi+30^\circ)\sin(\beta_f(z-b)) \tag{55}$$

$$E_\rho^d = E_{\rho,1}^d + E_{\rho,-1}^d = e_\rho^d J_1'(k_c\rho)\cos(\varphi+30^\circ)\sin(\beta_d z) \tag{56}$$

$$E_\varphi^d = E_{\varphi,1}^d + E_{\varphi,-1}^d = e_\varphi^d \frac{J_1(k_c\rho)}{\rho}\sin(\varphi+30^\circ)\sin(\beta_d z) \tag{57}$$

$$E_z^d = E_{z,1}^d + E_{z,-1}^d = e_z^d J_1(k_c\rho)\cos(\varphi+30^\circ)\cos(\beta_d z) \tag{58}$$

where

$$e_\rho^f = -k_c e_\varphi^f = -\frac{\beta_f}{k_c}\frac{2E}{\sqrt{3}J_1(x)} \tag{59}$$

$$e_\rho^d = -k_c e_\varphi^d = -\frac{\varepsilon_f}{\varepsilon_d}\frac{\cos(\beta_f t)}{\cos(\beta_d h)}\frac{\beta_d}{k_c}\frac{2E}{\sqrt{3}J_1(x)} \tag{60}$$

$$e_z^d = \frac{\varepsilon_f}{\varepsilon_d}\frac{\cos(\beta_f t)}{\cos(\beta_d h)}\frac{2E}{\sqrt{3}J_1(x)} \tag{61}$$

To find the input conductance of the circulator at the operating frequency we present an electromagnetic computation in this section. This method is based upon the electromagnetic approach for the quality factor of the circulator that is

$$Q = \frac{\omega_0 U}{P_{out}} \tag{62}$$

where $U$ is two times as much as the stored energy in the resonator described in **Figure 3** (because the stripline structure has one such resonator on each side of the metal disc ), and $P_{out}$ is the power delivered to the output port. We can relate $P_{out}$ to the input conductance of the circulator. Computation of $U$ is a complicated work for the elevated substrate ferrite film circulators because it deals with energy computations in both ferrite and dielectric layers and all components of electric field vector are present, unlike the conventional ferrite circulators in which only $z-$component of electric field is non-zero. In the previous section we found the quality factor, equation (46). Then from the relation between $P_{out}$ and $G_c$ we obtain to a closed formula for the input conductance of the circulator.

$P_{out}$ is defined as

$$P_{out} = G_c \frac{\left|V_{out}^-\right|^2}{2} \tag{63}$$

where $V_{out}^-$ is the outcoming voltage wave at the output port defined as

$$V_{out}^- = \int_0^h E_z^d(\rho=R,\varphi=120^\circ,z)\,dz + \int_h^b E_z^f(\rho=R,\varphi=120^\circ,z)\,dz \tag{64}$$

then using (52) and (58) we reach to a closed form for $V_{out}^-$

$$V_{out}^- = -\frac{\sqrt{3}}{2}J_1(x)\left[\frac{e_z^d}{\beta_d}\sin(\beta_d h) + \frac{e_z^f}{\beta_f}\sin(\beta_f t)\right] \tag{65}$$

and using (63) we can relate output power to the input conductance

$$P_{out} = \frac{3}{8}G_c J_1^2(x)\left[\frac{e_z^d}{\beta_d}\sin(\beta_d h) + \frac{e_z^f}{\beta_f}\sin(\beta_f t)\right]^2 \tag{66}$$

Using (53) and (61) we can rewrite Equation (66) as follows

$$P_{out} = \frac{3}{8}|e_z^f|^2 G_c J_1^2(x)\cos^2(\beta_f t)\left[\frac{\varepsilon_f}{\varepsilon_d}\frac{\tan(\beta_d h)}{\beta_d} + \frac{\tan(\beta_f t)}{\beta_f}\right]^2 \tag{67}$$

For computing $U$ we can define

$$U_z^f = \frac{\varepsilon_f}{4}\int_{\Delta V}\left|E_z^f\right|^2 dv = \frac{\varepsilon_f}{4}\left|e_z^f\right|^2 I_{\rho 1} I_\varphi I_{z1} \tag{68}$$

$$U_z^d = \frac{\varepsilon_d}{4}\int_{V-\Delta V}\left|E_z^d\right|^2 dv = \frac{\varepsilon_d}{4}\left|e_z^d\right|^2 I_{\rho 1} I_\varphi I_{z3} \tag{69}$$

$$U_\varphi^f = \frac{\varepsilon_f}{4}\int_{\Delta V}\left|E_\varphi^f\right|^2 dv = \frac{\varepsilon_f}{4}\left|e_\varphi^f\right|^2 I_{\rho 2} I_\varphi I_{z2} \tag{70}$$

$$U_\varphi^d = \frac{\varepsilon_d}{4}\int_{V-\Delta V}\left|E_\varphi^d\right|^2 dv = \frac{\varepsilon_d}{4}\left|e_\varphi^d\right|^2 I_{\rho 2} I_\varphi I_{z4} \tag{71}$$

$$U_\rho^f = \frac{\varepsilon_f}{4}\int_{\Delta V}\left|E_\rho^f\right|^2 dv = \frac{\varepsilon_f}{4}\left|e_\rho^f\right|^2 I_{\rho 3} I_\varphi I_{z2} \tag{72}$$

$$U_\rho^d = \frac{\varepsilon_d}{4}\int_{V-\Delta V}\left|E_\rho^d\right|^2 dv = \frac{\varepsilon_d}{4}\left|e_\rho^f\right|^2 I_{\rho 3} I_\varphi I_{z4} \tag{73}$$

where $I_{\rho 1}$, $I_{\rho 2}$ and $I_{\rho 3}$ are defined in (A-1)-(A-3) and

$$I_\varphi = \int_0^{2\pi}\begin{Bmatrix}\cos^2(\varphi+30^\circ)\\ \sin^2(\varphi+30^\circ)\end{Bmatrix} d\varphi = \pi \tag{74}$$

$$I_{z1} = \int_h^b \cos^2(\beta_f(z-b))\,dz = \frac{t}{2} + \frac{1}{4\beta_f}\sin(2\beta_f t) \tag{75}$$

$$I_{z2} = \int_h^b \sin^2(\beta_f(z-b))\,dz = \frac{t}{2} - \frac{1}{4\beta_f}\sin(2\beta_f t) \tag{76}$$

$$I_{z3} = \int_0^h \cos^2(\beta_d z)\,dz = \frac{h}{2} + \frac{1}{4\beta_d}\sin(2\beta_d h) \tag{77}$$

$$I_{z4} = \int_0^h \sin^2(\beta_d z)\,dz = \frac{h}{2} - \frac{1}{4\beta_d}\sin(2\beta_d h) \tag{78}$$

$$U = 2(U_z^f + U_z^d + U_\varphi^f + U_\varphi^d + U_\rho^f + U_\rho^d) \tag{79}$$

 

By using (59) we can write

$$U_\varphi^f + U_\rho^f = \frac{\varepsilon_f}{4} I_\varphi I_{z2} \left[ \left| e_\varphi^f \right|^2 I_{\rho 2} + \left| e_\rho^f \right|^2 I_{\rho 3} \right]$$
$$= \frac{\varepsilon_f}{4} I_\varphi I_{z2} \left| e_\rho^f \right|^2 \left[ \frac{I_{\rho 2}}{k_c^{\,2}} + I_{\rho 3} \right] \quad (80)$$
$$= \frac{\varepsilon_f}{4} I_\varphi I_{z2} \left| e_\rho^f \right|^2 I_{\rho 1}$$

The last conclusion of equation (80) was made by (A-4). Using (60), in a manner analogous to equation (80), we can yield

$$U_\varphi^d + U_\rho^d = \frac{\varepsilon_d}{4} I_\varphi I_{z4} \left| e_\rho^d \right|^2 I_{\rho 1} \quad (81)$$

Then by (79)-(81) we can obtain

$$U = \frac{I_\varphi I_{\rho 1}}{2} \left\{ \varepsilon_f \left[ \left| e_z^f \right|^2 I_{z1} + \left| e_\rho^f \right|^2 I_{z2} \right] + \varepsilon_d \left[ \left| e_z^d \right|^2 I_{z3} + \left| e_\rho^d \right|^2 I_{z4} \right] \right\} \quad (82)$$

Using (75), (76), (53) and (59) we can expand the first expression in the energy Equation (82)

$$\varepsilon_f \left[ \left| e_z^f \right|^2 I_{z1} + \left| e_\rho^f \right|^2 I_{z2} \right] = \frac{\varepsilon_f}{2} \left| e_z^f \right|^2 \cos^2(\beta_f t) \times$$
$$\left[ t(1 + \frac{\beta_f^{\,2}}{k_c^{\,2}}) \sec^2(\beta_f t) + \frac{\tan(\beta_f t)}{\beta_f} - \frac{\beta_f \tan(\beta_f t)}{k_c^{\,2}} \right] \quad (83)$$

Also by (14) and (32) we can write

$$1 + \frac{\beta_f^{\,2}}{k_c^{\,2}} = \frac{\varepsilon_{rf} k_0^{\,2}}{k_c^{\,2}} = \frac{\varepsilon_{rf}}{\zeta} \quad (84)$$

$$1 + \frac{\beta_d^{\,2}}{k_c^{\,2}} = \frac{\varepsilon_{rd} k_0^{\,2}}{k_c^{\,2}} = \frac{\varepsilon_{rd}}{\zeta} \quad (85)$$

By using (77), (78), (60) and (61) we can expand the second expression in the energy Equation (82)

$$\varepsilon_d \left[ \left| e_z^d \right|^2 I_{z3} + \left| e_\rho^d \right|^2 I_{z4} \right] = \frac{\varepsilon_d}{2} \left| e_z^d \right|^2 \cos^2(\beta_d h) \times$$
$$\left[ h(1 + \frac{\beta_d^{\,2}}{k_c^{\,2}}) \sec^2(\beta_d h) + \frac{\tan(\beta_d h)}{\beta_d} - \frac{\beta_d \tan(\beta_d h)}{k_c^{\,2}} \right] \quad (86)$$

By (53), (61), (85) and (86) we have

$$\varepsilon_d \left[ \left| e_z^d \right|^2 I_{z3} + \left| e_\rho^d \right|^2 I_{z4} \right] = \frac{\varepsilon_f}{2} \left| e_z^f \right|^2 \cos^2(\beta_f t) \times$$
$$\left[ h \frac{\varepsilon_f}{\zeta} \sec^2(\beta_d h) + \frac{\varepsilon_f}{\varepsilon_d} \frac{\tan(\beta_d h)}{\beta_d} - \frac{\varepsilon_f}{\varepsilon_d} \frac{\beta_d \tan(\beta_d h)}{k_c^{\,2}} \right] \quad (87)$$

Substituting (83) and (87) in Equation (82) and by us ing (84) we reach (the last terms of (83) and (87) will be cancelled because of characteristic Equation (28))

$$U = \frac{I_\varphi I_{\rho 1}}{2} \frac{\varepsilon_f}{2} \left| e_z^f \right|^2 \cos^2(\beta_f t) \times$$
$$\left[ \frac{\varepsilon_{rf}}{\zeta} (t \sec^2(\beta_f t) + h \sec^2(\beta_d h)) + \frac{\tan(\beta_f t)}{\beta_f} \frac{\varepsilon_f}{\varepsilon_d} \frac{\tan(\beta_d h)}{\beta_d} \right] \quad (88)$$

Equation (88) is a closed formula for the energy stored in a cylindrical ferrite-dielectric resonator demonstrated in **Figure 3**. At this stage we have not only the analytical expression for energy, Equation (88), but also an analytical formula for the power delivered to the output port, equation (67). Then according to (62) the closed formula for the input conductance of the bared circulator is obtained (see Equation (89)).

To reach to the Equation (89) we also used the expressions for $I_\varphi$ and $I_{\rho 1}$ given in (74) and (A-1). In the practical cases in which the electrical length, $k_0 b$, is rather small, we can substitute sec functions by unity and tan functions by their arguments so the transcendental complexity in Equation (89) can be removed as follows

$$\frac{\varepsilon_{rf}}{\zeta} (t \sec^2(\beta_f t) + h \sec^2(\beta_d h)) + \frac{\tan(\beta_f t)}{\beta_f} + \frac{\varepsilon_f}{\varepsilon_d} \frac{\tan(\beta_d h)}{\beta_d}$$
$$\approx \frac{\varepsilon_{rf}}{\zeta} b + t + \frac{\varepsilon_f}{\varepsilon_d} h$$
$$= \varepsilon_{rf} \left( \frac{t/b}{\varepsilon_{rf}} + \frac{1 - (t/b)}{\varepsilon_{rd}} \right) b + t + \frac{\varepsilon_f}{\varepsilon_d} h$$
$$= 2(t + h \frac{\varepsilon_f}{\varepsilon_d}) \quad (90)$$

$$[\frac{\varepsilon_f}{\varepsilon_d} \frac{\tan(\beta_d h)}{\beta_d} + \frac{\tan(\beta_f t)}{\beta_f}]^2 \approx (\frac{\varepsilon_f}{\varepsilon_d} h + t)^2 \quad (91)$$

$$k_c^{\,2} = k_0^{\,2} \zeta = \frac{k_0^{\,2}}{\frac{t/b}{\varepsilon_{rf}} + \frac{1 - (t/b)}{\varepsilon_{rd}}} =$$
$$\frac{k_0^{\,2} b}{\frac{t}{\varepsilon_{rf}} + \frac{h}{\varepsilon_{rd}}} = \frac{\omega_0^{\,2} \mu_0 \varepsilon_f b}{t + \frac{\varepsilon_f}{\varepsilon_d} h} \quad (92)$$

$$G_c = \frac{\frac{\pi}{3}(x^2 - 1) \frac{\omega_0 \varepsilon_f}{k_c^{\,2}} [\frac{\varepsilon_{rf}}{\zeta} (t \sec^2(\beta_f t) + h \sec^2(\beta_d h)) + \frac{\tan(\beta_f t)}{\beta_f} + \frac{\varepsilon_f}{\varepsilon_d} \frac{\tan(\beta_d h)}{\beta_d}]}{Q \, [\frac{\varepsilon_f}{\varepsilon_d} \frac{\tan(\beta_d h)}{\beta_d} + \frac{\tan(\beta_f t)}{\beta_f}]^2} \quad (89)$$

 

Then using good approximations brought in (90)-(92), the input conductance given in (89) takes very simple form

$$G_c = \frac{2}{\sqrt{3}} \frac{pt}{f_0 \mu_0 b^2} \tag{93}$$

Equation (93) is the most important result of this paper and very useful to design the suitable matching network for the circulator.

## 6. Design Procedure for the Ferrite Film Circulator

In this section we summarize a procedure for designing an elevated stripline ferrite film circulator. In this design algorithm we use all the mathematical results in the previous sections.

### 6.1. Choosing the Operational Frequency and Suitable Ferrite Sample

The splitting factor in practical case must be located in the range $0.2 < |\kappa / \mu| < 0.5$. This condition limits our choice of ferrite sample for our desired operational frequency because of Equation (2). Then if we choose a central frequency for operation of circulator, our ferrite sample should have a saturation magnetization so that according to Equation (2), the splitting factor is located in the mentioned interval.

### 6.2. Choosing the Substrate and the Thickness of Ferrite and Dielectric Layers

In the next section we discuss about the permittivity mismatch for ferrite and dielectric layers. Also the overall thickness of ferrite and dielectric layers must be rather small to be a practical case in MICs. For a rule of thumb $k_0 b < 2\pi / 40$ is a suitable choice. In most practical cases the permittivity of ferrite is more than that of the dielectric layer. To have a miniaturized circulator size, it is not appropriate to choose a low permittivity for dielectric substrate.

### 6.3. Determining the Radius of Ferrite Cylinders

If the electrical thickness of ferrite and dielectric layers is small, the algebraic formula for effective permittivity, Equation (36), can be very useful. Then the radius of ferrite cylinders are found using Equation (29) or equivalently

$$R = 1.841 / (k_0 \sqrt{\zeta}) \tag{94}$$

### 6.4. Determining the Input Conductance for the Bare Circulator

For the bare circulator (*i.e.* the circulator without stripline ports) provided the overall thickness of layers is small, we can use simple Equation (93) to find the input conductance of the bare circulator. This input conductance, indeed is the reciprocal value of the reference impedance for which the scattering parameters for the three-port takes the form of the scattering parameters of a good circulator (*i.e.* with low insertion loss, high isolation and high return loss)

### 6.5. Determining the Suitable Matching Network

The necessary quarter wave matching transformer impedance, $Z_T$, as shown in **Figure 1** to match the circulator to $50\ \Omega$ lines is then

$$Z_T = \sqrt{50 / G_c} \tag{95}$$

To find the width of the striplines, we can use Microwave Softwares. For example MWOFFICE [24] is a useful software.

**Table I** shows the design parameters for an elevated substrate ferrite junction circulator using the above procedure.

## 7. Numerical Results

In this section, first we verify the correctness and accuracy of our formula, Equation (93), for the input conductance of the stripline ferrite film circulator using HFSS [19] simulations. By HFSS we can find the scattering

**Table 1. Design data for an elevated substrate ferrite film circulator.**

| Quantity | Comment | Value |
|---|---|---|
| $f_0$ | --- | 4 GHz |
| $t$ | --- | 0.5 mm |
| $h$ | --- | 0.5 mm |
| $\varepsilon_{rf}$ | G-610 ferrite[1] | 14.5 |
| $4\pi M_S$ | --- | 680 G |
| $\varepsilon_{rd}$ | sapphire | 9 |
| $p$ | Eq. (2) | 0.476 |
| $\zeta$ | Eq. (36) | 11.1 |
| $\beta_f$ | Eq. (33) | 154.5 Rad/s |
| $\beta_d$ | Eq. (34) | -j121.4 |
| $R$ | Eq. (94) | 6.6 mm |
| $\lambda_g / 4$ | $\lambda_g = 2\pi / (k_0 \sqrt{\varepsilon_{rd}})$ | 6.25 mm |
| $Q^{-1}$ | Eq. (46) or (47) | 0.345 |
| $G_c$ | Eq. (75) or (93) | 0.0547 mho |
| $Z_T$ | Eq. (95) | 30 ohm |
| $W$ (width of stripline) | TXLINE [24] | 1.2 mm |

[1] We neglect the line-width $\Delta H$.

 

parameters of the bare circulator for each reference impedance, $Z_{ref}$, of the ports. The scattering parameters are the functions of reference impedance. Indeed the input conductance, $G_c$, is the reciprocal value of the reference impedance for which the return loss and isolation are maximum and insertion loss is minimum. We call this suitable reference impedance as $Z_{ref,c}$. By this criterion we can know whether $G_c^{-1}$ is near to $Z_{ref,c}$ or not. Return loss, insertion loss and isolation are depicted in **Figure 5** versus $Z_{ref}$ for an elevated substrate ferrite circulator for different permittivites of the dielectric layer. According to these simulations, we can see that $G_c^{-1}$ is very close to $Z_{ref,c}$ and their difference is only in few ohms. So Equation (93) is a very good analytical formula for designing the matching network for an elevated ferrite film circulator.

The next thing we can verify numerically is the role of the thickness of ferrite film, effectively shown by, $t/b$, on the bandwidth of the scattering parameters. Hartwig and Readey [14] reported that as ferrite thickness is increased, the bandwidth is improved but we lose the integration of our device. So we encounter with a trade-off. In **Figure 6** the frequency behavior of the scattering parameters of the ferrite film circulator are demonstrated for some values of $t/b$. This results show that to in-crease the bandwidth of the device, the ferrite thickness should be increased but we should not miss the miniaturization for our purpose. Another problem that is caused by low value of $t/b$ is the reduction of the width of the ports. This is a bottle-neck in fabrication because the absolute error in fabricating the striplines with small width is limited.

The last numerical result is the effect of dielectric mismatch for ferrite and dielectric layers on the bandwidth of the device. **Figure 7** shows the frequency behavior of the scattering parameters of the ferrite film circulator for some dielectrics. Roughly we can say as the permittivity of the dielectric layer increases not only the bandwidth goes up but also we keep the integration of the device.

The concept and formulations developed in this paper allow successful design of the matching network with the use of simple formula for the input conductance for a bared miniaturized elevated ferrite film circulator. Although a simple quarter wavelength transformer is utilized here, our formulation can be applied to other general matching networks to obtain a wider band circulator. Other aspects such as having different ferrite materials for the lower and upper part of the metal disk, can demonstrate desired flexibility to have a wide band circulator. Further designs considering the fabrication realization are in progress.

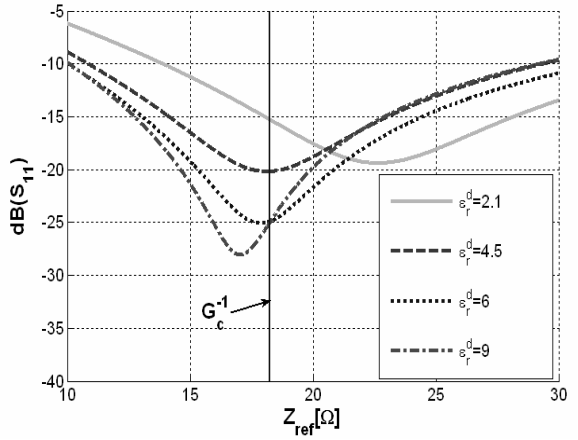


(a)

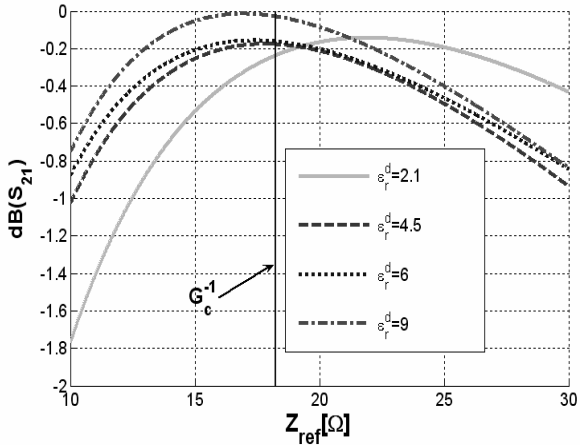


(b)

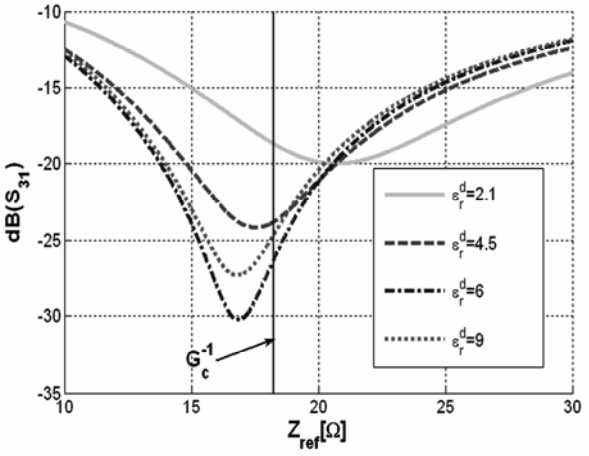


(c)

**Figure 5. Scattering parameters for an elevated ferrite film circulator versus reference impedance for $k_0 b = 2\pi/75$, $\varepsilon_{rd} = 2.1, 4.5, 6$ and 9, $\varepsilon_{rf} = 14.5$, $4\pi M_S = 680$ Gauss, $b = 1$ mm and $f_0 = 4$ GHz**

**(a) Return loss; (b) Insertion loss; (c) Isolation.**

 

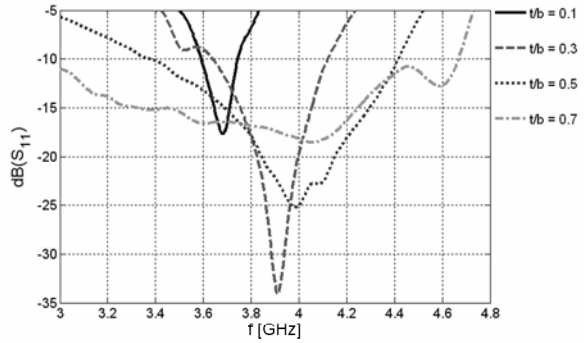


(a)

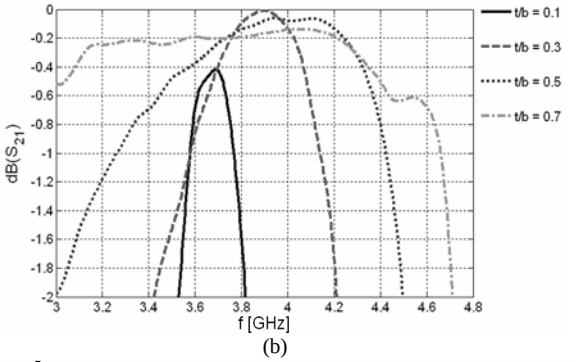


(b)

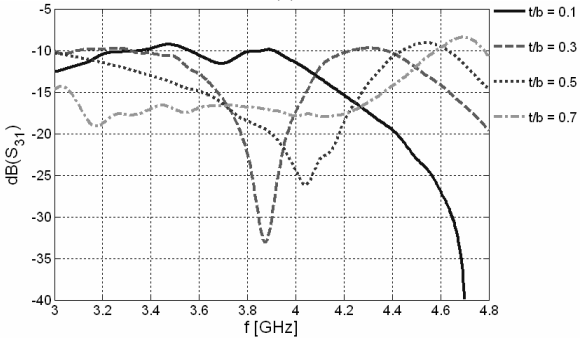


(c)

**Figure 6. Frequency behavior of the scattering parameters for an elevated ferrite film circulator for $t/b = 0.1$, 0.3, 0.5 and 0.7 , $k_0 b = 2\pi/75$ , $\varepsilon_{rd} = 9$ , $\varepsilon_{rf} = 14.5$ , $4\pi M_S = 680$ Gauss , $b = 1$ mm and $f_0 = 4$ GHz (a) Return loss (b) Insertion loss (c) Isolation.**

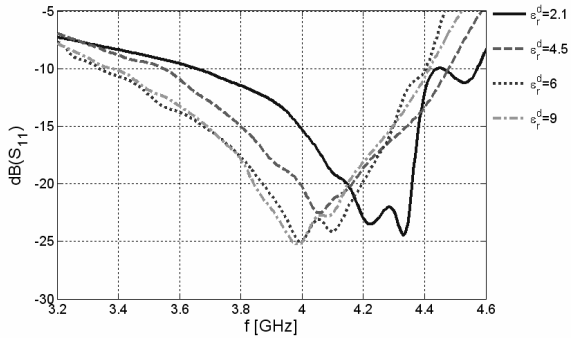


(a)

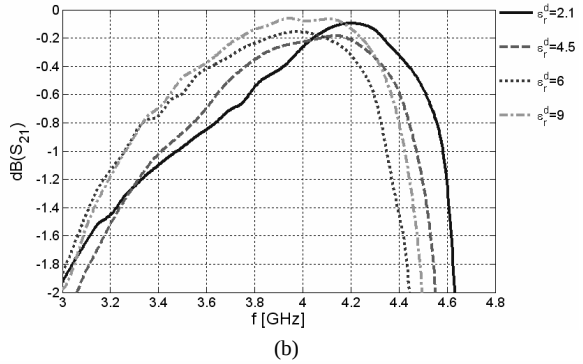


(b)

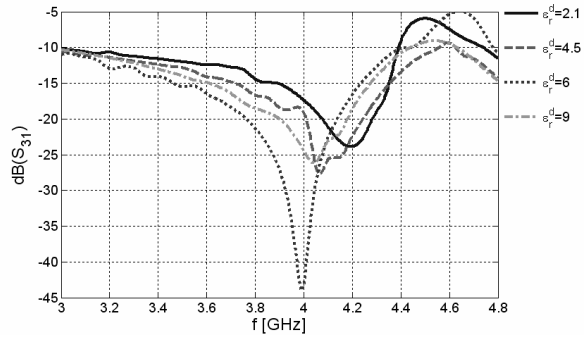


(c)

**Figure 7. Frequency behavior of the scattering parameters for an elevated ferrite film circulator for $t/b = 0.5$ , $\varepsilon_{rd} = 2.1$, 4.5, 6 and 9 , $k_0 b = 2\pi/75$ , $\varepsilon_{rf} = 14.5$ , $4\pi M_S = 680$ Gauss , $b = 1$ mm and $f_0 = 4$ GHz (a) Return loss (b) Insertion loss (c) Isolation.**

## 8. Conclusions

This paper is a complementary to the study of elevated substrate ferrite film circulators. After 40 years of introducing the elevated ferrite film circulator, we answered the question of how we can find the input conductance of the elevated circulator to design a matching network not with trial and error or with approximated formulas which were used 40 years ago. We showed that how a long analytical formulation can end up with a simple formula for the input conductance of the miniaturized ferrite-dielectric circulator. The simple formula depends to the ferrite and dielectric thickness and the splitting factor. We followed circuit approach as well as electromagnetic approach in our design route by successfully employing perturbation method. The procedure to obtain such formula had a lot of mathematical complexity due to perturbation integrals and finding the electromagnetic fields profile in ferrite loaded resonator. The transcendental nature of the result was simplified in the practical case that the electrical thickness of ferrite and dielectric layers is rather small. Finally we verified our analytical result by numerical simulations.

 

The formulation presented in this paper also can be applied for a multi-layer ferrite structure including more than two layers in each side of the metal disk. The layers can be dielectrics and ferrites with different characteristics. The formulation illustrated in this paper can be applicable not only for stripline but also for microstrip circulators. In microstrip case we need to consider just one ferrite dielectric loaded resonator instead of two resonators. Other matching networks in different configurations can be utilized to match the bare circulator by using the input conductance formula presented in this paper. The proposed technique in this paper enables a capable approach for designing elevated substrate circulators with the use of energy integrals, and perturbation technique presented in this paper.

## 9. Acknowledgements

The authors would like to thank the help and discussion of Professor Carmine Vittoria in Northeastern University.

## REFERENCES

[1] H. C. Wu and W. B. Dou, "Field Structures of Waveguide Junction Circulators with Irregular Shaped Ferrite Simulated Based on Exact Treatment," *Progress in Electromagnetics Research*, Vol. 57, 2006, pp. 33-54.

[2] J. Helszajn, "Reflection Angles of In-Phase and Split Counter-Rotating Eigenvalues of the Three-Port Circulator," *IEEE Transactions on Microwave Theory and Techniques*, Vol. 54, No. 3, March 2006, pp. 1076-1083.

[3] E. Benevent, T. Rouiller, B. Sauviac, V. Larrey, D. Vincent and A. Madelaine, "Stripline Y-Junction Circulator Using Barium Hexagonal Ferrite Thin Films," *IEEE International Symposium on Industrial Electronics*, Vol. 1, No. 1, May 2004, pp. 15-18.

[4] J. L. Young and J. W. Sterbentz, "The Circular Homogeneous-Ferrite Microwave Circulator—An Asypmtotic Green's Function and Impedance Analysis," *IEEE Transactions on Microwave Theory and Techniques*, Vol. 51, No. 8, August 2003, pp. 1939-1945.

[5] P. Shi, H. How, X. Zuo, S. A. Oliver, N. E. McGruer and C. Vittoria, "MMW Monolithic Y-Junction Circulator on Single-Crystal Sc-Doped Ba-Hexaferrite," *IEEE MTT-S International Microwave Symposium Digest*, Boston, Vol. 2, 2000, pp. 909-912.

[6] J. D. Adam, L. E. Davis, G. F. Dionne, E. F. Schloemann, and S. N. Stitzer, "Ferrite Devices and Materials," *IEEE Transactions on Microwave Theory and Techniques*, Vol. 50, No. 3, March 2002, pp. 721-737.

[7] R. E. Blight and E. Schloemann, "A Compact Broadband Microstrip Circulator for Phased Array Antenna Modules," *IEEE MTT-S International Microwave Symposium Digest*, Albuquerque, Vol. 3, June 1992, pp.1389-1392.

[8] S. L. Karode and V. F. Fusco, "Feedforward Embedding Circulator Enhancement in Transmit/Receive Applications," *IEEE Microwave and Guided Wave Letters*, Vol. 8, No. 1, January 1998, pp. 33-34.

[9] H. Bosma, "On Strip Line Y-Circuation at UHF," *IEEE Transactions on Microwave Theory and Techniques*, Vol. 12, No. 1, January 1964, pp. 61-72.

[10] C. E. Fay, and R. L. Comstock, "Operation of the Ferrite Junction Circulator," *IEEE Transactions on Microwave Theory and Techniques*, Vol. 13, No. 1, January 1965, pp. 15-27.

[11] H. J. Butterweck, "Der Y Zirkulator," *Arch. Elektron. Uebertragung.*, Vol. 17, April 1963, pp. 163-176.

[12] H. How, S.W. McKnight and C. Vittoria, "Effective-Field Theory for Ferrite Thin-Film Junction Circulator," *IEEE MTT-S International Microwave Symposium Digest*, Denver, Vol. 2, June 1997, pp. 1127-1130.

[13] R. R. Jones, R. A. Moore, A. I. Braginski and T. R. Oeffinger, "Elevated Substrate Ferrite Film Circulator," *IEEE GMTT International Microwave Symposium*, Arlington Heights, 1972, pp. 241-242.

[14] C. P. Hartwig and D. W. Readey, "Ferrite Film Circulator," *Journal of Applied Physics*, Vol. 41, No. 3, March 1970, pp. 1351-1352.

[15] L. K. Anderson, "An Analysis of Broadband Circulators with External Tuning Elements," *IEEE Transactions on Microwave Theory and Techniques*, Vol. 15, No. 1, January 1967, pp. 42-47.

[16] K. Oshiro, T. Noborio, H. Fujimori, H. Mikami, S. Fujii, M. Matsuura and S. Yamamoto, "Design of a Circulator with Ferrite Thin Film," *Journal of the Magnetics Society of Japan*, Vol. 29, No. 4, 2005, pp. 490-493.

[17] J. Helszajn, "Experimental Evaluation of Junction Circulators: A Review," *IEE Proceedings on Microwaves, Antennas and Propagation*, Vol. 141, No. 5, October 1994, pp. 351-358.

[18] J. Helszajn, "Scattering Matrices of Junction Circulator with Chebyshev Characteristics," *IEEE Transactions on Microwave Theory and Techniques*, Vol. 23, No. 7, July 1975, pp. 548- 554.

[19] HFSS. ver. 9.1, Ansoft Corporation, Pittsburg, 2003.

[20] Y. S. Wu, "Wide-Band Operation of Microstrip Circulators," *IEEE Transactions on Microwave Theory and Techniques*, Vol. 22, No. 10, October 1974, pp. 849-856.

[21] R. F. Harrington, "Time Harmonic Electromagnetic Fields," IEEE Press, USA, 2001.

[22] D. M. Pozar, "Microwave Engineering," 3rd Edition, Addison-Wesley, USA, 2005.

[23] B. Lax and K. J. Button, "Microwave Ferrites and Ferrimagnetics," McGraw-Hill, New York, 1962.

[24] AWR Design Environment, ver. 6.51, Applied Wave Research, 2005.

 

## Appendix: Useful Integrals Involving Bessel Functions

$$I_{\rho 1}=\int_0^R J_1^{\,2}(k_c\rho)\rho d\rho=\frac{1}{2k_c^{\,2}}(x^2-1)J_1^{\,2}(x) \qquad \text{(A-1)}$$

$$I_{\rho 2}=\int_0^R \frac{J_1^{\,2}(k_c\rho)}{\rho}d\rho=\frac{1}{4}[2-J_1^{\,2}(x)-(2+x^2)J_0^{\,2}(x)] \qquad \text{(A-2)}$$

$$I_{\rho 3}=\int_0^R J_1'^{2}(k_c\rho)\rho d\rho=\frac{1}{4k_c^{\,2}}[(2x^2-1)J_1^{\,2}(x)+(2+x^2)J_0^{\,2}(x)-2] \qquad \text{(A-3)}$$

$$\frac{I_{\rho 2}}{k_c^{\,2}}+I_{\rho 3}=I_{\rho 1} \qquad \text{(A-4)}$$

 

*J. Electromagnetic Analysis & Applications*, **2010, 2, 543-548**
doi:10.4236/jemaa.2010.29070 Published Online September 2010 (http://www.SciRP.org/journal/jemaa)

# Analysis of Reflection Properties of High Power Microwave Propagation in Mixture-Atmosphere

**Tao Tang, Cheng Liao, Qingmin Gao, Pengcheng Zhao**

Institution of Electromagnetics, Southwest Jiaotong University, Chengdu, China
Email: ttang@foxmail.com, c.liao@home.swjtu.edu.cn, kaocaomin@163.com, zhaopengcheng19860@163.com

Received June 3rd, 2010; revised July 21st, 2010; accepted July 21st, 2010

## ABSTRACT

*A simple theoretical modeling is made to describe the reflection features of the high power microwave (HPM) in the mixture-atmosphere. The time-space dependent mixture-atmosphere is generated by ionization of the neutral molecules in atmosphere. Reflection will occur when HPM propagates in such mixture-atmosphere. The reflection characteristic of the HPM propagation in the mixture-atmosphere is investigated by FDTD numerical experiments in inhomogeneous medium, the influence on the reflection for different HPM parameters is concluded. An additional stability conditions for the FDTD difference scheme of the HPM mixture-atmosphere propagation model are presented.*

***Keywords*: *High Power Microwave, Reflection Properties, Mixture-Atmosphere***

## 1. Introduction

When high power microwave (HPM) pulse propagates in atmosphere, the breakdown will occur if the corresponding region where the breakdown threshold is lower than the HPM electric field intensity. The free electrons which exist in the atmosphere are accelerated, the impact ionization is expected to occur when those accelerated electrons interacts with the neutral molecules, this process generates new electrons, the new electrons will be accelerated and the impact ionization will occur again, engendering more electrons. Due to the chain ionization, the electron density in the atmosphere rise sharply in a short time and space-time dependent plasma is formed [1]. The plasma will have some negative impacts on the HPM, bringing some nonlinear effects, such as reflection, absorption attenuation and etc. Because of the pulse width is limited, and it will take some time for the electrons produced by ionization reach the density which can significantly absorb the pulse, but before that time, the leading edge of the pulse has passed, and therefore, the attenuation occurs only in the tail. This mechanism is called as "tail erosion" [1]. Some theoretical and experimental work has been reported in the past few years. Woo and DeGroot [2] obtained the kinetic and hydrodynamic description of this problem by reduced the Boltzmann equation. Ali [3] has investigated the breakdown parameters for very high values of E/p. Kuo and Zhang [4] conducted a chamber experiment and identified tow mechanisms responsible for tow different degree of tail erosion. Yee *et al*. [5,6] developed one-dimensional codes to investigate the dynamic behavior of short-pulse by using electron fluid equations and Maxwell's equations self-consistently.

When air is breakdown, the density is so high that the atmosphere will be turned into the plasma and non-plasma mixture-atmosphere. HPM propagates in the mixture-atmosphere, the reflection will occur, if the reflection is strong, there will have a negative impact on the HPM source device, even damages like airborne high-power radar or other HPM equipments.

In this paper, we report the results of a theoretical and numerical study of HPM reflection properties. Taking into account of the differential thinking, we treat the mixture-atmosphere as a layered inhomogeneous medium. And using FDTD method [7] in inhomogeneous medium, we computationally investigate the reflection characteristics of the HPM pulse in mixture-atmosphere; the stability conditions for the FDTD difference scheme of the HPM atmosphere propagation model are derived.

The paper is organized as following. In Section 2, the HPM propagation model in mixture-atmosphere is introduced, and its stability condition is presented. Section 3 presents the stability condition for FDTD difference scheme. Section 4 discusses the reflection properties of HPM propagation in the mixture-atmosphere. Conclusions are drawn in Section 5.

 

## 2. Propagation Model in Inhomogeneous Medium

### 2.1. Transmission Line Model for Inhomogeneous Medium

The mixture-atmosphere which is composited by plasma and non-plasma will be counterproductive in the HPM to make the occurrence of attenuation. The attenuation will weaken the ionization, therefore, the electron density decreases along the wave propagation direction, and the mixture-atmosphere is not uniform. Taking into account of the differential thinking, the mixture-atmosphere can be discretized as a multi-layer medium approximation model which distributes along the propagation direction. The setup of this model is shown in **Figure 1(a)**. If the division of each layer is small enough, the medium within each layer can be regarded as homogeneous medium, the dielectric of each layer is a constant.

According to the transmission line model, the propagation of electromagnetic waves along the z axis can be equivalent to the cascaded transmission line. By making this equivalent, respectively the reflection, transmission and other law for electromagnetic wave propagation in the layered medium can be obtained [8]. The $k_i$ and $Z_i$ in **Figure 1** is the wave vector and wave impedance.

### 2.2. The FDTD Difference Scheme of HPM in Mixture-Atmosphere

The HPM atmosphere propagation model consists of Maxwell's equations and the electron fluid equations which are reduced from the Boltzmann equation [4-6].

$$\nabla \times \mathbf{E} = -\frac{\partial \mathbf{B}}{\partial t} \tag{1}$$

$$\nabla \times \mathbf{H} = en_e\mathbf{u} + \frac{\partial \mathbf{D}}{\partial t} \tag{2}$$

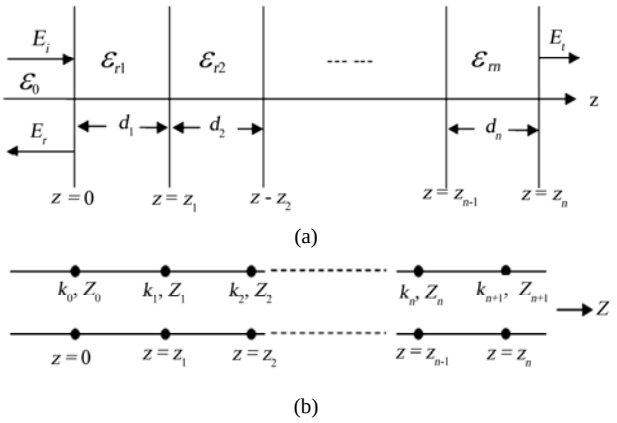


**Figure 1. The schematic diagram of layered medium model for mixture-atmosphere (a) and equivalent circuit (b).**

$$\frac{\partial n_e}{\partial t} = \left(v_i - v_a\right) n_e \tag{3}$$

$$m\frac{\partial \left(n_e\mathbf{u}\right)}{\partial t} = en_e\mathbf{E} - n_e m v_c \mathbf{u} \tag{4}$$

where (1) and (2) are the Maxwell's equations in the case of atmosphere. The avalanche ionization makes the number of free electrons increase rapidly. Equation (3) is the electron density continuity equation. Equation (4) is the electron momentum conservation equation in the fluid model. **E** is the electric field, **B** is the magnetic induction, **H** is the magnetic field, **D** is the displacement vector, $n_e$ and **u** is the density and velocity of electronic fluid, respectively; $v_i$, $v_a$ and $v_c$ are the ionization, attachment and collision rate coefficients; $e$ and $m$ denote the charge and mass of electronic, respectively.

In one dimensional model, the scalar forms of (1) and (2) in the inhomogeneous medium can be rewritten as

$$\frac{\partial E_x}{\partial t} = -v(z)Z(z)\frac{\partial H_y}{\partial z} - v(z)Z(z)enu_x \tag{5}$$

$$\frac{\partial H_y}{\partial t} = -\frac{v(z)}{Z(z)}\frac{\partial E_x}{\partial z} \tag{6}$$

In which $v(z) = 1/\sqrt{\varepsilon_r \mu}$, $Z(z) = \sqrt{\mu/\varepsilon_r}$ are the wave velocity and wave impedance of the medium, respectively. $\mu$ is the permeability and $\varepsilon_r$ is the relative permittivity of mixture-atmosphere, which can be modeled as [9].

$$\sqrt{\varepsilon_r} = n_n - \frac{40.308\times10^{-12} n_e}{n_n f^2} \tag{7}$$

where $n_n$ is the refraction index of non-ionizing atmosphere.

$$n_n = 1 + \frac{77.6\times10^{-6}}{T}\left(p + \frac{4810\,p_e}{T}\right) \tag{8}$$

where $T$ is the atmosphere temperature in K; $p$ and $p_e$ are pressure and water vapor pressure in hPa, respectively; $f$ is the microwave frequency in Hz; and $n_e$ is electron density in $m^{-3}$. By discrete Equation (3), the changes of the electron density can be obtained; the related work can be found in [10]. The initial electron density is defined follows [11]

$$n_{e0} = \begin{cases} 10 & (h < 25km) \\ 8\times10^7 \times \left(h/60\right)^{18} & (h \geq 25km) \end{cases} \tag{9}$$

According to the Courant stability condition for the FDTD simulation, we have $v(z)\Delta t \leq \Delta z$ for the case of inhomogeneous medium. In order to meet this condition, the maximum wave velocity of the medium must be satisfied. Another stability condition must be met when use FDTD to solve the problem of HPM atmosphere propagation, which will be presented in the next Section.

 

## 3. Additional Stability Condition

### 3.1. Stability Condition

The scalar equations of the (1)-(4) can be discretized by central difference method in the time step and spatial step. The FDTD difference scheme for these equations in one dimensional model can be written as

$$E_x^{n+1}(i)=E_x^n(i)-\frac{\Delta t}{\varepsilon_r\Delta z}\left[H_y^{n+\frac{1}{2}}(i+\frac{1}{2})-H_y^{n+\frac{1}{2}}(i-\frac{1}{2})\right]+\frac{e\Delta t}{4\varepsilon_r}\left[n_e^{n+1}(i)+n_e^n(i)\right]\cdot\left[u_x^{n+\frac{1}{2}}(i+\frac{1}{2})+u_x^{n+\frac{1}{2}}(i-\frac{1}{2})\right] \tag{10}$$

$$H_y^{n+\frac{1}{2}}\left(i+\frac{1}{2}\right)=H_y^{n-\frac{1}{2}}\left(i+\frac{1}{2}\right)-\frac{\Delta t}{\mu\Delta z}\left[E_x^n\left(i+1\right)-E_x^n\left(i\right)\right] \tag{11}$$

$$n_e^{n+1}\left(i\right)=\left[\left(1+\frac{\Delta t\left(v_i-v_a\right)}{2}\right)\Big/\left(1-\frac{\Delta t\left(v_i-v_a\right)}{2}\right)\right]n_e^n\left(i\right) \tag{12}$$

$$u_x^{n+\frac{1}{2}}\left(i+\frac{1}{2}\right)=\left[\left(1-\frac{\Delta tv_c}{2}\right)\Big/\left(1+\frac{\Delta tv_c}{2}\right)\right]u_x^{n-\frac{1}{2}}\left(i+\frac{1}{2}\right)+\frac{e\Delta t}{m\left(2+\Delta tv_c\right)}\cdot\left[E_x^n\left(i+1\right)+E_x^n\left(i\right)\right] \tag{13}$$

where the superscript $n$ is the time steep and $i$ is the space steep. When the air is breaking down, the electron density is so high that the HPM will be reflected and absorbed, the microwave will decay quickly in the mixture-atmosphere which leads to the role of ionization $v_i$ decreases quickly and the electron adhesion $v_a$ plays a dominant role. But $v_a$ is so small that the electron density remains almost unchanged. Therefore, equation (12) is stable.

In order to investigate the stability for the FDTD scheme of other equations, we expand the electromagnetic wave into plane wave spectrum, and we have

$$E_x^n\left(i\right)=E_0\exp\left[-j_0\left(ik_z\Delta z-n\omega\Delta t\right)\right] \tag{14}$$

$$H_y^{n+\frac{1}{2}}\left(i+\frac{1}{2}\right)=H_0\exp\left[-j_0\left((i+\frac{1}{2})k_z\Delta z-(n+\frac{1}{2})\omega\Delta t\right)\right] \tag{15}$$

Because the electron fluid velocity equation is only coupled with the electric field strength $\mathbf{E}$. Therefore, the electron fluid velocity equation becomes a first-order linear differential equation, and its solution can be written as follows

$$u_x=\frac{e\left(j\omega+v_c\right)}{m}E_x \tag{16}$$

Substituting (14) into (16), we have

$$u_x^{n+\frac{1}{2}}\left(i+\frac{1}{2}\right)=u_0\exp\left[-j_0\left((i+\frac{1}{2})k_z\Delta z-(n+\frac{1}{2})\omega\Delta t\right)\right] \tag{17}$$

On the other hand, we can plug (14) and (15) into the (11), after simplified, we have

$$-\frac{\Delta t}{\mu\Delta z}E_0\left[\exp\left(-j_0k_z\Delta z\right)-1\right]=H_0\exp\left(-j_0\frac{1}{2}k_z\Delta z\right)\cdot\left[\exp\left(j_0\frac{1}{2}\omega\Delta t\right)-\exp\left(-j_0\frac{1}{2}\omega\Delta t\right)\right] \tag{18}$$

In (18), the term $\exp\left(-j_0k_z\Delta z\right)-1$ can be rewritten as follows

$$\exp\left(-j_0k_z\Delta z\right)-1=\exp\left(-j_0\frac{1}{2}k_z\Delta z\right)\cdot\left[\exp\left(-j_0\frac{1}{2}k_z\Delta z\right)-\exp\left(j_0\frac{1}{2}k_z\Delta z\right)\right] \tag{19}$$

Combining (18) and (19), we can obtain

$$H_0=\frac{\Delta t\sin\left(\frac{1}{2}k_z\Delta z\right)}{\mu_0\Delta z\sin\left(\frac{1}{2}\omega\Delta t\right)}E_0 \tag{20}$$

Similarly, combining (17) and (14), after tedious simplification, we can rewrite (13) as follows

$$u_0\exp\left(-j_0\frac{1}{2}k_z\Delta z\right)\exp\left(j_0\frac{1}{2}\omega\Delta t\right)-u_0\exp\left(-j_0\frac{1}{2}k_z\Delta z\right)\left[\left(1-\frac{\Delta tv_c}{2}\right)\Big/\left(1+\frac{\Delta tv_c}{2}\right)\right]\cdot\exp\left(-j_0\frac{1}{2}\omega\Delta t\right)=\frac{E_0e\Delta t}{m\left(2+\Delta tv_c\right)}\left\{\exp\left[-j_0\left(k_z\Delta z\right)\right]+1\right\} \tag{21}$$

Taking the collision frequency $v_c$ into account, the time step should meet the following condition [12]

$$\Delta t\le 1\Big/10v_c \tag{22}$$

Then we have

$$\frac{1-\Delta tv_c\Big/2}{1+\Delta tv_c\Big/2}\approx 1 \tag{23}$$

At the same time, the term $\exp\left[-j_0\left(k_z\Delta z\right)\right]+1$ in (21) can be rewritten as follows

$$\exp\left[-j_0\left(k_z\Delta z\right)\right]+1=\exp\left(-j_0\frac{1}{2}k_z\Delta z\right)\cdot\left[\exp\left(-j_0\frac{1}{2}k_z\Delta z\right)+\exp\left(j_0\frac{1}{2}k_z\Delta z\right)\right] \tag{24}$$

 

Therefore, considering (23) and (24), (21) can be further simplified as follow

$$u_0 = j\frac{e\Delta t\cos\left(\frac{1}{2}k_z\Delta z\right)}{m\left(2+v_c\Delta t\right)\sin\left(\frac{1}{2}\omega\Delta t\right)}E_0 \tag{25}$$

As discussed above, when the air is breakdown, the electron density will reach a maximum value $n_{\max}$, and then remains almost unchanged [2,12,13]. So we can take the place of $n_e^{n+1}$ and $n_e^n$ in (10) with $n_{\max}$. Combining (14), (15) and (17), after tedious simplification, we finally obtain from (11)

$$\begin{aligned} j\sin\left(\frac{1}{2}\omega\Delta t\right)E_0 &= \frac{\Delta t}{\varepsilon_r\Delta z}\cdot j\sin\left(\frac{1}{2}k_z\Delta z\right)H_0 \\ &+\frac{en_{\max}\Delta t}{2\varepsilon_r}\cos\left(\frac{1}{2}k_z\Delta z\right)u_0 \end{aligned} \tag{26}$$

Substituting (20) and (25) into (26), we have

$$\frac{\sin^2\left(\frac{1}{2}\omega\Delta t\right)}{\Delta t^2} = \frac{\sin^2\left(\frac{1}{2}k_z\Delta z\right)}{\varepsilon_r\mu\Delta z^2} + \frac{e^2n_{\max}\cos^2\left(\frac{1}{2}k_z\Delta z\right)}{2\varepsilon_r m\left(2+v_c\Delta t\right)} \tag{27}$$

With the use of the propagation constant $k_z = \omega\sqrt{\varepsilon_r\mu}$ and (22), (27) can be written as

$$\frac{\omega^2}{4}\left(\frac{\sin^2\left(\frac{1}{2}\omega\Delta t\right)}{\left(\frac{1}{2}\omega\Delta t\right)^2} - \frac{\sin^2\left(\frac{1}{2}k_z\Delta z\right)}{\left(\frac{1}{2}k_z\Delta z\right)^2}\right) = \frac{e^2n_{\max}\cos^2\left(\frac{1}{2}k_z\Delta z\right)}{4\varepsilon_r m} \tag{28}$$

Follow the same derivation of the Courant condition, we can obtain

$$\Delta t \le \frac{1}{v(z)}\left(\frac{1}{\Delta z^2} + \frac{e^2\mu n_{\max}}{4m}\right)^{-1/2} \tag{29}$$

This stability condition is similar to the result given in Ref. [14].

### 3.2. Calculation Results

In order to illustrate our analysis, a numerical example is presented. We set the field intensity of the incident sinusoidal HPM source is $1\times10^5$ V/m, the center frequency is 1GHz and the pulse width is 50ns. It is transmitted vertically from the altitude of 35 km; **Figure 2** records its time domain waveform of different altitude and the corresponding electron density. In order for clear comparison, we shift the time when the wave pulse just reaches the corresponding position to zero. Obviously, our numerical results well agrees with the earlier literature results.

As the previous analysis, when the breakdown is occurring, the electron density grows exponentially in time quickly, the density is so high that the HPM will be reflected and absorpted, the microwave will decay quickly. This leads ionization decreases quickly and the electron adhesion plays a dominant role, therefore, the electron density will decreases slowly. Therefore, the use of FDTD in the case of inhomogeneous medium to deal with the problem of HPM atmosphere propagation is reasonable.

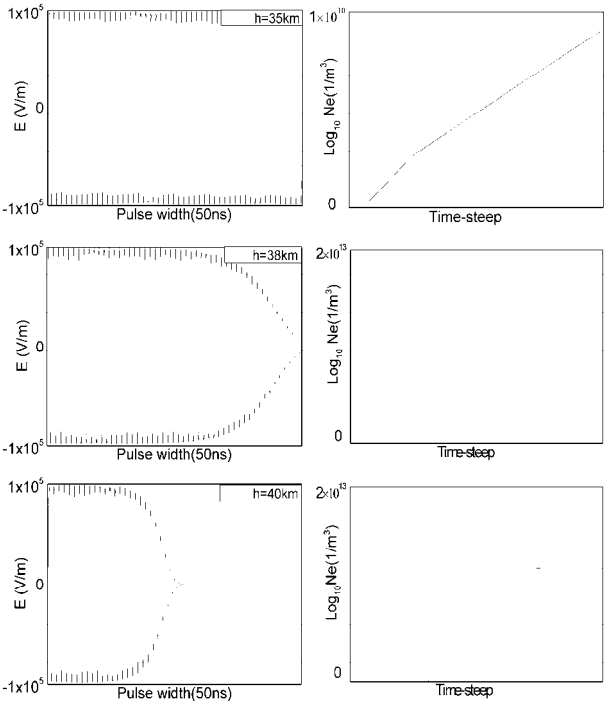


**Figure 2. HPM decay in a mixture-atmosphere and the electron density of the corresponding position.**

## 4. Reflection in the Mixture-Atmosphere

The air breakdown makes the atmosphere change into an inhomogeneous medium; HPM will be reflected on the surface of each layer of the mixture-atmosphere. In order to investigate the HPM reflection, the propagation area is divided into scattering field and the total field area, which shows in **Figure 3**.

According to the FDTD total field boundary conditions [15], adding a corresponding equivalent current at the total field outer boundary and a magnetic current at the total field boundary as incident wave of the tangential field components, while the normal component remains unchanged, that is

$$\begin{aligned} H_y^{n+1/2}(i-1/2) &= H_y^{n-1/2}(i-1/2) \\ -\frac{c(z)}{Z(z)}\frac{\Delta t}{\Delta z}&\left[E_x^n(i)-E_x^n(i-1)\right]+\frac{c(z)}{Z(z)}\frac{\Delta t}{\Delta z}E_i^n(i) \end{aligned} \tag{30}$$

 

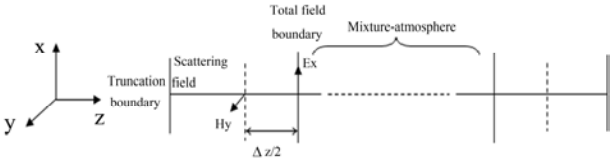


**Figure 3. Regional division: Scattering Fields.**

$$E_x^{n+1}(i) = E_x^n(i) - c(z)Z(z)\frac{\Delta t}{\Delta z}\left[H_y{}^{n+1/2}(i+1/2) - H_y{}^{n+1/2}(i-1/2)\right] - c(z)Z(z)e\Delta t U_x^{n+1/2}(i+1/2) + c(z)Z(z)\frac{\Delta t}{\Delta z}H_i^{n+1/2}(i-1/2) \quad (31)$$

Using the same source which is given in Section 3. The results are shown in **Figure 4**, since the breakdown degrees are different at different altitudes, the different breakdown will lead to different plasma concentrations in the mixture-atmosphere, resulting in different degrees of reflection. When the air is breakdown, the electron density $n_e = 10^8 n_{e0}$ [3,11]. So, from (9) the initial electron density is about 4893.2 $m^{-3}$ at 35 km altitude.

As **Figure 4 (a)** shows, the electron density is excited by HPM is about $3.6\times10^{11}$ $m^{-3}$, which has not yet reached the breakdown density. Therefore, there is no breakdown occurred, almost no reflection. From **Figure 4 (b)**, we can see that as the altitude increases the breakdown begin to happen, and the electron density increases sharply, leading to serious reflection. As **Figure 4 (b)** shows, the reflected field actually as high as 43% at the altitude of 38 km, which would undoubtedly harm the high-power emitter device.

Because of different pulse field strength, different pulse width and different frequency correspond to different breakdown threshold, so, the HPM pulses with different parameters at the same altitude will cause different breakdown. Comparing with the **Figure 5 (a)**, **Figure 5 (b)** and **Figure 4 (c)**, we can see that at the same altitude of 40 km, the field strength and pulse width increase would lead to an increase of reflection, but as **Figure 5 (c)** shows, at the same altitude of 40 km the reflection will decrease with the frequency increases. This is because in our concerned altitude range, the breakdown threshold will be decreases with the increases of field intensity and pulse width, but it will increases as the wave frequency increases [13].

## 5. Conclusions

A theoretical physical model describing the propagation of HPM pulse through the mixture-atmosphere is developed in the present work. We treat the mix

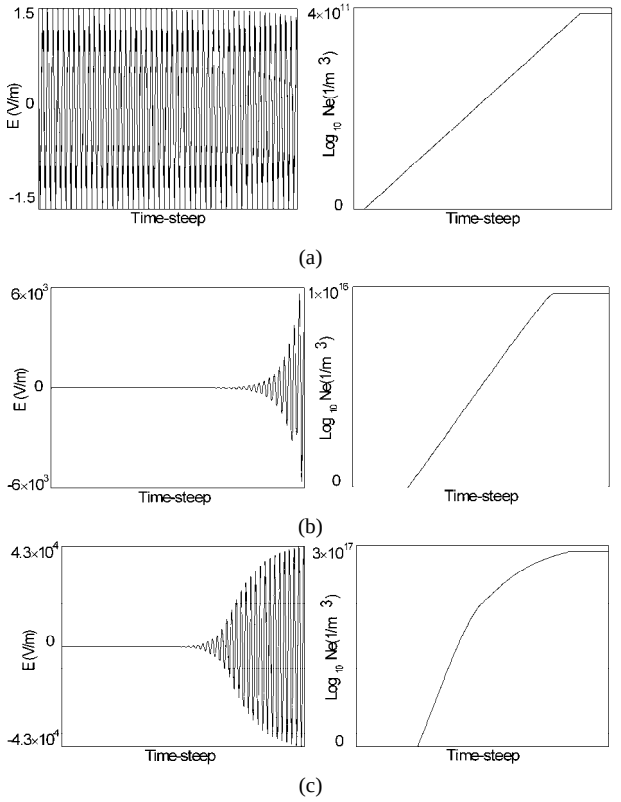


**Figure 4. Reflection at different altitudes. (a) reflection field and electron density at 35 km; (b) reflection field and electron density at 38 km; (c) reflection field and electron density at 40 km.**

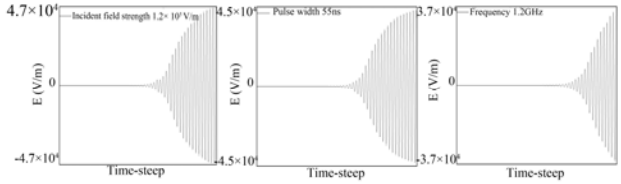


**Figure 5. Reflection intensity of HPM sources with different parameters at 40 km.**

ture-atmosphere generated by HPM air breakdown as a layered inhomogeneous medium. Using the transmission line model of electromagnetic wave propagation in inhomogeneous medium and the FDTD method in inhomogeneous medium, the reflection characteristics of the HPM propagation in the mixture-atmosphere have been studied. The results show that the reflection increases with the degree of air breakdown. The stability conditions for the FDTD difference scheme of the HPM mixture-atmosphere propagation model are firstly presented.

## 6. Acknowledgements

Authors are very grateful to the Natural Science Foundation of China (60771020) for the financial assistance.

 

## REFERENCES

[1] S. P. Kuo, Y. S. Zhang and P. Kossey, "Propagation of High Power Microwave Pulses in Air Breakdown Environment," *Physics Fluids*, Vol. 133, No. 10, 1991, pp. 2906-2912.

[2] W. Woo and J. S. DeGroot, "Microwave Absorption and Plasma Heating Due to Microwave Breakdown in the Atmosphere," *Physics Fluids*, Vol. 27, No. 2, 1984, pp. 475-487.

[3] A. W. Ali, "Nanosecond Air Breakdown Parameters for Electron and Microwave Beam Propagation," *Laser and Particle Beams*, Vol. 6, No. 2, 1988, pp. 105-117.

[4] S. P. Kuo and Y. S. Zhang, "A Theoretical Model for Intense Microwave Pulse Propagation in an Air Breakdown Environment," *Physics Fluids B*, Vol. 3, No. 10, 1991, pp. 2906-2912.

[5] J. H. Yee, R. A. Alvarez, D. J. Mayhall, D. P. Byrne and J. DeGroot, "Theory of Intense Electromagnetic Pulses Propagation through the Atmosphere," *Physics Fluids*, Vol.29, No. 4, 1986, pp. 1238-1244.

[6] J. H. Yee, D. J. Mayhall, G. E. Sieger and R. A. Alvarez, "Propagation of Intense Microwave Pulses in Air and in a Waveguide," *IEEE Transactions Antennas Propagation*, Vol. 39, No. 9, 1991, pp. 1421-1426.

[7] A. Taflove and S. C. Hagness, "Computational Electrodynamics the Finite-Difference Time-Domain Method," 3rd edition, Reading, MA: Artech House, June 2005.

[8] H. S. Chen, Y. Wang and K. S. Chen, "Transient Analysis of Propagation in Non-uniform One Dimensional Media by Transmission Line Method," *Journal of Microwaves*, Vol. 19, No. 3, 2003, pp. 25-29.

[9] J. Y. Wang and C. Y. Jiang, "Refractive Index of Non-Ionized and Ionized Mixture-Atmosphere," *Chinese Journal of Radio Science*, Vol. 20, No. 1, 2005, pp. 34-36.

[10] T. Tang, C. Liao and D. Yang, "Feasibility Study of Solving High-Power Microwave Propagation in the Atmosphere Using FDTD Method," *Chinese Journal of Radio Science*, Vol. 25, No. 1, 2010, pp. 122-126.

[11] D. T. Hou, D. F. Zhou, Z. X. Niu and Z. Q. Yu, "Effect on Air Refraction Index by Effective Electric-Field Intensity in High Power Microwave Propagation," *High Power Laser And Particle Beams*, Vol. 16, No. 9, 2004, pp. 1183 -1185.

[12] C. Zhang, D. F. Zhou, Y. P. Rao, Y. Chen and D. T. Hou, "FDTD Computation of Air Ionization and Breakdown Caused by High Power Microwave," *High Power Laser and Particle Beams*, Vol. 21, No. 5, 2009, pp. 719-723.

[13] M. Löfgren, D. Anderson and M. Lisak and L. Lundgren, "Breakdown-Induced Distortion of High-Power Microwave Pubes in Air," *Physics Fluids B*, Vol. 3, No. 12, 1991, pp. 3528-3531.

[14] M. Thèvenot, J. P. Bérenger, T. Monedière and F. Jecko, "A FDTD Scheme for the Computation of VLF-LF Propagation in the Anisotropic Earth-ionosphere Waveguide," *Annals of Telecommunications*, Vol. 54, No. 5-6, 1999, pp. 297-310.

[15] K. R. Umashanker and A. Taflove, "A Novel Method of Analyzing Electromagnetic Scattering of Complex Objects," *IEEE Transactions Electromagnetic Compatibility*, Vol. EMC-24, No. 4, 1982, pp. 397-405.

 

*J. Electromagnetic Analysis & Applications*, **2010, 2, 549-556**
doi:10.4236/jemaa.2010.29071 Published Online September 2010 (http://www.SciRP.org/journal/jemaa)

# An Approach to a Universal System of Units

**Salama Abdelhady**

Department of Mechanical Engineering, CIC, Cairo, Egypt
Email: salama_hady@cic-cairo.com

Received July 9th, 2010; revised August 15th, 2010; accepted August 15th, 2010

## ABSTRACT

*According to many scientists, there are some redundancies in the SI system of units. Through an entropy approach that depends on a previous analogy between the electrical, mechanical and thermal fields; it was possible to introduce a system of units that removes such redundancies. According to the second law of thermodynamics, the temperature was defined as a quality of heat. Following a proved analogy, the electrical and magnetic potentials may represent also the qualities of electric and magnetic fluxes. According to published experimental results, the electric and the magnetic potentials generates also electromotive forces, EMF, that were measured by Al-Fe thermocouples. The chemical potential or the concentration gradient generates also an EMF, as in the concentration cells, which is measured here by the same Al-Fe thermocouple. Such measurement-results are introduced to define a unique scale for measuring the potentials or qualities of the thermal, chemical, electric, and magnetic fields. The mentioned qualities are not defined by directly measurable quantities, as length and time, but they are found as functions of dimensionless concentrations of mass or energy fluxes. Hence, the volt, as a unit of the introduced EMF scale for potentials measurement, is postulated as a dimensionless unit. Finally, a universal system of units that is based only on three dimensions; L, T, and E, and four fundamental units; meter, second, Joule and volt is introduced in this paper to delete the SI redundancies. The energy replaces the mass as a fundamental unit in the introduced US as it plays a dominant role in most of the scientific and engineering fields. The ampere is not included as a fundamental unit since the charge is considered as a form of energy that is measured in one of the US fundamental units, Joule. The candela and the mole were also not considered as fundamental units as they can be related to the selected fundamental units by appropriate numbers. The limited number of dimensions in the introduced US simplifies the application of the "$\pi$" dimensional theorem to find plausible relations between the main parameters that characterize many physical phenomena and the energy conversions and interactions.*

***Keywords*: *Dimensions, Units, Potentials, Qualities, Thermodynamics, Electromagnetism***

## 1. Introduction

Many scientists have found the international system of units, SI system, as a historical, independent, and redundant system [1-3]. Using the SI system; the dimensional homogeneity is not satisfied in many physical Equations and constants. In **Table 1**, we can find examples of such SI conflicts, which are found in literature [1,2], between the units of analogous quantities in the electric and magnetic fields. The ampere is a unit of the electric current, while "ampere/m" is found as a unit of strength or potential of the magnetic fields. According to Maxwell's wave Equation [4], the unit of the electric field strength, E, should be similar to the unit of the magnetic field strength, H. Both are potentials of the flowing components of the same electromagnetic wave. However, both have conflicting SI units as seen in **Table 1**. Similarly; the conductivity is analogous to permeability while their SI units are confusing as also seen in **Table 1**

The system that will be the center of our concern is shown in **Figure 1**. Such system allows the flow of thermal, electric, magnetic and mechanical energies in addition to mass diffusion to or from the system. According to the second law of thermodynamics; the temperature as a potential of heat flow, is considered as a quality of heat that is defined by hypothetical scales [5]. By analogy [4]; the electric and magnetic potentials are simply postulated as qualities of electric charge and magnetic flux. Such qualities are functions of dimensionless concentrations of charge or energy fluxes similar to the chemical potential that is defined by the dimensionless concentration [6]. So, such potentials may be concluded as dimensionless parameters as they are not defined by directly measurable quantities but they are

 

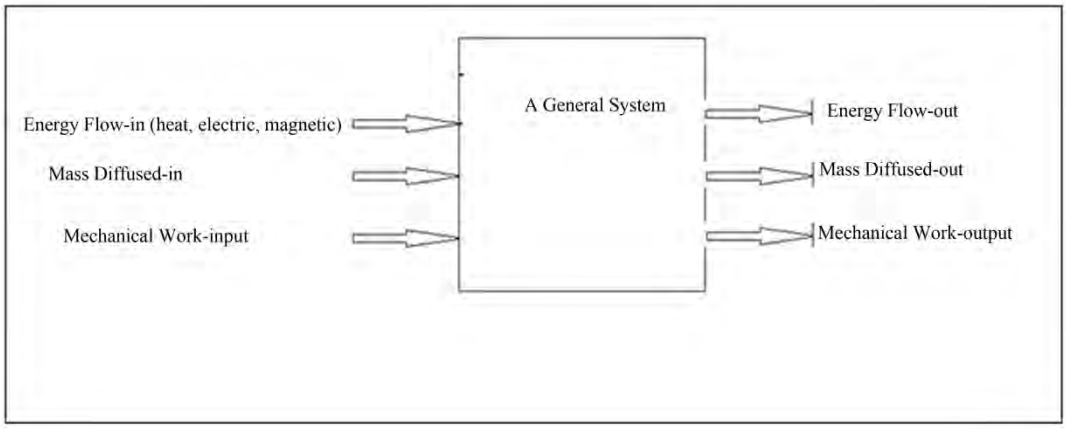


**Figure 1. A general system energy-interactions.**

**Table 1. Electric/Magnetic analogues in SI System.**

| Magnetic quantity | Electric quantity |
|---|---|
| magneto-motive force Amp | electromotive force Volt |
| magnetic field strength Amp/m | electric field strength V/m |
| permeability kg m/sec$^2$/Amp$^2$ | conductivity Sec$^3$Amp$^2$ /kg/m$^3$ |
| magnetic flux m$^2$ kg/sec$^2$/Amp | current Amp |
| magnetic flux density kg/sec$^2$/Amp | current density Amp/m$^2$ |
| reluctance Amp$^2$ / m$^2$ kg / sec$^2$ | resistance m$^2$kg/sec$^3$/Amp$^2$ |

defined by hypothetical scales. The examples of such dimensionless scales are the angular scale that cuts the circular angle into 360 dimensionless degrees and as defining the qualities of a viscous fluid flow by dimensionless Reynolds numbers and of a compressible flow by dimensionless Mach numbers [6]. A common tool for measuring such potentials-scale is suggested by the experimental results discussed by Kumar and others [7] and the measurements elaborated in the presented study. The results compared the performance of an Aluminum-iron thermocouple to other thermocouple combinations. Such Al-Fe thermocouple recorded the generation of excess EMF by influence of magnetic and electric fields. Such influences or effects can be introduced to define a unique scale for evaluating potentials or qualities of the thermal, electric and magnetic fields. However; the concentration gradient or chemical potential generates a similar EMF in volt, as in the concentration cell, which is measured in the present study by the use of the same Al-Fe thermocouple. So, the volt will be introduced in the presented approach as a dimensionless fundamental-unit for the measurement of the thermal, chemical, electric and magnetic potentials.

As energy is the core of most scientific and engineering fields; the Joule is considered in the introduced US as a fundamental unit while the unit of mass, kg, is considered as a derived unit. Such selection solves many conflicts found in dealing with properties of vacuum where the mass, involved in the SI system, is meaningless in vacuum. Finally, the introduced universal system is based on four units; meter, second, Joule and volt and three dimensions; Length, Time and Energy. Such system leads to removing the SI redundancies in scientific relations, constants and many physical quantities [2,3]. However, the candela was not considered as a fundamental unit in the introduced approach as such unit is actually defined in terms of the energy intensity of a specified spectrum of energy-radiation; *i.e.* in Joule. Similarly; the mole was not considered as a fundamental unit as it can be replaced by an appropriate number of molecules, $6.02 \times 10^{23}$ molecules per mole, which corresponds to a specific mass in kg for each material.

The introduced three dimensional system of units leads also to simple representation of the physical quantities in a three dimensional space, L, T and E. Such system simplifies application of the $\pi$ theorem to find dimensionally homogenous relations between the parameters that characterize different phenomena and to define different energy interactions.

## 2. A Universal Thermocouple

During their experimental work to compare the performance of some common thermocouples; Kumar and others [7] found better performances of an Aluminum-Iron thermocouple as compared to other combinations. Aluminum fulfills the requirement of high electrical conductivity while iron is a ferromagnetic material that has a comparatively low thermal conductivity.

**Figure 2** shows the variation of the generated EMF due to variable temperature differences by various thermocouples where an EMF of "1.6892" mV was measured at temperature difference of 293˚C when using an Al-Fe thermocouple. However, they also recorded effects of magnetic flux on the performance of such Al-Fe ther

 

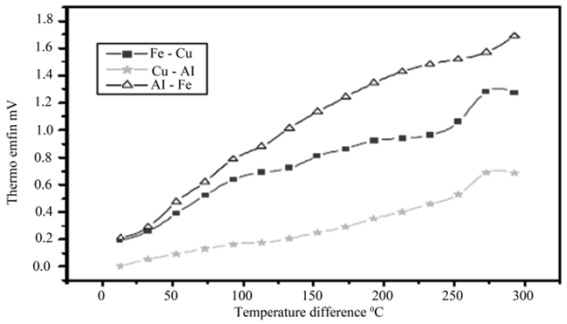


**Figure 2**. **Performance of different thermocouples [7].**

mocouple as seen in **Figure 3**. When a magnetic field of certain magnetic flux intensity was applied on such thermocouple at parallel orientation of the thermocouple, the generated EMF increased to 1.898 mV at the same temperature difference of 293˚C.

By application of an electric field of potential 4 V on such thermocouple at parallel and perpendicular orientation, significant effects on the generated EMF were found according to the results shown in **Figure 4**.

Such generated EMF by an Al-Fe thermocouple due to application of different fields introduces one unit and a unique instrumentation for measurement of the thermal, electric and magnetic potentials. A voltmeter of a proper scale for each field can be applied to measure directly the potentials of such fields by one unit; Volt. However, such scales may be calculated, as an example, from the found measurement results of Kumar where 1.6983 mV mainly corresponded to 566 K and 0.423 mV corresponded to 300 K. The measured EMF which is generated due to applying a magnetic flux of 120 G was found as (1.898 – 1.698 =) 0.2 mV. Similarly; the EMF found due to applying an electric potential of 4 V was found to be (1.2 – 0.4 =) 1.2 mV.

According to these results; the magnetic and electric fields have specific effects on the involved thermocouple and generate EMF as the EMF generated by the effect of temperature differences. Such results introduce also other

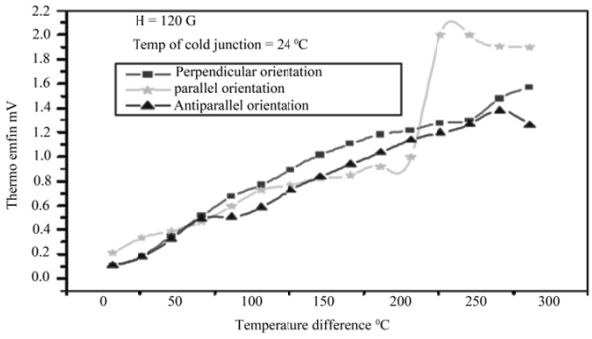


**Figure 3. Influence of magnetic field on performance of Al-Fe thermocouple [7].**

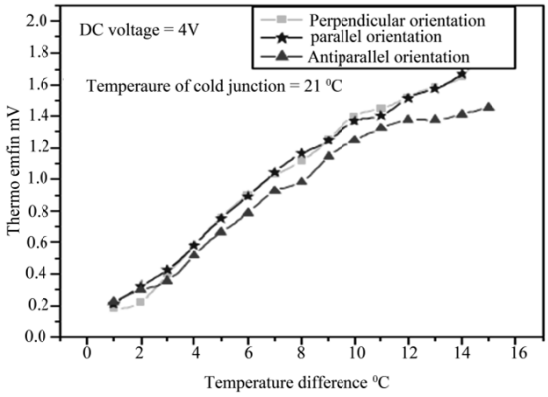


**Figure 4. Influence of electric field on performance of Al-Fe thermocouple [7].**

newly discovered effects on thermocouples which are similar to the Seebeck effect [5]. Such measured effects of the magnetic and electric fields are sustaining the postulated definitions of magnetic flux and electric char-ges as modified forms of energies or electromagnetic waves that possess specific potentials as the potential possessed by heat [4].

According to literature of physical chemistry [6], the chemical potential or the concentration gradient generates also an electrical potential that can be measured in volt. Such potential have been measured experimentally in this study by using the same Al-Fe thermocouple. The cold junction of the Al-Fe thermocouple was inserted into a water solution of high concentration while the hot junction was inserted into water solutions of less concentration. The difference in concentration generates excess EMF that is measured in volt as seen in **Figure 5**. So, we may postulate a universal system of units that considers the volt as a unit of the thermal, chemical, electrical, and magnetic potentials.

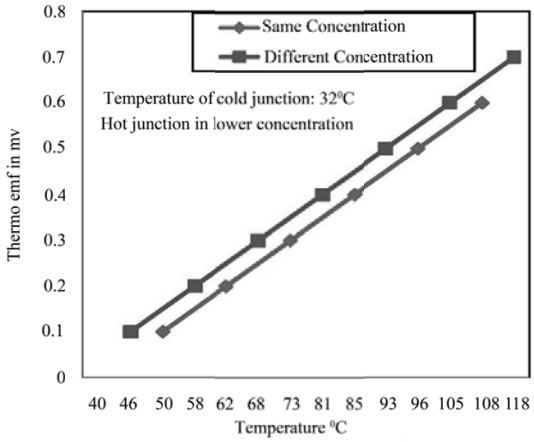


**Figure 5. Influence of chemical concentration on performance of Al-Fe thermocouple.**

 

## 3. Analogy of Thermal, Electric and Magnetic Fields

The Fourier Law of thermal conduction is stated as follows [8]:

$$q = -k\nabla T \quad (1)$$

Where $\boldsymbol{q}$ is the heat flux density in W / m$^2$. $\boldsymbol{T}$ is the temperature in, as postulated, in volt and is $\boldsymbol{k}$ the thermal conductivity of materials in W/m$^2$ V.

Similarly; Ohms Law of Electric conduction is stated as follows [8, 9]:

$$J = -\sigma\nabla\varphi_e \quad (2)$$

Where $\boldsymbol{J}$ is the electric flux density in W/m$^2$. $\boldsymbol{\varphi_e}$ is the electrical potential in Volts and $\boldsymbol{\sigma}$ is electrical resistance in W/m$^2$ V or Ohm.

The commonly used form for the relationship between the magnetic field parameters $\boldsymbol{B}$ and $\boldsymbol{H}$ is [9]:

$$B = -\mu_m H \quad (3)$$

$\boldsymbol{B}$ is sometimes called the magnetic flux density or the magnetic induction. The unit of an energy- flux density is measured generally in W/m$^2$. Hence, the unit of $\boldsymbol{B}$ should be analogous to the units of the thermal and electrical fluxes in W/m$^2$. $\boldsymbol{\mu_m}$ is the magnetic permeability of a material that is analogous to the thermal and electrical conductivities. By analogy between the electric, magnetic and thermal field [4], Equation (3) that describes the magnetic flux can be expressed by an Equation similar to Equations (1) and (2) of the form [8,9]:

$$B = -\mu_m\nabla\varphi_m \quad (4)$$

Comparing Equations (3) and (4), the magnetic potential $\boldsymbol{\varphi_m}$ can be defined in terms of the magnetic field intensity by the following relation:

$$H = -\nabla\varphi_m \quad (5)$$

According to Equations (1), (2) and (4); the heat, electric and magnetic fluxes are denoted by $\boldsymbol{q}$, $\boldsymbol{J}$ and $\boldsymbol{B}$ and they are measured in W/m$^2$. Similarly, the thermal, electric and magnetic potentials are denoted by $\boldsymbol{T}$, $\boldsymbol{\varphi_e}$ and $\boldsymbol{\varphi_m}$ and they are measured, as postulated, in Volts. Finally, the unit of conductivities $\boldsymbol{k}$, $\boldsymbol{\sigma}$ and $\boldsymbol{\mu_m}$ will result, according to the stated Equations, in W/m$^2$ V. Such modified units of the fluxes and potentials may be considered as results of the definition of the electric charge and the magnetic flux as forms of electromagnetic waves [4].

## 4. An Entropy Approach to a Universal System of Units

In a recently published paper [4], it was introduced a new thermodynamic fundamental Equation of the following (rather modified) form:

$$dU + p\,dV = T\,dS_t + \varphi_e dS_e + \varphi_m dS_m + \sum\mu_i dN_i \quad (6)$$

Equation (6) represents the electric charge, Q in terms of the electric potential, $\boldsymbol{\varphi_e}$, times a change of entropy $\boldsymbol{dS_e}$ and the magnetic flux as magnetic potential, $\boldsymbol{\varphi_m}$ , times a change in entropy $\boldsymbol{dS_m}$. Such approach depends on the analogy between the thermal, electric and magnetic fields [4] where heat is expressed in terms of temperature (as the thermal potential or quality), $\boldsymbol{T}$, times a change in entropy $\boldsymbol{dS_t}$. In Equation (6), the product of the two terms $\boldsymbol{\mu_i}$ and $\boldsymbol{dn_i}$ is expressing the chemical energy where μ is the chemical energy added to the system per unit increase in the concentration of certain chemical specie by $\boldsymbol{dN_i}$. The term $\boldsymbol{dN_i}$ represents the change of relative concentration of a specie "$\boldsymbol{i}$" by the amount $\boldsymbol{dn_i/n_i}$ where $\boldsymbol{n_i}$ is the total number of moles of such specie. As we can discover; the definition of $\boldsymbol{\mu_i}$ as a chemical potential is misleading since it represents the added chemical energy per unit increase in concentration and its driving potential is the concentration of each of the chemical species. In other words, we may consider $\boldsymbol{\mu_i}$ as the entropy increase of the system per unit increase of the relative concentration of the species.

Introducing the definition of the free Gibbs energy:

$$G = U + pV - TS \quad (7)$$

In this Equation; we may consider the potential $\boldsymbol{T}$ as the sum of the driving potentials of the thermal, electric and magnetic energies.

Taking total differential of $\boldsymbol{G}$, we have:

$$dG = dU + pdV + Vdp - TdS - SdT \quad (8)$$

Replacing $\boldsymbol{dU}$ in Equation (8) from the fundamental Equation (6); we get:

$$dG = TdS - pdV + \sum_i \mu_i dN_i + pdV + Vdp - TdS - SdT \text{ , or}$$

$$dG = Vdp - SdT + \sum_i \mu_i dN_i \quad (9)$$

Dealing with systems that involve the transfer of different forms of energy as in thermal, electric, magnetic, and chemical energies, Equation (9) can be rewritten as follows:

$$dG = Vdp - S(dT + d\varphi_e + d\varphi_m) + \sum_i \mu_i dN_i \quad (10)$$

The potentials; $\boldsymbol{T}$, $\boldsymbol{\varphi_e}$ and $\boldsymbol{\varphi_m}$ will be substituted, as previously discussed, in volts and $\boldsymbol{S}$ in Joule/ volt. By comparing the terms of Equation (10); the terms S and $\boldsymbol{\mu_i}$ may be considered as the entropy added to the system due to the increase of any of the potentials: $\boldsymbol{T}$, $\boldsymbol{\varphi_e}$, $\boldsymbol{\varphi_m}$ and $\boldsymbol{dn_i/n_i}$. So, the entropy may be considered in general as a specific free energy per unit potential, *i.e.* it defines the free energy required to increase the potential of a system by one volt.

According to the second law of thermodynamics, temperature is considered as a quality of heat [5]. By analogy [4]; the electric and magnetic potentials are considered also as qualities of electric charge and magnetic

 

flux. Such qualities represent, according to Equation (10), the motivating mechanism that releases the entropy from the system into various energy forms. As the chemical potential is determined by the dimensionless concentration gradient of different species [6], different literatures consider also, by analogy, the thermal, electric and magnetic potentials are functions of the concentration of the related fluxes [9-12]. Accordingly, such potentials will be considered dimensionless parameters as they are functions of dimensionless concentrations. This may originate also from the definition of temperature, the quality of heat, by a hypothetical scale similar to a scale that partitions the circle into 360 dimensionless degrees [8].

## 5. A Three-Dimensional System of Units

Many references [1-3,10-12] found it is undesirable to use SI system of units in the thermo-chemical and electromagnetic fields as it fails to express properly the dimensional homogeneity of the characterizing Equations in such fields. Table 1 shows examples of such redundancies. In addition; the SI system does not find a physical significance of many constants or identical units of the quantities E, D, B, H and μ [9,11,12].

A recently defined system of units that was introduced to modify the SI system depends only on Space and Time, S and T, as basic dimensions and fundamental units [2]. However, such ST system of units did not solve the redundancy that was discussed. Rather, it added many conflicts in its introduced units. As an example, it defines the energy and temperature by the same dimensions $T\,S^{-1}$ while energy is physically different than temperature. Similarly, such ST system assigns to the electric charge and the space the same dimension S which contradicts their definitions and physical meanings.

The introduced US of units is relied upon the previously discussed analogy between the thermal, electrical, magnetic and chemical energies. According to Equation (10), the heat, electrical and magnetic fluxes are considered as forms of energy or electromagnetic waves that are measured by the energy dimensions and units. According to the studied measurement-results of the Al-Fe thermocouple, the potentials of these fluxes are defined by a unique scale, the measured EMF, and one dimensionless unit, the volt.

In many scientific and engineering studies, energy plays a dominant role. So, the proposed system of units introduces energy, E, as one of its fundamental dimensions and units. Units of time and space, of the dimensions T and L, are considered also as fundamental units. So, the introduced system is based on three basic dimensions and units: the length in meters, time in seconds, and energy in Joule. The volt is considered as a dimensionless unit that measures, as previously explained, the potentials of the electric, magnetic and thermal fields by a unique EMF scale. The introduced US of units excludes the ampere as a fundamental unit where the charge, as modified electromagnetic waves [4], is measured directly by Joule. The candela is defined as the luminous energy intensity, in a given direction, of a source that emits monochromatic radiation of frequency $540 \times 10^{12}$ hertz and that has a radiant intensity in that direction of 1/683 watt per steradian [8]. Therefore, the candela is defined in terms of energy units and can be skipped as a fundamental unit [8].

Other physical quantities can be derived in terms of the introduced US fundamental dimensions and units according to their physical definitions. Some examples of derived US units are introduced as follows:

Velocity

$$v = \frac{\partial x}{\partial t}\, m/s \qquad of \quad dimensions LT^{-1} \tag{11}$$

Acceleration

$$a = \frac{\partial_2 x}{\partial t^2} = \frac{\partial v}{\partial t} \quad m/s^2 \quad of \quad dimensions LT^{-2} \tag{12}$$

Mass

From relativity theory:

$$m = \frac{E}{c^2} \quad kg \quad of\ dimensions EL^{-2}T^2 \tag{13}$$

Power

$$\dot{E} = P = \frac{\partial E}{\partial t}\, Joul/s \ or\ W\left(Watt\right)\ of\ dimensions ET^{-1} \tag{14}$$

Such Power dimensions and units represent also the rate of flow of heat, electric charge and magnetic flux as $\dot{\boldsymbol{Q}}_{\boldsymbol{th}}$, $\boldsymbol{i}$ and $\boldsymbol{B}$.

Energy flux

$$\dot{e} = \frac{\dot{E}}{A} \quad W/m^2 \quad of \quad dimensions EL^{-2}T^{-1} \tag{15}$$

Such energy flux represents rate of energy flow per unit area as $\dot{\boldsymbol{q}}$, $\dot{\boldsymbol{j}}$ and $\dot{\boldsymbol{b}}$:

Force

$$F = \frac{\partial E}{\partial x}\, Joul/m \quad or \quad N\left(Newton\right) of\ dimensions EL^{-1} \tag{16}$$

Pressure

$$p = \frac{F}{A}\, N/m^2 \ or\ Pa\left(Pascal\right) of\ dimensions EL^{-3} \tag{17}$$

Potential gradient: $\nabla\boldsymbol{\varphi}$ (as temperature gradient, electric field gradient or magnetic field gradient):

$$\nabla T, \nabla E, \nabla H = \frac{\partial \varphi}{\partial x}\, Volt/m\ of \quad dimension L^{-1} \tag{18}$$

Conductivity (as thermal, electric and magnetic conductivity):

 

$$\sigma,\lambda = \frac{energy\ \ flux}{potential\ \ gradient} = \frac{\dot{e}}{\frac{\partial \varphi}{\partial x}}\ W/mV$$

$$of dimensions ET^{-1}L^{-1} \quad (19)$$

Permeability

$$\mu = \frac{energy\ \ flux}{magneti\ cintensity\ gradient} = \frac{B}{\nabla \varphi}\ Henry/m\ or\ W/mV \quad (20)$$

$$of\ \ dimensions\ ET^{-1}L^{-1}$$

Permittivity:

$$\varepsilon_0 = \frac{electric\ \ flux\ density}{electric\ \ field\ strength} = \frac{D}{E}\ Joul/mV \quad (21)$$

$$of\ \ dimensions EL^{-1}$$

Resistivity:

$$\rho = \frac{1}{\sigma} V.m/W\ \ of\ \ dimensions E^{-1}TL \quad (22)$$

Resistance (reluctance):

$$R_{th,el,mag} = \frac{\rho L}{A} = \frac{L}{\sigma A} = \frac{L}{\mu A}\Omega\ or\ V/W\ \ of\ \ dimensions E^{-1}T \quad (23)$$

Coil Inductance

$$L = \frac{e.m.f}{\partial i/\partial t}\ Vs/W\ \ of\ \ dimensions E^{-1}T^2 \quad (24)$$

Capacitance (Electric and thermal)

$$C = \frac{energy\ stored}{potential\ difference} = \frac{Q}{\Delta \varphi} Farad \quad (25)$$

$$or\ \ Joul/Volt\ \ of\ \ dimension E$$

According to the limited number of dimensions of the introduced system, 3 dimensions, it is possible to represent the above mentioned derived units into a three- dimensional space which is shown **Figure 6**. Such representation simplifies the dimensional comparison between different physical quantities and shows directly the analogy between different fields.

## 6. Discussion of the Introduced US of Units

The introduced US of units assigns unique dimensions for the analogous parameters in the electric and magnetic fields as the energy flux, resistance, conductivities, and resistivity as seen in **Table 2** and **Figure 5**. The conflicts of the SI system of units, discussed in **Table 1**, are completely deleted as shown **Table 2**. People with knowledge of the B-field and H-field have argued, as Larson [11], that the SI system is in a mess because physics of such parameters is in a mess. They said that ascribing SI units to the permeability μ is not science but computational legerdemain. The introduced US of units express the permeability and the permittivity by units that are

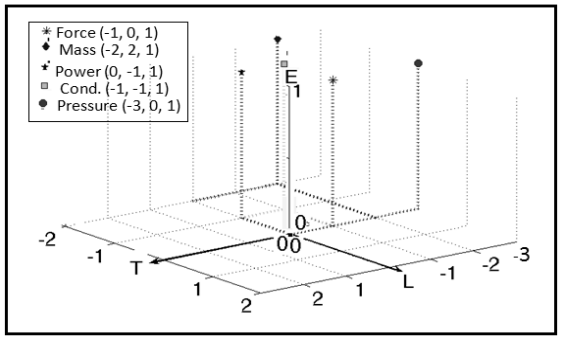


**Figure 6. The postulated "TLE" dimensional system.**

**Table 2. Electric/Magnetic Fields analog in the US system**.

| Magnetic quantity | Electric quantity |
|---|---|
| magneto-motive force Volt | electromotive force Volt |
| magnetic field strength Volt/m | electric field strength V/m |
| permeability W/m V | conductivity W/m V |
| magnetic flux W | current W |
| magnetic flux density W/m$^2$ | current density W/m$^2$ |
| reluctance V/W or Ω | resistance V/W or Ω |

analogous to the units of electrical or thermal conductivity. Similarly, the introduced system solves the conflicts of the SI system that measures the free space or vacuum permeability and permittivity by units that involve the mass while mass has no meaning in vacuum. Similarly; vacuum has an impedance SI units of "m$^2$kg/sec$^3$/Amp$^2$". Such impedance involves the mass in vacuum as one of its units while the mass does not exist in vacuum. As the US excludes the mass as a fundamental unit, it excludes also assigning the mass to vacuum as the unit of such impedance is Volt/watt.

We may look also at the units of the force between two electric charges, Coulomb's force:

$$F = \frac{Q_1 Q_2}{4\pi\varepsilon_0 r^2} \quad (26)$$

Substituting the introduced dimensions of the charge Q in (E) and of the permittivity $\boldsymbol{\varepsilon_0}$ in (E L$^{-1}$); the force will result directly in force dimensions and units, Newton. Such unit is already derived in Equation (16) as a unit of

force in the introduced US of units. Looking at the definition of the fine structure constant; it is found as follows [14]:

$$\alpha = \frac{e^2}{4\pi\varepsilon_0 c\bar{h}} \quad (27)$$

According to the introduced system: $\boldsymbol{e}$ is the elementary charge in J, $\bar{h}$ is the reduced Planck constant in J.s, $\boldsymbol{\varepsilon_0}$ is the permittivity in J/m V and c is the speed of light in m/s. Substituting such units; it also leads to a dimen-

 

sionless parameter in accordance to its definition.

According to the SI system of units, the electron-volt is a unit of energy equal to approximately $1.602 \times 10^{-19}$ J and is described also as a charge of $1.602 \times 10^{-19}$ [14,15]. By classical definition, it is equal to the amount of kinetic energy gained by a single unbound electron when it accelerates through an electric potential difference of one volt. So, it is not known if it is kinetic energy of $1.602 \times 10^{-19}$ J or as described a charge of the same figure of quantity of $1.602 \times 10^{-19}$ C. Such redundancy of the SI system that cannot find the plausible explanation of the equality of such figures of the electron's charge in Coulomb and its kinetic energy in Joule is solved. In the US of units, we consider, as postulated here, the electric charge has the same unit as energy in Joule. In this case the e. V will be defined as the specific charge of the electron or the amount of energy that increases the potential of the electron by 1 volt in analogy to the defined specific heat of a body as the amount of heat that increases the temperature of such body by one degree.

The limited number of dimensions in the introduced system simplifies the application of the $\boldsymbol{\pi}$ dimensional theorem to express the relation between different physical quantities. As an example; the dimensionless- structure constant can be found in terms of the permeability, the frequency of the electron charge and the related parameters as follows [16]:

$$\alpha = \frac{e^2 . \nu_{electron}}{4\pi\mu_0 c\overline{h}} \tag{28}$$

Equating the left sides of Equations (27) & (28) gives an interesting result:

$$\nu_{electron} = \frac{\mu_0}{\varepsilon_0} \tag{29}$$

As the electron charge is considered, according to the postulated definition [4], a modified electromagnetic wave, it is possible to find the wavelength of an electric charge according to the relation:

$$\lambda_{electron} = c_o \nu_{electron} = c_0 * \frac{\mu_0}{\varepsilon_0} \tag{30}$$

Such frequency assures the postulated definition of the charge as an electromagnetic wave of specified frequency [4] which is referred as Bohr's electron frequency [16].

Applying the π dimensional theorem once more to find an expression for the magnetic attraction force between two parallel conductors of equal length $\boldsymbol{L}$ and carrying electric currents $\boldsymbol{I_1}$ and $\boldsymbol{I_2}$ in terms of the permeability of the surrounding medium (vacuum), speed of electromagnetic waves (or of electric charge) and the spacing between the conductors "$\boldsymbol{d}$"; it can be found as:

$$f = \frac{F}{L} = \frac{I_1 I_2}{2\pi d L c_0 \mu_0} \tag{31}$$

Equation (31) expresses the force is in Newton the force/unit length in N/m; *i.e.* in accordance to the US derived units.

To remove the mess between the $\boldsymbol{B}$ field and $\boldsymbol{H}$ field [11], the first law of thermodynamics, as a law of conservation of energy, is applied to the case of an electric motor shown in **Figure 6**. A power source of potential "V" is feeding the motor's windings, which are connected in parallel, by a total current I as shown in **Figure 6.**

According to experimental data [16], the magnetic field intensity "$\boldsymbol{H}$" is found, with sufficient accuracy, proportional to the potential of the feeding current "$\boldsymbol{V}$". According to this result, it is possible to prove with sufficient accuracy also that the voltage drop across the armature is equal to the intensity of the magnetic field strength of the shunt coil as both are connected in parallel, according to **Figure 6**, and both are measured by the same unit, according to the introduced US of units. So;

$$H \equiv V \tag{32}$$

Accordingly; the input power to such motor can be determined by the following power relation [8]:

$$Input\ Power = V * I \tag{33}$$

$\boldsymbol{I}$ is the sum of currents flowing through the magnet and armature windings. $\boldsymbol{V}$ is the same potential difference across the magnet and coil windings, **Figure 7**. The output work of such motor is [8]: $\boldsymbol{F} * \boldsymbol{v}$ or $\boldsymbol{\tau} * \boldsymbol{\omega}$; where $\boldsymbol{F}$ is the force acting on the armature-coil and ν is its velocity, $\boldsymbol{\tau}$ is the torque acting on the armature-coil and $\boldsymbol{\omega}$ is its angular velocity. The efficiency of this process can be written as follows:

$$\eta = \frac{output}{input} = \frac{F * v}{V * I} = \frac{\tau * \omega}{V * I} \tag{34}$$

Substituting Equation (32) into Equation (33); it is possible to express the input power by a rather new relation:

$$Input\ Power = H * I \tag{35}$$

Such relation expresses directly the interactions between the intensity of the magnetic field $\boldsymbol{H}$, that depends on the electrical field potential, $\boldsymbol{V}$, and the flowing cur

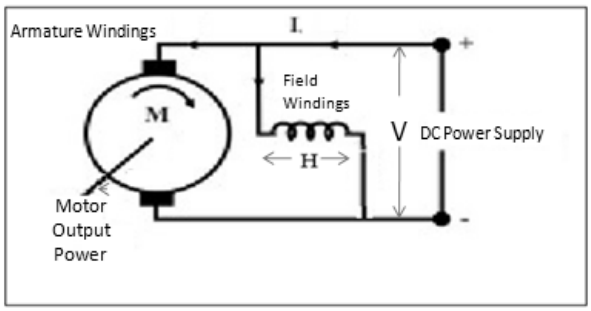


**Figure 7. Armature and Field windings in parallel [8].**

 

rent in the motor windings, ***I***. The main effect of the field current is the generation of magnetic field of potential "***H***" through the magnetic core. Such core does not allow any current to flow but only magnetic flux. Equation (35) may be valid for measuring the power input to motors in general where it expresses interactions between electric and magnetic fields. Substituting Equation (35) into Equation (32), we can define the efficiency of the electric motor by a new relation:

$$\eta = \frac{output}{input} = \frac{F * v}{H * I} = \frac{\tau * \omega}{H * I} \qquad (36)$$

Hence, the force acting on a carrying current- conductor that moves in a magnetic field or the torque acting on such conductors can be expressed by dimensionally correct Equations in the US of units of the following form:

$$F = \eta * \frac{H * I}{v} \qquad \text{N.} \qquad (37)$$

$$\tau = \eta * \frac{H * I}{\omega} \qquad \text{N. m} \qquad (38)$$

Such Equation can be generally validated for motors or generators.

## 7. Conclusions

This study introduces a system of units that removes the redundancies found in the SI system of units. Such system is called "Universal System" as it can be applied universally to all scientific fields. The introduced system depends on an entropy approach that used analogy between different forms of energy-system interactions and on a unique dimensionless scale that define all energy-potentials. The introduced US of units is defined by four fundamental units and three dimensions. The limited number of dimensions in the introduced system simplifies the application of the π dimensional theorem to reformulate the relations between the physical parameters on dimensional basics. It offers also a plausible definition of the electron-volt as a unit for energy or charge. It helps also in expressing electromagnetic relations by dimensionally homogenous relations.

## REFERENCES

[1] M. Abubakr, "On Dimensional Analysis, Redundancy in set of fundamental quantities and Proposal of a New Set," *General Physics*, 2007. http://arxiv.org/abs/0710.3483v1

[2] X. Borg, "Unified Theory Foundations-The ST System of Units," *Blaze Labs Research*, 2005. http://www.blazelabs.com/f-u-suconv.asp

[3] S. Abdelhady, "A Three Dimensional System of Units," *Proceedings of the 14th International Conference on Applied Mechanics and Mechanical Engineering*, MTC, Cairo, May 2010, paper MD-4.

[4] S. Abdelhady, "A Fundamental Equation of Thermodynamics that Embraces Electrical and Magnetic Potentials," *Journal of Electromagnetic Analysis & Applications*, Vol. 2, No. 3, 2010, pp. 162-168.

[5] A. C. Yunus and A. B. Michael, "Thermodynamics: An Engineering Approach," McGraw-Hill Science Engineering, 2006.

[6] P. W. Atkins and J. DePaula, "Physical Chemistry," 8th Edition, Oxford University Press, W.H. Freeman & Co., 2006.

[7] V. Kumar, J. Singh and S. S. Verma, "Performance Comparison of Some Common Thermocouples for Waste Heat Utilization," *Asian Journal of Chemistry*, Vol. 21, No. 10, 2009, pp. 62-65.

[8] J. Jewett and R. A. Serway, "Physics for Scientists and Engineers with Modern Physics," 7th Edition, Thomson, Brooks/Cole, 2008.

[9] G. D. Yarnold, "Notes on Electric and Magnetic Dimensions," *Proceedings of the Physical Society*, iopscience. iop.org, 1942, pp. 189-193.

[10] S. W. Hawking and G. F. R. Ellis, "The Large Scale Structure of Space-Time," Cambridge University, 1973.

[11] R. Clarke, "Unit System in Electromagnetism," 2009. http://info.ee.surrey.ac.uk/Workshop/advice/coils/unit_systems/index.html

[12] G. M. Trunov, "Correctness of the International System of Units in the Area of Electromagnetism," J*ournal of Measurement Techniques*, Vol. 26, No. 1, 1983, pp. 9-10.

[13] A. J. Hewitt, A. Ahfock and S. A. Suslov, "Magnetic Flux Density Distribution in Axial Flux Machine Cores," Electric Power Applications, IEE Proceedings, 2005, Vol. 152, pp. 292-296.

[14] F. Stevens and F. Charles, "The Six Core Theories of Modern Physics", MIT Press. ISBN 0-262-69188-4, 1965.

[15] J. L. Flowers, N. J. Cleaton, P. W. Josephs and B. W. Betlev, "Progress toward a Precision Measurement of the Helion Magnetic moment in Bohr Magnetons," Instrumentation and Measurement, IEEE Transactions, Vol. 48, 1999, pp. 209-211.

[16] R. G. Bartheld and J. A. Kline, "Comparative Efficiency Measurements," IEEE Proceedings, Vol. 38, No. 2, 1997, pp. 608-614.

 

*J. Electromagnetic Analysis & Applications*, 2010, 2, 557-562
doi:10.4236/jemaa.2010.29072 Published Online September 2010 (http://www.SciRP.org/journal/jemaa)

# Analysis of the Focusing Characteristics of Double Negative Binary Diffractive Lens

**Zongxin Wang[1], Lizhi You[2]**

[1]State Key Lab of Millimeter Waves Southeast University, Nanjing, China; [2]Radar and Avionics Institute of AVIC, Wuxi, China
Email: wangzx@seu.edu.cn

Received May 29th, 2010; revised July 26th, 2010; accepted August 5th, 2010

## ABSTRACT

*For a compact millimeter wave imaging system it is very important to design every component into small size, for the components in a millimeter wave system are usually much larger than those in an optical imaging system due to relatively long wave lengths. In this paper, we suggest a kind of binary diffractive lens* (*BDL*) *designed using double negative materials* (*DNG*) *as the objective lens for a millimeter wave imaging system. The DNG-BDL has not only the advantage of low profile but also small f number, which will be benefit for constructing a compact millimeter wave imaging system. Several DNG-BDL are designed and analyzed using the FDTD method. The numerical results of the focal plane field of the DNG-BDL are presented, which show that the DNG-BDL with small f number has relatively better focusing characteristic than that of a double positive BDL with same f number.*

***Keywords*: *Millimeter Wave Imaging, Binary Diffractive Lens, Double Negative Material***

## 1. Introduction

Since Veselago's theory [1] about a homogeneous isotropic electromagnetic material in which both permittivity and permeability have negative real values ($\mu < 0$, $\varepsilon < 0$) over thirty year's ago, the properties of the double negative materials (DNG) have raised a great deal of interest, many interesting phenomena and applications of the DNG have been found, such as Plano-concave DNG lens [2], negative angles of refraction [3,4], enhanced focusing [4,5], backward wave antennas [6], and electrically small antennas[7]. In this paper, DNG was used to design binary diffractive lens (BDL) [8,9], whose potential application is the objective lens in a millimeter wave (MMW) imaging system. In MMW imaging, sizes of the components are usually much larger than those in an optical imaging system due to relatively long wave lengths, so reducing the component's sizes is very important for designing a compact MMW imaging system. The BDL has advantages of light weight and low profile [10,11] than ordinary curve face lens, which will accordingly benefit for building up compact imaging system. Besides the aforementioned advantages of an traditional BDL made of double positive medium (DPS), the DNG-BDL with small *f* number (FN) is expected to have better focusing characteristics than a DPS one, which is well-founded for as we know that Plano-concave DNG lens show good small FN [2] characteristics, and the small FN characteristic of lens is also very important for constructing a compact imaging system especially at MMW frequencies. So in this paper, we present the design formulas of the DNG-BDL; several DNG-BDL are designed at frequency of 94GHz and analyzed using FDTD method which is powerful for analyzing DNG problems [12,13]; the focal plane fields of the DNG-BDL are presented to show the focusing characteristics of the DNG-BDL with small *f* number.

*This Paper is supported by NSFC, Project Number: 60970058

## 2. Design of the DNG-BDL

The basic characteristic of an imaging lens is that it can focus the plane wave to a focal point. In practice, imaging lens can not focus plane wave absolutely to a point, it can only focus the plane wave to a small region, and this will be represented by a main narrow lobe in the focal plane field (FPF) intensity distribution which is drawn versus a line perpendicular to the propagation direction, see **Figure 1**, there may be small side lobes which will degrade the imaging quality. The field distribution at the focal plane is actually the field sum of the electromag-

 

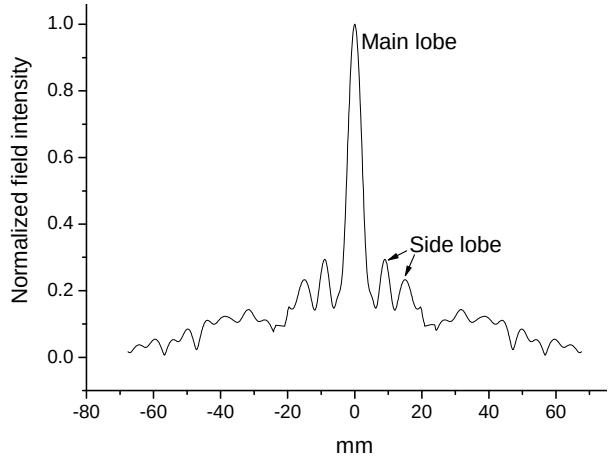


**Figure 1. Focal field distribution for a typical imaging lens incident by plane wave.**

netic waves passing through a lens, and the reason why energies concentrate into the main beam is that the phases of the electromagnetic waves reaching to the focal point have nearly same phases. So the basic rule for design a focusing lens is that every wave path to the focal point should be equal, for example the wave path ABCO in **Figure 2** should equal to wave path DEFO.

Following the design rule just mentioned, take a $1/2^2$ BDL ($2^2$ sub-zones in each zone) as an example [14], the distance from the focal point to the lens are

$$r_n = f + n\frac{\lambda}{2^2} \qquad n = 1, 2, 3\cdots \tag{1}$$

where

$r_n$ is the distance from the focal point to the lens , $n$ is the number index of the sub-zones, $f$ is the focal length, $\lambda$ is the wavelength. It is clear that there is $\lambda/2^2$ difference (phase difference is $\pi/2$) between two neighboring $r_n$.

Waves propagated in DNG medium generate negative wave path differences compared to waves propagated in the air, which is opposite to that in DPS medium. Different height of sub-zones will generate wave path difference and this will compensate for the difference among all $r_n$, then each wave path to the focal point will be equal. Accordingly, the sub-zone step height d is determined by the following equation

$$k_d d - k_0 d = -\pi/2 \tag{2}$$

where

$k_d$ is the wave number in the DNG medium and according to [12], $k_d = -\sqrt{\mu_r \varepsilon_r}$ when $\mu_r$ and $\varepsilon_r$ are both negative, so from equation (2) we get

$$-\frac{2\pi}{\lambda}\sqrt{\mu_r \varepsilon_r}\, d - \frac{2\pi}{\lambda} d = -\pi/2,$$

$$i.e.\quad d = \frac{\lambda}{2^2}\frac{1}{\sqrt{\mu_r \varepsilon_r}+1} \qquad (\mu_r < 0, \varepsilon_r < 0) \tag{3}$$

For $1/2^k$ BDL, there are $2^k$ sub-zones in each zone, and the path difference between two neighboring sub-zones is $\lambda/2^k$, then the parameters of this BDL are:

$$r_n = f + n\frac{\lambda}{2^k} \tag{4}$$

$$\rho_n = \left[ nf\frac{\lambda}{2^{k-1}} + \left(n\frac{\lambda}{2^k}\right)^2 \right]^{1/2} \tag{5}$$

$$d = \frac{\lambda}{2^k}\frac{1}{\sqrt{\mu_r \varepsilon_r}+1} \tag{6}$$

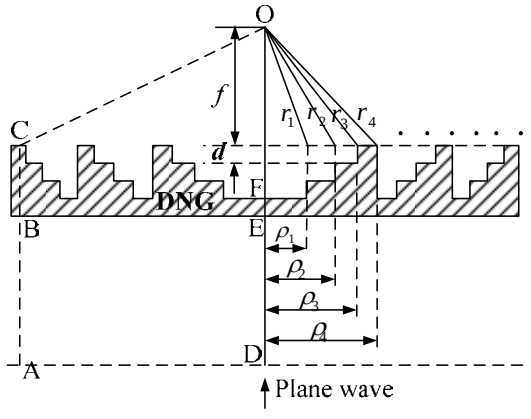


**Figure 2. DNG-BDL.**

## 3. Numerical Results of the DNG-BDL

Among numerous methods for solving DNG problems, FDTD method [15] is a relatively convenient and powerful one, so FDTD method is used to analyze the DNG-BDL in this paper. There existing three types of frequency dispersive FDTD methods: the ecursive convolution (RC) method [16], the auxiliary differential equation (ADE) method [17] and the Z-transform method [18]. The ADE FDTD method is selected here and the Drude model [12,15] is used to model the DNG medium where permeability $\mu(\omega)$ and permittivity $\varepsilon(\omega)$ take the following forms:

$$\mu = \mu_0\left(1 - \frac{\omega_p^2}{\omega^2}\right), \quad \varepsilon = \varepsilon_0\left(1 - \frac{\omega_p^2}{\omega^2}\right) \tag{7}$$

where

$\omega_p$ is the material's resonant frequency.

The perfect lens ($\mu_r = -1$, $\varepsilon_r = -1$) proposed by Pendry in [12] is simulated at first to test our code. The thickness of the DNG slab (denoted by the dashed line) was $d$ = 100 cells in the direction of propagation and the source-to-slab distance was 50 cells in front of the slab, according to Pendry's theory the focus in the slab would occur at the center of the slab and the focus outside the slab would occur at 50 cells beyond the back of the slab. The

 

electric field intensity obtained by our program at frequency 94 GHz after 2000 time steps is shown in **Figure 3**, where S denotes the point source; the focus occurring in and outside the slab agrees well with Pendry's theory.

The BDL designed and analyzed here are axisymmetric, so a symmetry boundary (see **Figure 4**) is set in the computation model to save computation space; the total FDTD region is enclosed by the PML and divided into total-field and scattered-field, the plane wave source is generated by 1D-FDTD method [19] and introduced through the connection boundary of the total-field and scattered-field by a combined total–scattered field formulation [20]; the focal plane field (FPF) is then computed through Stratton-Chu integral of the field at the output-boundary.

The FPF ($f$ = 30e-3) of a 1/2 DPS-BDL ($\varepsilon_r$ = 2.2, contains five zones) was computed using the FDTD code and compared with that obtained by boundary element method (BEM) as shown in **Figure 5**, the two results agree well with each other.

Then several DNG-BDL are designed and analyzed using the FDTD method. Shown in **Figure 6(a)** is the


**Figure 3. The electric field intensity over the DNG slab simulation space.**

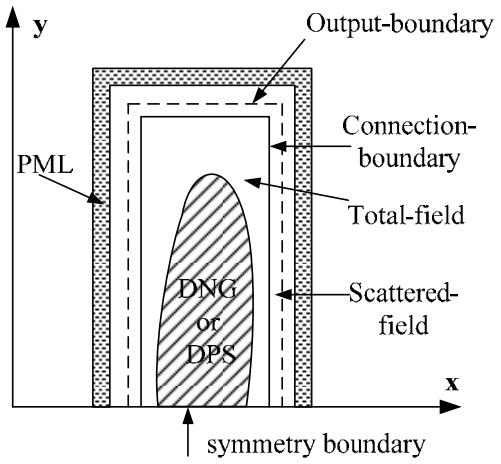


**Figure 4. FDTD computation model.**

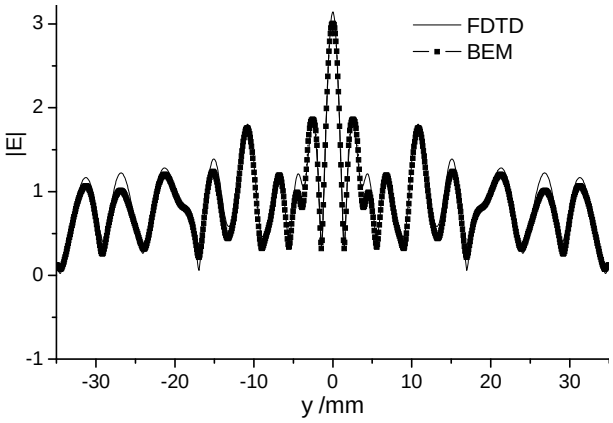


**Figure 5. FPF of a 1/2 DPS-BDL.**

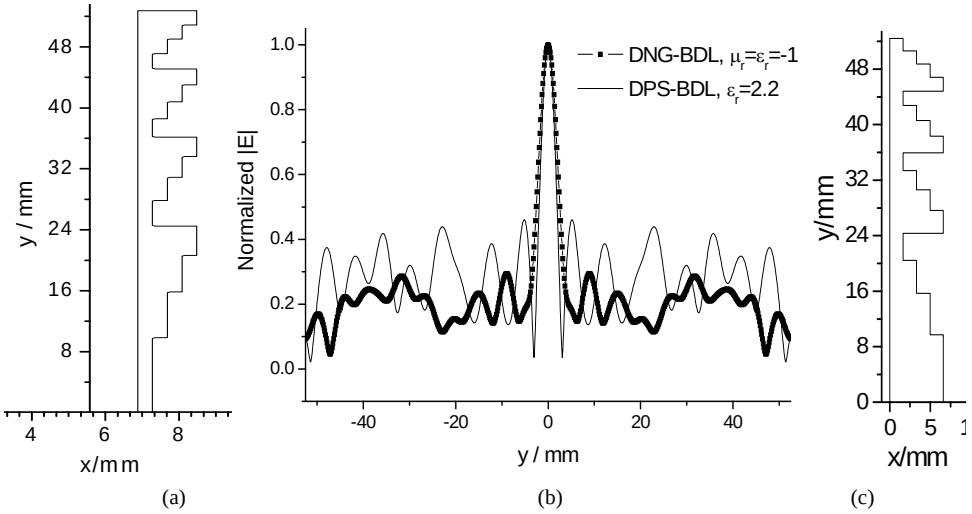


**Figure 6. Focal plane fields of the DNG-BDL($\mu_r$ = –1, $\varepsilon_r$ = –1) and DPS-BDL($\varepsilon_r$ = 2.2) with FN = 1. (a) DNG-BDL; (b) Focal plane field; (c) DPS-BDL.**

 

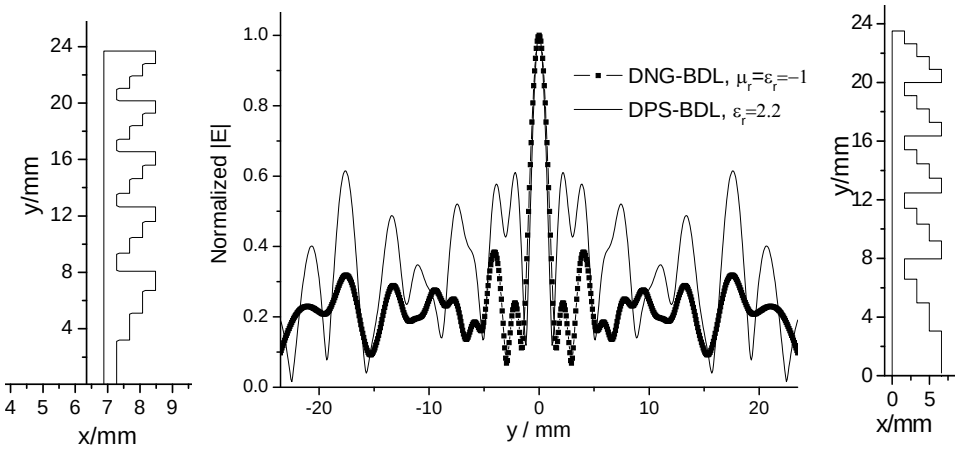


(a) (b) (c)

**Figure 7. Focal plane fields of the DNG-BDL($\mu_r = \varepsilon_r = -1$) and DPS-BDL($\varepsilon_r = 2.2$) with FN = 0.21. (a) DNG-BDL; (b) Focal plane field; (c) DPS-BDL.**

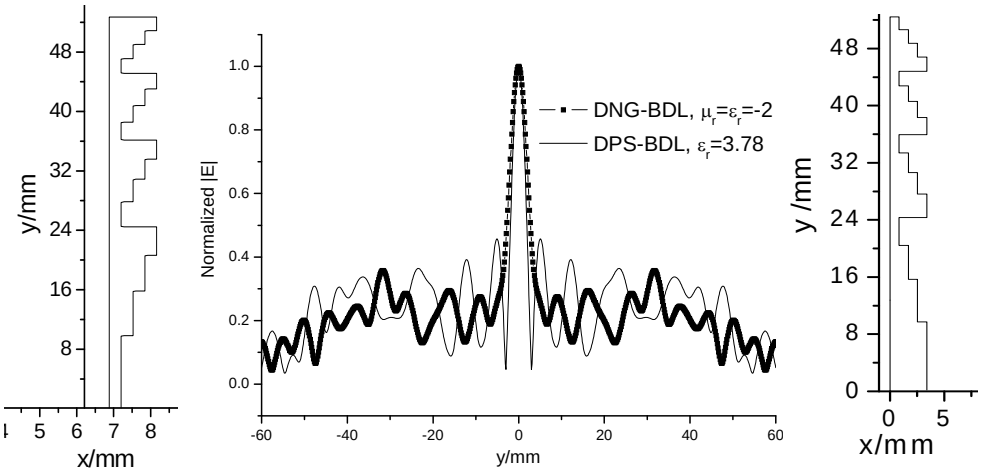


(a) (b) (c)

**Figure 8. Focal plane fields of the DNG-BDL($\mu_r = \varepsilon_r = -2$) and DPS-BDL ($\varepsilon_r = 3.78$) with FN = 1. (a) DNG-BDL; (b) Focal plane field; (c) DPS-BDL.**

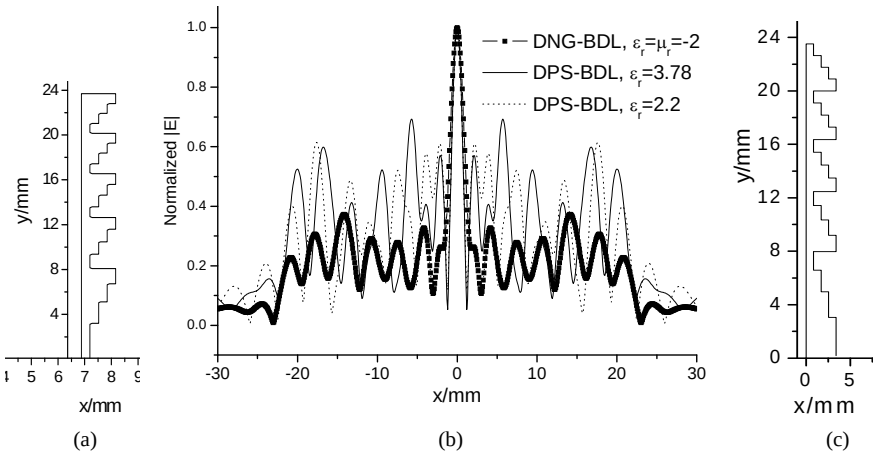


(a) (b) (c)

**Figure 9. Focal plane fields of the DNG-BDL($\mu_r = \varepsilon_r = -2$) and DPS-BDL with FN = 0.21. (a) DNG-BDL; (b) Focal plane field ; (c) DPS-BDL.**

 

structure of a $1/2^2$ DNG-BDL ($\mu_r = -1$, $\varepsilon_r = -1$) with four zones, focal length $f$ = 105 mm and diameter $D$ = 105 mm (FN = 1). The FPF of the DNG-BDL was computed using the FDTD method and compared with that of a DPS-BDL ($\varepsilon_r = 2.2$), see **Figure 6(b)**. The structure of the DPS-BDL with same number of zones, focal length and diameter as that of the DNG-BDL is given in **Figure 6(c)**. It is clear from **Figure 6** that the FPF side lobes of the DNG-BDL are lower than that of the DPS-BDL, as has been explained in section 2 that lower side lobes of the DNG-BDL will be benefit to the imaging qualities.

For BDL of small FN, the FPF side lobes of the DNG-BDL are relatively even much lower than that of the DPS-BDL, an example is shown in **Figure 7** where the focal length of the $1/2^2$ DNG and DPS BDL (five zones) are $f$ = 10 mm, diameter $D$ = 47 mm (FN = 0.21). The FPF of two DNG-BDL with $\mu_r = \varepsilon_r = -2$ and two DPS-BDL with $\varepsilon_r = 3.78$ were also computed. Shown in **Figure 8** are the results of the BDL with focal length $f$ = 105 mm and diameter $D$ = 105 mm (FN = 1); shown in **Figure 9** are results of the small FN BDL with focal length $f$ = 10 mm, diameter $D$ = 47 mm (FN = 0.21). The results in **Figure 8** and **Figure 9** also support the conclusion that smaller FN DNG-BDL has relatively lower side lobes than that of DPS-BDL with same FN, and will get better imaging quality as a result.

## 4. Conclusions

The DNG-BDL which has good characteristics of low profile and small $f$ number is studied in this paper. The design formulas of the DNG-BDL are presented and several DNG-BDL are designed and analyzed using the FDTD method. The focal plane fields of several DNG-BDL are given and compared with that of DPS-BDL; the compared results show that the DNG-BDL with small $f$ number has better focusing characteristics than that of DPS-BDL, and this property makes it very useful to be taken as the objective lens to construct a compact millimeter wave imaging system.

## REFERENCES


[1] V. G. Veselago, "The Electrodynamic of Substance with Simultaneously Negative Values of $\varepsilon$ and $\mu$," *Soviet Physics Uspekhi*, Vol. 10, No. 4, 1968, pp. 509-514.

[2] N. Engheta and R. W. Ziolkowski, "A Positive Future for Double-Negative Metamaterials," *IEEE Transactions on Microwave Theory and Techniques*, Vol. 53, No. 4, 2005, pp. 1535-1556.

[3] A. Shelby, D. R. Smith and S. Schultz, "Experimental Verification of a Negative Index of Refraction," *Science*, Vol. 292, No. 5514, 2001, pp. 77-79.

[4] J. B. Pendry, "Negative Refraction Makes a Perfect Lens," *Physics Review Letters*, Vol. 85, No. 18, 2000, pp. 3966-3969.

[5] G. G. V. Eleftheriades, A. K. Iyer and P. C. Kremer, "Planar Negative Refractive Index Media Using Periodically L–C Loaded Transmission Lines," *IEEE Transactions on Microwave Theory and Techniques*, Vol. 50, No. 12, 2002, pp. 2702-2712.

[6] A. A. Grbic and G. V. Eleftheriades, "Experimental Verification of Backward-Wave Radiation from a Negative Refractive Index Metamaterial," *Journal of Applied Physics*, Vol. 92, No. 10, 2002, pp. 5930-5935.

[7] R. W. Ziolkowski and A. Kipple, "Application of Double Negative Metamaterials to Increase the Power Radiated by Lectrically Small Antennas," *IEEE Transactions on Antennas and Propagation*, Vol. 51, No. 10, 2003, pp. 2626-2640.

[8] M. Skeren, I. Richter and P. Fiala, "Design of Binary Phase-Only Diffractive Optical Elements for Laser Beam Shaping," *Proceedings of SPIE*, Vol. 4095, 2000, pp. 154-164.

[9] S. N. Toma, A. Alexandrescu, D. Apostol, V. Nascov and D. Cojoc, "Gaussian to Rectangular Laser Beam Shaping Using Diffractive Optical Elements," *Proceedings of SPIE*, Vol. 5972, 2005, pp. G1-G8.

[10] D. N. Black and J. C. Wiltse, "Millimeter-Wave Characteristics of Phase-Correcting Fresnel Zone Plates," *IEEE Transactions on Microwave Theory and Techniques*, Vol. 35, No. 12, 1987, pp. 1122-1129.

[11] S. M. Stout-Grandy, A. Petosa, I. V. Minin, O. V. Minin, and J. Wight, "A Systematic Study of Varying Reference Phase in the Design of Circular Fresnel Zone Plate Antennas," *IEEE Transactions on Antennas and Propagation*, Vol. 54, No. 12, 2006, pp. 3629-3637.

[12] R. W. Ziolkowski and E. Heyman, "Wave Propagation in Media Having Negative Permittivity and Permeability," *Physical Review E*, Vol. 64, No. 5, 2001, pp. 1-15.

[13] M. Y. Wang, D. B. Ge, J. Xu and J. Wu, "FDTD Study on Back Scattering of Conducting Sphere Coated with Double-Negatibe Metamaterials," *International Journal of Infrared and Millimeter Waves*, Vol. 28, No. 2, 2007, pp. 199-206.

[14] Z. X. Wang and W. B. Dou, "Design and Analysis of Several Kinds of Dielectric Lens Antennas," *Journal of Electromagnetic waves and Applications*, Vol. 20, No. 12, 2006, pp.1643-1653.

[15] Y. Zhao, P. Belov and Y. Hao, "Accurate Modelling of Left-Handed Metamaterials Using an FDTD Method with Spatial Averaging at the Boundaries," *Journal of Optics A*: *Pure and Applied Optics*, Vol. 9, 2007, pp. S468-S475.

[16] R. Luebbers, F. P. Hunsberger, K. Kunz, R. Standler and M. Schneider, "A Frequency-Dependent Finite-Differen ce Time-Domain Formulation for Dispersive Materials," *IEEE Transactions on Electromagnetic Compatability*, Vol. 32, No. 3, 1990, pp. 222-227.

[17] O. P. Gandhi, B.-Q. Gao and J.-Y. Chen, "A Frequency Dependent Finite-Difference Time-Domain Formulation for General Dispersive Media," *IEEE Transactions on*


 

*Microwave Theory and Techniques*, Vol. 41, No. 4, 1993, pp. 658-664.

[18] D. M. Sullivan, "Frequency-Dependent FDTD Methods Using Z Transforms," *IEEE Transactions on Antennas and Propagation*, Vol. 40, No. 10, 1992, pp. 1223-1230.

[19] W. P. Dennis and S. Y. Shi, "Formulation and Application of the Finite-Difference Time-Domain Method for the Analysis of Axially Symmetric Diffractive Optical Elements," *Journal of Optical Society America A*, Vol. 16, No. 5, 1999, pp. 1131-1142.

[20] K. Umashankar and A. Taflove, "A Novel Method to Analyze Electromagnetic Scattering of Complex Objects," *IEEE Transactions on Electromagnetics Compatibility*, Vol. 24, No. 4, 1982, pp. 397-405.

 

*J. Electromagnetic Analysis & Applications*, 2010, 2, 563-570
doi:10.4236/jemaa.2010.29073 Published Online September 2010 (http://www.SciRP.org/journal/jemaa)

# Scaling Relationships for Input Energy in Electromagnetic Welding of Similar and Dissimilar Metals

**S. V. Desai[1], Satendra Kumar[1], P. Satyamurthy[2], J. K. Chakravartty[3], D. P. Chakravarthy[1]**

[1]Accelerator & Pulse Power Division, Bhabha Atomic Research Centre, Mumbai, India; [2]ADS Target Development Section, Bhabha Atomic Research Centre, Mumbai, India; [3]Mechanical Metallurgy Section, Bhabha Atomic Research Centre, Mumbai, India
Email: Satendra Kumar skdagur@yahoo.com

Received July 2nd, 2010; revised August 18th, 2010; accepted August 23rd, 2010

## ABSTRACT

*In Electromagnetic Welding (EMW) process, the capacitive energy is the source of input energy. The tool that is used for welding comprises of an electromagnetic coil. The job piece to be welded is placed in close proximity with the coil. The welding is achieved by impact, when the colliding job pieces are accelerated towards each other by the Lorentz force. The electromagnetic and mechanical properties/ parameters of the equipment, tool and the job govern the overall welding process. We have described a procedure to calculate the capacitive input energies for jobs of different sizes. Data is given for welding of strips of aluminium, copper and S.S. in similar and dissimilar combinations. Since the EMW technique is used in limited applications, this type of data is not available. We have validated our model with some data available in the literature. It is hoped that, this information will help the designer, to select and standardize the system and process parameters.*

***Keywords*:** *Electromagnetic Welding, Collision Velocity, Capacitor Bank, Lorentz Force, Ringing Frequency, Energy Scaling Relationships*

## 1. Introduction

Electromagnetic Welding (EMW) is the state of art technology in the field of joining of metals. It has numerous advantages (suitability for welding of dissimilar metals being the important one among others), which have been reported earlier [1,2]. However, this technique has some inherent limitations, the major being: 1) lower efficiency for large size jobs (exceeding half a meter) and 2) higher energy requirement for the welding of low electrical conductivity metals. Due to these limitations, the idea of using this technique on wide scale has not received significant attention of the industry. Nevertheless, this technique if applied judiciously, keeping in mind the above facts, can be utilized for some industrial applications. Elaborate analysis of the process and system parameters in Electromagnetic Forming (EMF) has been reported by many authors [3-8]. Copper to brass welding is reported by K.Feas *et al.* [9]. V.Shribman *et al.* have discussed about high strength aluminium welds [10]. Ben Artzy *et al.* have done in depth analysis of the nature of weld interface [11].

The EMF process consists of three stages namely 1) free forming, 2) forming against a die (groove formation) and 3) welding. The energy required for these operations goes on increasing successively. For the process of EMF and EMW, there are no major attempts made in standardization of tool (forming/welding coil), the equipment (energy storage capacitor bank) and the process parameters, which undoubtedly is a formidable task.

We have made a modest effort in this direction, in the field of EMW. The data for input energy for different job sizes helps the designer to select the system components. We have chosen flat strips of similar and dissimilar metals (planar geometry) for analysis, for mainly two reasons: 1) simplicity of coil fabrication and 2) consideration of the fact that comparatively less research work is reported for planar geometry job pieces. In the beginning, we did analysis of electromagnetic Lorentz force based on the parameters of the capacitor bank, the work coil and job piece material. This is being reported separately.

It is found that the collision velocity is the crucial parameter in EMW process. Its dependence on the electro-

 

magnetic parameters and the effect of collision velocity on the welding microstructure has been reportedly recently [12]. It is well known fact that, the aluminium is the easiest metal to form or weld electromagnetically. It can even improve the welding efficiency in case of other metals. In other words, aluminium is best suited as a 'Driver' in EMW process.

In this paper, we are discussing the relationships between capacitor input energy, ringing frequency and the sizes and the materials of the jobs to be welded (in similar and dissimilar combinations). The mathematical model developed by us is validated for the data on welding of S.S. tubes, which is summarized in the end. These relationships are useful to arrive at operating and design parameters of the capacitor bank and the coil, which could possibly eliminate the need of building hardware prototypes.

## 2. Description of the Analytical Approach

The design approach discussed in this paper is based on computational and experimental data. Samples of aluminium, copper and S.S. of different sizes were welded in similar and dissimilar combinations and the corresponding process parameters were calculated by the softwares. It was observed that whenever good welding was achieved, the computed collision velocity for the corresponding operating parameters was of the order of 400 m/sec. Since the sample strips to be welded move in opposite directions (in our experiment), before collision, the velocity of individual strip was 200 m/sec. For the data given in **Table 2**, the computation of collision velocities and experimental verification is done. The input energy values mentioned in **Tables 3-7** are predicted values to achieve the collision velocity of 400 m/sec and hence the welding. The comparison of the measured value for the data from literature and data calculated by our model is given. On the basis of this comparison, the correctness of the predicted values can be justified.

The electrical circuit simulation of the experimental set up (shown in **Figure 1**) was done using MATLAB-SIMULINK. For our set up, the electrical parameters were measured as R=10 mΩ, L=400 nH and C=200 μF. For these values, the circuit was found to be under damped. For a specific value of charging voltage, the software calculated the damped sinusoidal current in the circuit. This was given as input to MAXWELL–SV software, which calculated the values of magnetic field and current induced in the job piece.

The magnetic field density **B** generated by the coil is given by

$$\nabla \times \mathbf{H} = \mathbf{J_c} \quad (1)$$

$$\text{and} \quad \mathbf{B} = \mu \mathbf{H} \quad (2)$$

where $\mathbf{J_c}$ is coil current density and **H** magnetic field intensity.

The electric field density, **E** and current density, $\mathbf{J_w}$ in the job piece are given by

$$\nabla \times \mathbf{E} = -\partial \mathbf{B}/\partial t \quad (3)$$

$$\text{and} \quad \mathbf{J_w} = \sigma \mathbf{E} \quad (4)$$

Lorentz force on the job piece is given by

$$\mathbf{F} = \mathbf{J_w} \times \mathbf{B} \quad (5)$$

The force generated (given by the above equation 5 is unidirectional and is of double the frequency of the input voltage/current frequency. The impulse generated is then given by

$$\text{Impulse} = 2 \int F . dt \quad (6)$$

This impulse is used in plastic deformation and in setting up the collision velocity. A portion of energy is also lost in joule heating and in sonic and light energy during switching in the spark gap. Neglecting the losses during switching, one can write the energy conservation equation as

$$\frac{1}{2} CV^2 = \frac{1}{2} LI^2 = V \sigma . \frac{de}{dt} + I^2 Rt + \frac{1}{2} m v_{max}^2 \quad (7)$$

where term ($V \sigma . \frac{de}{dt}$) represents the plastic strain energy and 'σ' is plastic stress and 'e' is the plastic strain, 'm' is the mass of colliding strip and '$v_{max}$' is the collision velocity.

In EMF process, kinetic energy is fully utilized in forming (free deformation) and in welding process, it is partly used. The remaining kinetic energy is responsible to generate the collision velocity required for impact welding.

The force impulse (calculated by MAXWELL-SV) along with the geometry and mechanical properties were given as input to ANSYS software, which calculated the collision velocity. The properties of the materials used in the calculations are shown in **Table1**.

## 3. Description of the Experimental Work

The experimental layout of the EMW equipment is shown in **Figure 1**. It consists of high voltage power supply, energy storage capacitor bank, spark gap switch and the arrangement of the coil and the job piece. The dis-

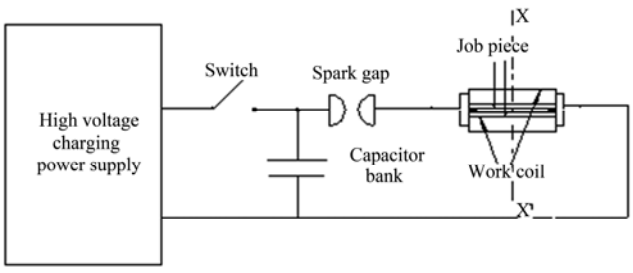


**Figure 1. Schematic of EMW equipment.**

 

**Table 1. Electrical and mechanical properties of the materials.**

| Metal | Electrical Conductivity (S/m) | Mass density ($Kg/m^3$) | Young's Modulus ($N/m^2$) | Yield Strength ($N/m^2$) |
|---|---|---|---|---|
| Al | $38 \times 10^6$ | 2700 | $69 \times 10^9$ | $50 \times 10^6$ |
| Cu | $58 \times 10^6$ | 8900 | $117 \times 10^9$ | $190 \times 10^6$ |
| SS | $1.1 \times 10^6$ | 8000 | $193 \times 10^9$ | $210 \times 10^6$ |

**Table 2. Details of attempted weld samples in our laboratory.**

| Al-Al sample thicknesses in mm | Energy in kJ | Cu-Al sample thicknesses in mm | Energy in kJ |
|---|---|---|---|
| 0.5-0.5 | 4.0 | 0.5-0.5 | 5.0 |
| 0.5-1.0 | 4.5 | 0.5-1.0 | 5.3 |
| 1.0-1.0 | 5.0 | **Cu-Cu sample thicknesses in mm** | |
| 1.0-1.5 | 5.4 | 0.5-0.5 | 6.3 |
| 1.5-2.0 | 5.9 | **Al-S.S. sample thicknesses in mm** | |
| 0.5-3.0 | 6.3 | 0.5-0.5 | 5.2 |
| **Cu-S.S. sample thicknesses in mm** | | 1.0-0.5 | 5.5 |
| 0.5-0.5 | 5.8 | 0.5-0.7 | 5.3 |

**Table 3. Showing energy requirement for welding Al-Al strips of different dimensions.**

| Thickness of the job pieces (mm) | Length of the job pieces (mm) | Energy at 18 kHz ( kJ ) | Energy at 14.7 kHz ( kJ ) | Energy at 12.7 kHz ( kJ ) |
|---|---|---|---|---|
| 1-1 | 70 | 5.00 | 6.25 | 7.17 |
| 2-2 | 100 | 6.37 | 7.87 | 8.95 |
| 3-3 | 150 | 8.87 | 11.00 | 12.70 |
| 4-4 | 200 | 13.12 | 16.25 | 18.67 |
| 5-5 | 300 | 17.62 | 21.75 | 24.95 |

**Table 4. Shows the energies required to weld Cu-Cu strips of different lengths and thicknesses.**

| Thickness of the job pieces (mm) | Length of the job pieces (mm) | Energy at 18 kHz ( kJ ) | Energy at 14.7 kHz ( kJ ) | Energy at 12.7 kHz ( kJ ) |
|---|---|---|---|---|
| 0.5-0.5 | 70 | 6.35 | 8.43 | 9.6 |
| 1.0-1.0 | 100 | 7.95 | 10.30 | 11.67 |
| 1.5-1.5 | 150 | 11.05 | 14.00 | 15.57 |
| 2.0-2.0 | 200 | 16.50 | 19.32 | 23.12 |
| 2.5-2.5 | 300 | 22.30 | 27.00 | 30.87 |

**Table 5. Shows energies required to weld Al-Cu strips of different thicknesses and lengths.**

| Thickness of the job pieces (mm) | Length of the job pieces (mm) | Energy at 18 kHz ( kJ ) | Energy at 14.7 kHz ( kJ ) | Energy at 12.7 kHz ( kJ ) |
|---|---|---|---|---|
| 1(Al)-0.5(Cu) | 70 | 5.37 | 6.70 | 7.70 |
| 1(Al)-1.0(Cu) | 100 | 6.55 | 8.20 | 9.25 |
| 2(Al)-0.5(Cu) | 150 | 6.95 | 8.75 | 10.05 |
| 2(Al)-1.0(Cu) | 200 | 8.62 | 10.25 | 12.00 |
| 2(Al)-2.0(Cu) | 300 | 12.75 | 15.87 | 18.25 |

**Table 6. Shows energies required to weld Al-S.S. strips of different thicknesses and lengths.**

| Thickness of the job pieces (mm) | Length of the Job pieces (mm) | Energy at 18 kHz (kJ) | Energy at 14.7 kHz (kJ) | Energy at 12.7 kHz (kJ) |
|---|---|---|---|---|
| 1(Al)-0.5(S.S.) | 70 | 5.52 | 6.90 | 7.95 |
| 1(Al)-1.0(S.S.) | 100 | 6.75 | 8.45 | 9.55 |
| 2(Al)-0.5(S.S.) | 150 | 7.20 | 9.05 | 10.40 |
| 2(Al)-1.0(S.S.) | 200 | 9.00 | 10.75 | 12.62 |
| 2(Al)-2.0(S.S.) | 300 | 13.50 | 16.87 | 19.50 |

 

**Table 7. Shows energies required to weld Cu-S.S. strips of different thicknesses and lengths.**

| Thickness of the job pieces (mm) | Length of the Job pieces (mm) | Energy at 18 kHz (kJ) | Energy at 14.7 kHz (kJ) | Energy at 12.7 kHz (kJ) |
|---|---|---|---|---|
| 1(Cu)-0.5(S.S.) | 70 | 6.27 | 7.90 | 9.20 |
| 1(Cu)-1.0(S.S.) | 100 | 7.75 | 9.70 | 11.05 |
| 2(Cu)-0.5(S.S.) | 150 | 8.45 | 10.55 | 12.15 |
| 2(Cu)-1.0(S.S.) | 200 | 10.75 | 12.75 | 14.87 |
| 2(Cu)-2.0(S.S.) | 300 | 16.02 | 19.62 | 22.62 |

charge of the capacitor bank creates a damped sinusoidal current in the coil, which induces anti phase currents in the job piece. The interaction of these currents results in the creation of Lorentz force, the latter being responsible for the deformation and impact welding. The isometric view of the arrangement of the welding set up is shown in **Figure 2**. We have adopted the H type coil discussed by T. Aizawa *et al.* [13].

It may be noted that the 'driver' is one of the important components in the assembly. The driver is high conductivity material which is used for the welding of low electrical conductivity metals. We have done extensive experimental and computational work on the performance of the drivers, which is being published separately [14]. A detailed procedure is given for the selection of the dimensions of the drivers and it's frequency dependence. It is found that aluminium is the best driver material to achieve welding in all other metals.

**Figure 2** shows the arrangement for coil, driver, job piece and end connectors. The base width of the coil is '$w_c$' which tapers down to 'w' near the job piece. The end connectors are placed at the ends along longitudinal direction, serve the purpose of providing the separation between the job pieces. They also enhance the induced currents in the job piece. The separation distance, is varied by using the end connectors of different thicknesses. The length of the job piece and the driver was 7cm, for the readings shown in **Table 2**. The job pieces collide with each other and a lap weld joint is obtained by impact.

Due to the limitation of the capacitor input energy and the life of the coil, we have limited our experimental trials for aluminium samples up to 3 mm thickness and that for copper and SS samples up to1mm thickness. The weld length and width in all the cases were 7 cms and 5 mm respectively. These details are given in **Table 2.** It was observed that for a good weld the computed collision velocity was found to be about 400 m/sec, in all these cases. The predicted (extrapolated) energy values for jobs of larger size, in **Tables 3-7** are calculated so as to achieve this velocity. The input energy is worked out by using the soft wares mentioned above. Since there is complete agreement between the computational and experimental observations, it can be conclusively said that the rest of the computational results can predict scaled up energies for jobs of different materials and of larger size. The comparison of the calculated results with the data in the literature is also given in the end.

## 4. Discussion of the Results

It can be observed from **Tables 3-7**, that the input energy goes on increasing with size of the job piece. The energy is the least for welding of aluminium and it successively increases for copper and SS for welding of dissimilar combinations of these metals, the energy requirement is intermediate. When the input energy is applied, the EM force (Lorentz force) is generated in accordance with electrical conductivity of the job piece. Out of the total input energy, some part is spent in spark gap switch (in the form of light and sound). The remaining energy is distributed in the leads and the welding/forming coil. Hence for better efficiency, the lead lengths should be minimized. Out of the energy, coupled to the coil, a part is coupled to job piece, depending on magnetic coupling between the former and the latter. The energy coupled to the job piece is initially spent in deformation of the job piece. Successively higher energy is spent for deformation for aluminium, copper and SS. The kinetic energy

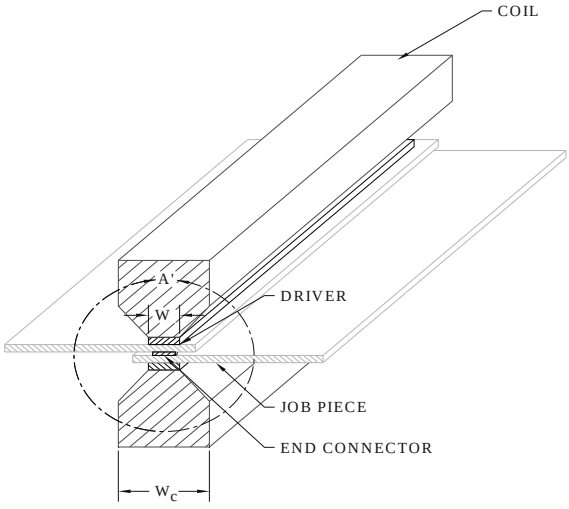


**Figure 2. Shows the arrangement for coil, driver, job piece and end connector.**

 

available for impact welding goes on diminishing in the same sequence. The collision velocity further reduces due to increase in mass density. In order to have good weld joint, the job pieces should have sufficient velocity at the time of collision. Thus the mechanical and electrical properties play crucial role in deciding the collision velocity.

As mentioned earlier, it was explicitly established (from experiments and the computations) that the collision velocity required to achieve weld was of the order of 400 m/sec and is independent of job sizes and the job material. The energies required for other sizes are calculated to achieve this velocity. Thus it is possible to establish scaling relationships with the help of mathematical model.

In EMW/EMF applications, it is desirable to operate at as high frequency as possible. The upper limit is set by the size of overall circuit. **Figure 3** shows the variation of EM force for different frequencies and job piece conductivity values.

**Table 3** shows the values of energy for the welding of aluminium strips of different thicknesses and lengths. The separation distance between the colliding strips was adjusted to 2 mm. The same separation was maintained for the readings in **Table 4** to **7**. The frequency values are calculated for capacitor bank with capacitances of 200 μF, 300 μF and 400 μF, operating at10 kV. In this table, decrease in frequency is observed due to increase of capacitance value. It can also be observed that the energy requirement goes on decreasing with the increase in frequency. This is because of the fact that at higher frequency more magnetic field is contained in the job piece and less magnetic field diffuses out, which results in making the process more efficient. This trend can be observed in all the readings in **Tables 3-7**. The energy requirement increases with length and thickness of the job piece. This due two reasons, viz.-1) There is increase of inductance of the overall circuit and 2) With the increase of thickness, more energy is spent in deformation, resulting in reduction of collision velocity.

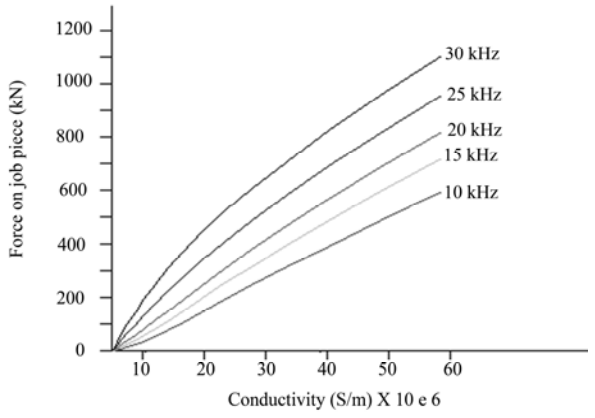


**Figure 3. Variation of EM force with frequency for various conductivity values of the job piece.**

It is desirable to use a capacitor bank of lower capacitance and higher voltage for jobs of larger size and of low conductivity materials. This type of selection can meet the demand of higher energy and higher ringing frequency simultaneously. For welding of the jobs with dimensions larger than that indicated in the tables, the ringing frequencies of the order of 30-40 kHz could be implemented.

**Table 4** shows the values of energy required to weld copper strips of different dimensions, without using aluminium driver. When **Table 3** and **4** are compared, it can be observed that, for the same size, copper needs higher energy as compared to aluminium, to get welded. This is owing to better mechanical strength and mass density of the former.

**Table 5** shows the energy values to achieve welding of aluminium and copper strips of different sizes. For the results shown in **Tables 5, 6** and **7** aluminium drivers of 70 mm length, 5 mm width and 0.5 mm thickness was used to drive the copper and S.S. strips. When the readings in **Table 4** and **5** are compared, it can be observed that Al-Cu combination requires less energy as compared to Cu-Cu combination (compare reading 2 from **Table 4** and reading 2 from **Table 5**).This is quite obvious, owing to the fact that Cu is mechanically stronger than Al.

**Table 6** shows the energy values to achieve welding in aluminium and S.S. strips of different sizes. It can be observed from **Table 5** and **6** that welding of Al-S.S. needs higher energy than Al-Cu, owing to better mechanical strength and mass density of S.S. as compared to that of copper.

From **Table 6** and **7**, one can observe that the energy required for welding of Cu-S.S. is higher than the corresponding combination of Al-S.S. This is again due to better mechanical properties of S.S. than that of copper.

The readings from **Tables 3-7** can be broadly summarized as follows-

1) The energy requirement increases with the increase in the dimensions of the job piece.

2) The energy requirement increases at lower frequencies due to increase of diffused out magnetic field, resulting in reduction in energy available for generating the velocity.

3) Aluminium needs the least energy for welding.

4) It is found that welding can be achieved at lesser energy for other similar and dissimilar welding combinations. Hence the use of aluminium as a driver is recommended.

5) The energy requirement goes on increasing successively for the combinations Al-Al, Al-Cu, Al-S.S.,

 

Cu-Cu and Cu-S.S. This could be explained on the basis of mass density and electrical and mechanical properties of the metals involved in the process.

6) It is interesting to note that in even case of copper the welding can be achieved at less energy. This explained elaborately in [14].

The **Figures 4-9** show the photographs of samples welded in our laboratory.

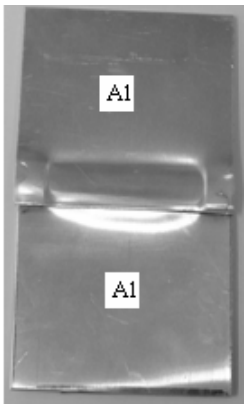


**Figure 4. Al-Al welded sample.**

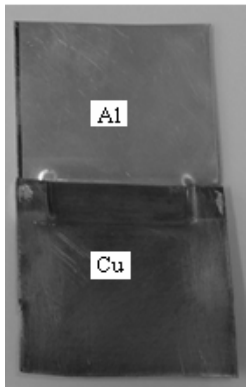


**Figure 5. Al-Cu welded sample.**

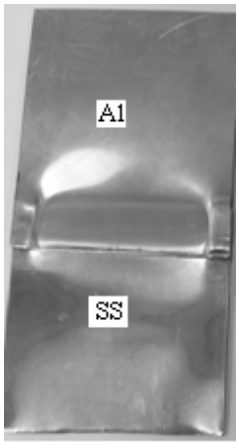


**Figure 6.Al-S.S. welded sample.**

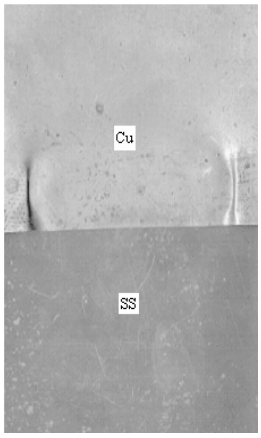


**Figure 7. Cu-S.S. welded sample.**

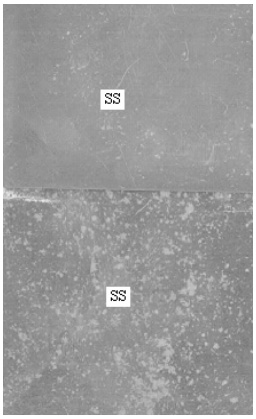


**Figure 8. S.S.-S.S. welded sample.**

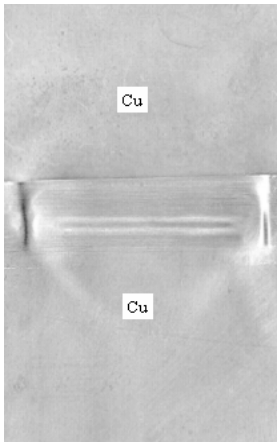


**Figure 9. Cu-Cu welded sample.**

## 5. Comparison of the Computed Results with EMW System for Fabrication of S.S. Fuel Pins

We have done the validation of our computational model with the data available for the welding set up reported by

 

**Table 8. Data used in computational model.**

| Sr. No | Details of components / operational parameters | Numerical data |
|---|---|---|
| 1 | Capacitor bank ratings | 37.5 μF, 50 kV, 47 kJ |
| 2 | Actual charging voltage | 37.5 kV |
| 3 | Total circuit inductance | 27 nH |
| 4 | Outside diameter of the inductor coil | 10.2 mm |
| 5 | Length of the inductor coil | 16.0 mm |
| 6 | Inside diameter of the inductor coil (O.D. of the fuel pin) | 5.84 mm |
| 7 | Wall thickness of fuel pin | 0.38 mm |
| 8 | Taper angle of the end plug | $5^0$ |
| 9 | Acceleration step | 0.25 mm |
| 10 | Material of fuel pin and end plug | S.S. 316 |

**Table 9. Comparison of the data.**

| Sr.No. | Parameter | Data reported in ref. [10] | Data calculated by our model |
|---|---|---|---|
| 1 | Mag.field generated, $B_{(max)}$ | More than 50 T | 55 T |
| 2 | Peak current | 1.25 MA | 1.40 MA |
| 3 | Ringing frequency | 165 kHz | 165 kHz |
| 4 | Pressure generated | In excess of 689 MPa | 840 MPa |
| 5 | Collision velocity | 305 m/sec (measured) | 330 m/sec |

W.F.Brown *et al.* [15] which describes the electromagnetic welding of SS fuel pins used in the breeder reactor. They have used 47 kJ, 50 kV capacitor bank to achieve the welding of SS fuel pins with the end enclosure, using a single turn inductor. The weld results are qualified by mechanical and metallurgical tests. The data shown in **Table 8** is taken as input data in our computational model.

**Table 9** shows the comparison of the values reported in [10] and the values computed by our model. It can be observed that there is good amount of agreement.

It is interesting to note that the value of measured collision velocity (305 m/sec) reported in [10] is closely matching with the value calculated by our model (330 m/sec). This observation underlines the correctness of our computational model.

## 6. Conclusions

It is possible to establish scaling relationships for the input energies for welding of jobs of different sizes and the materials, in the case of EMW process. It is also possible to decide appropriate values of the capacitance and voltage for the capacitor bank, depending on the size of the job. The correctness of the computational model is validated, using the data available on welding of S.S. tubes. This analysis gives important inputs for the predictive design and the standardization procedures and is equally applicable for tubular jobs.

## 7. Acknowledgements

We thankfully acknowledge the help rendered by our colleague M. R. Kulkarni, during the experiments. Sincere thanks are also due to Dr. L. M. Gantayet, Director, BTD Group for encouragement and support for this activity.

## REFERENCES

[1] S. Kumar, S. V. Desai, M. R. Kulkarni and D. P. Chakravarthy, "Development of Electro-Magnetic Welding Technique for Similar and Dissimilar Metal Strips," National Welding Seminar-2008, Mumbai.

[2] S. Kumar, S. V. Desai, M. R. Kulkarni and D. P. Chakravarthy, "Electro-Magnetic Welding of Copper to Stainless Steel," National Welding Seminar-2009, Kolkata.

[3] S. T. S. Al Hassani, J. L. Duncan and W. Johnson, "On the Parameters of the Magnetic Forming Process," *Journal of Mechanical Engineering Science*, Vol. 16, No. 1, pp.1-9.

[4] S. T. S. Al Hassani, J. L. Duncan and W. Johnson, "The Influence of the Electrical and Geometrical Parameters in Magnetic Forming," *Proceedings of the 8th International MTDR conference*, Manchester, UK, September 1967.

[5] K. Baines, J. L. Duncan and W. Johnson, "Electromagnetic Metal Forming," *Proceedings of the Institution of Mechanical Engineers*, 180 (Pt. 1) 1965-6 4, 93.

[6] S. T. S. Al Hassani, J. L. Duncan and W. Johnson, "Analysis of the Electromagnetic Forming Process," *Proceedings of Cooperative Institutional Research Program*, ASTME conference U.S.A., September 1967.

 

[7] G. K. Lal and M. J. Hillier, "The Electrodynamics of Electromagnetic Forming," *International Journal of Mechanical Science*, Vol. 10, No. 6, 1968, pp. 491-500.

[8] G. K. Lal, "Electromagnetic Metal Forming," *IEEE Transactions on Industrial Applications*, 1972, pp. 425-429.

[9] K. Feas, T. Baaten, W. D. Waele and N. Debroux, "Joining of Copper to Brass Using Magnetic Pulse Welding," *4th International Conference on High Speed Forming*, 2010, pp. 84-96.

[10] V. Shribman, A. Stern, V. Livshitz and O. Gafri, "Magnetic Pulse Welding Produces High Strength Aluminium Welds," *Welding Journal*, Vol. 81, 2002, pp 33-37.

[11] B. Artzy, A. Stern, N. Frage and V. Shribman, "Interface Phenomena in Aluminium-Magnesium Magnetic Pulse Welding," *Science and Technology of Welding and Joining*, Vol. 13, No. 4, 2008, pp. 402-408.

[12] S. V. Desai, S. Kumar, P. Satyamurthy, J. K. Chakravartty and D. P. Chakravarthy, "Analysis of the Effect of Collision Velocity in Electromagnetic Welding Process of Aliminum Strips," accepted for publication in *International Journal of Electromagnetics and Mechanics* in May 2010.

[13] T. Aizawa, K. Okagawa, M. Yoshizawa and N. Henmi, "Impulse Magnetic Pressure Seam Welding of Aluminium Sheets," *Impact Engineering and Applications*, 2001, pp. 827-832.

[14] S. V. Desai, S. Kumar, P. Satyamurthy, J. K. Chakravartty and D. P. Chakravarthy, "Improvement of Performance of Electromagnetic Welding Process by Use of Driver Materials," accepted for publication in *International Journal of Electromagnetics and Mechanics* in 2010.

[15] W. F. Brown, J. Bandas and N. T. Olsan, "Pulsed Magnetic Welding of Fast Breeder Reactor Fuel Pin End Closures," *Welding Journal*, Vol. 57, No. 6, 1978, pp. 22-26.

 

*J. Electromagnetic Analysis & Applications*, **2010, 2, 571-579**
doi:10.4236/jemaa.2010.29074 Published Online September 2010 (http://www.SciRP.org/journal/jemaa)

# Monitoring Electromagnetic Field Emitted by High Frequencies Home Utilities

**Emanuele Calabrò, Salvatore Magazù**

Department of Physics, University of Messina, Messina, Italy
Email: e.calabro@yahoo.com, smagazu@unime.it

Received June 5th, 2010; revised August 19th, 2010; accepted August 26th, 2010

## ABSTRACT

*The aim of this study is to provide measurements of the electromagnetic field due to the 'electrosmog' emitted by some home electronic devices in the range of microwaves frequencies. The enormous increase in the use of mobile telephony throughout the world, microwave ovens, cordless phones and other high frequency home utilities suggests accurate measures of microwaves power density emitted by such devices to check that the exposure limits suggested by the International Commission on Non-Ionizing Radiation Protection are not exceeded. Measurements were carried out by a Narda SRM* 3000*. Spectrum analysis mode was chosen as a preliminary analysis to quantify the frequencies intensities of electromagnetic waves. Time analysis was successively conducted to operate selective and continuous measurements at a fixed frequency, allowing temporal check of power density and the related electromagnetic field components emitted by high frequencies home electronic devices.*

***Keywords*:** *Electrosmog, Electromagnetic Field, Microwaves, High Frequency, Mobile Phone*

## 1. Introduction

The achievement of electronics in all technological sectors and the growing demand for electric power have generated exposures of living beings to high frequencies electromagnetic field (HF-EMF).

Power lines, electric generators and motors, electric appliances, electronic devices and wireless communication systems generate electric and magnetic fields.

EMFs are produced everywhere in our homes, because of electrical wiring and very common devices such as electronic household appliances, mobile phone, microwave ovens, computers or television sets. Significant changes are afoot in the telecommunications sector, thanks to progress made in the new UMTS technologies, which allow the transmission of huge amounts of data on the airwaves and signal repeaters or mobile phone aerials.

All these technological environment produces a continuous electromagnetic waves emission, a phenomenon that has come to be known as 'electrosmog', a term coined in the 1970s. The part of the word 'smog' derives from the description of heavy industrial pollution where a mixture of smoke and fog produced horrendous clouds of air pollution in cities due to industrial processes. Electrosmog describes the dirt of electromagnetic pollution that is invisible and undetectable. It can be considered as the sum of all radiation coming from artificial sources in our environment.

The radiation produced by electrosmog can be broken down into different types.

Electrical fields are generated between two poles of opposite electrical potential. The closer these poles are to each other the stronger the field between them. It is not necessary for electrical current to flow in order to generate an electrical field because electric fields occur whenever a voltage difference occurs. Hence, any electrical device whether switched on or off will be a source of electrosmog. This is particularly true for cables hidden in walls and floors and therefore they represent a potential source of extremely low field (ELF) electromagnetic radiation.

Electric field component is usually not very strong in a building. High electric-field areas are found near TV or computer monitors, fluorescent lights or light dimmer controls and a safe distance from the field source is 1 meter at least. Electric fields are high near high-voltage power lines, but these fields rarely penetrate into a house.

In contrast, magnetic field component is much more common at home than electric field. Magnetic fields are

 

generated when electricity flows through electrical conductors. Like electric fields, they produce current in the body. Most of the recent health concerns have been about magnetic fields.

The main sources of ELF magnetic fields are electrical appliances, power lines or underground power cables, transformers, motorized equipment, computers and any modern electronic equipment.

New wireless technologies produced the electromagnetic contamination as electrosmog in the ranges of radiofrequency (RF) and microwaves (MW) generated by HF-EMFs. RF frequency range occurs from 100 kHz to 300 MHz, MW are at frequencies falling between 300 MHz and 30 GHz on the electromagnetic spectrum. Almost all RF-MW radiation is man-made, produced by satellites, radar, radio, mobile phone, baby-phones, cordless telephones, bluetooth and more, in order to enable technical applications such as signals traveling over long distances.

HFs EMF can be produced either by nearby transmission towers or by central stations of mobile phones, while the field of a low frequency is mainly spread by the equipment in the home, as well as by electrical wiring.

Since 1970s, base stations for mobile telecommunication have been spreading across the urban centres, increasing the electromagnetic contamination in the RF-MW range.

Mobile phone devices use electromagnetic radiation in the microwave range, at frequency bands usually close to 900 and 1800 MHz that can interfere in the nervous system of organisms.

In spite of the great number of studies performed, knowledge about the adverse effects of RF and MW radiation on human health, or the biological responses to their exposure, is still limited [1,2].

Many scientific studies have investigated possible health effects of mobile phone radiations. An assessment published in 2007 by the European Commission Scientific Committee on Emerging and Newly Identified Health Risks (SCENIHR) concluded that no significant health effect has been demonstrated from mobile phone radiation at normal exposure levels. However, more studies concerning potential health effects on children are needed [3].

Some scientific studies focused on the danger of MW radiation for health in humans and animals [4]. It was demonstrate that animals exposed to RF-MW field in the vicinity of transmitting antennas show conspicuous abnormalities [5,6].

It was found that RF-MW radiations produce a response in many types of neurons in the avian Central Nervous System [7]. MW radiation emitted by mobile phones can affect central cholinergic activity in the rat [8] and their learning memory tasks [9]. Furthermore, effects on blood-brain barrier permeability [10,11] and oxidative damage in brains tissues [12] were observed.

Karinen *et al*. [13] demonstrated that protein expression in human skin can be affected by the exposure to RF-EMF. Calabrò *et al.* [14] observed changes in heat-shock proteins expression of human neuronal-like cells exposed to MW radiations. In addition, several studies proved that the exposure to RF-MW radiation can alter DNA and gene structures [15-17].

In view of previously effects of RF-MW radiations, various authorities have long defined limit values to protect people from excessive exposure.

National radiation advisory authorities have recommended measures to minimize exposure to their citizens, following the Guidelines for exposure limits to electromagnetic fields of the International Commission on Non-Ionizing Radiation Protection (I.C.N.I.R.P.) [18].

However, it becomes necessary to avoid overexposure to electromagnetic waves and to make sure that installations are carefully and regularly monitored. Hence accurate measures need for monitoring power density and EMF emitted by the most used electronic devices in our home, particularly those emitting RF-MW radiations.

## 2. Materials and Methods

The value of electrosmog is generally measured by means of monitoring stations located in the vicinity of or inside the critical zones. The instrument used is available not only to the cantonal or local council authorities, but also to the population.

Electrosmog-meter-detector such as Gaussmeter, Teslameter, ELF-meter, are needed to measure the level of ELF-EMF produced by power lines, computers, TVs, kitchen appliances, enabling to find hidden sources of ELF frequency magnetic fields, and determining the effectiveness of eventual electric shielding devices.

HF-meter/detector can be used to measure the electromagnetic field emitted by high frequency appliances and devices.

A SRM-3000 instrument of Narda Safety Test Solutions was chosen to measure the electromagnetic field components related to three typical high frequency home utilities. Narda SRM 3000 frequency range can vary from 100 kHz to 3 GHz. It was linked through a cable to a Narda three axis antenna covering the frequency range from 75 MHz to 3 GHz, determining the three spatial components of the EMF being measured.

The "Spectrum Analysis" mode of the device was chosen as preliminary analysis. This function enables to detect and quantify the frequencies values relative to the electromagnetic waves impinging the three axis antenna. Hence, in Spectrum Analysis mode all the field compo-

 

nents in the environment can be detected and measured. The frequency range in Spectrum Analysis can be set by entering the upper and lower frequencies. Spectra analysis represented in **Figure 1** and **Figure 3** were carried out by setting a narrow frequency range so that the maximum number of frequencies can be detected.

Otherwise, only signals which are separated by a frequency greater than the defined resolution bandwidth (RBW) can be distinguished from one another. Hence the RBW characterizes the selectivity of the spectrum analyzer in respect of signals having the same amplitude.

The SRM-3000 can automatically define a suitable RBW, depending on the selected frequency span. This function gave the value RBW = 6 MHz for the spectral analysis shown in **Figure 1** and **Figure 3**.

The Average Mode was chosen as result type, and the average of the measured values were taken over a number of 16 results.

In "Time Analysis" mode, the device can provide selective and continuous measurements at a fixed frequency, allowing temporal check of power density of radiation. In addition the intensities of the related electric and magnetic field components can be monitored. This operating mode is ideal for timer-controlled measurements since the instrument mode enables one to carry out selective measurements at a defined frequency, to monitor the EMF level at the selected channel.

This operating mode function produces that RBW can be selected to match the channel bandwidth, averaging over a user defined time period, e.g. 6 minutes. Better results were obtained at RBW = 5 MHz.

Spectrum and Time analysis results were transferred to a PC for monitoring the electromagnetic components related to the RF-MW emitted during some conversations by mobile phones and cordless telephones, and during microwave ovens working.

Mobile phones, microwave ovens and cordless telephones have been considered the most representative home electronic utilities emitting in the range of MW radiation.

The mobile phones Nokia 1208, LG model U8330, Motorola V635, the microwave ovens Whirlpool Model AVM 541/WP/WH, Termozeta MW 250 D, Samsung CE 137, and the cordless telephones Brondi DC3010, Siemens Gigaset A38H, were used to measure MW radiation emitted during their working.

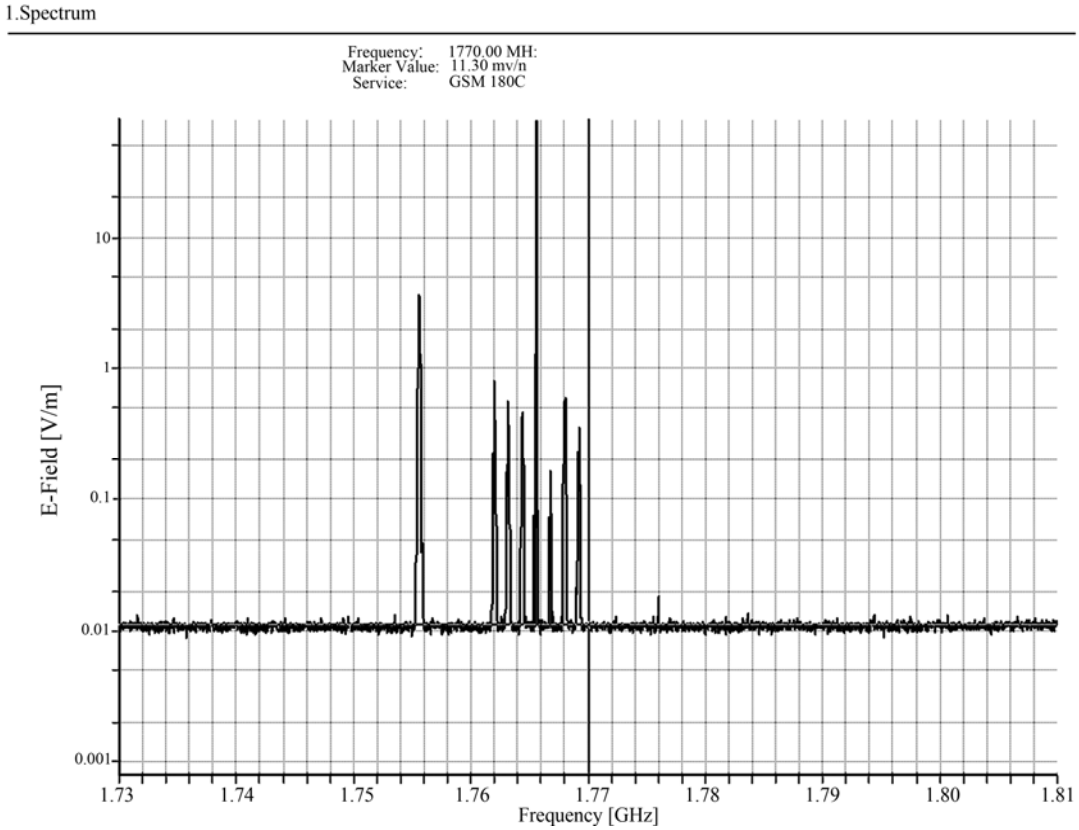


**Figure 1. A representative spectrum analysis of the electric field component measured by Narda SRM 3000 at 2 cm from a mobile phone Nokia 1208 during a conversation. The limit of 59 V/m suggest by the ICNIRP for the electric component was exceeded at 1766 MHz.**

 

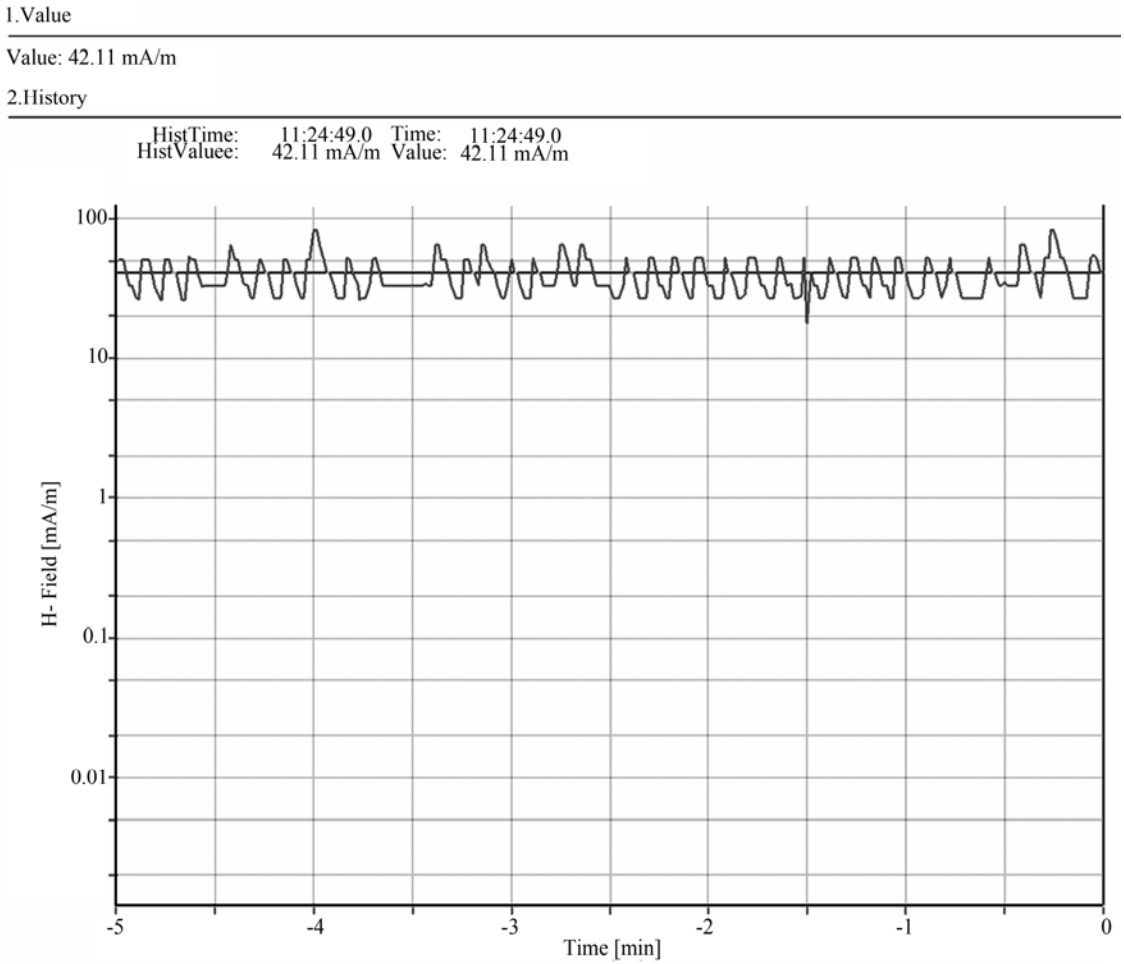


**Figure 2. A typical time analysis of the magnetic field component measured by Narda SRM 3000 at 2 cm from a mobile phone Nokia 1208, with respect to a frequency centred at 1757 MHz during an exposure.**

## 3. Results and Discussion

A typical house consists of a matrix of wires throughout the walls and ceilings. Moreover home devices or appliances are particularly MW sources, above all mobile phones and transmission masts, Wi-Fi systems and cordless phones.

First, we must differentiate between thermal and non-thermal effect of RF-MW radiations.

Whereas electric currents flow inside the body when ELF is concerned, the radiated energy within the body in HF fields is mainly transformed into heat, and the temperature increase in the organism can cause damage.

The unit used to measure it is the Specific Absorption Rate (SAR) which is given in watts per kilogram and its maximum levels for modern handsets have been set by governmental regulating agencies. In the USA a SAR limit of 1.6 W/kg has been assigned, averaged over a volume of 1 gram of tissue, for the head. In Europe, the limit is 2 W/kg, averaged over a volume of 10 grams of tissue.

Second, it must be taken into account that besides the thermal effect, the so-called “non-thermal effect” of the fields can have a negative influence on the biological system, an effect which can occur even when the radiation emission is extremely low. Persons working in MW fields have reported headaches, eyestrain, over-all fatigue and disturbance of sleep. These effects have been associated with the interaction of the MW fields with the central nervous system of the body. Such effects have been labeled as "non-thermal" interactions. These may be responsible for some of the long-term effects from prolonged exposure to low levels of EMFs. There is no confirmed scientific evidence to prove a link between such effects and MW exposure. However, accurate monitoring need to check that exposure limits recommended by I.C.N.I.R.P., at least, are not exceeded.

Results reported here strictly depend on the local base station to which mobile phone signal was transmitted. In

 

fact, when a user of a mobile phone makes a call, it is transmitted to the nearest base station, which receives and transmits radio signals in its area. The area covered by a base station is called a "cell". The number of cells varies in different areas, depending on the volume of use. Areas with a high volume of mobile phone use will have more cells, and as the phone user moves around, the radio signal can be switched from one cell to another, maintaining a good connection.

The total power output of a typical mobile phone base station depends on the type of antenna, the number of analog and digital channels that operate at a given time and at their maximum strength, and the antenna gain which gives the signals direction and strength. In addition, the power level generated by a mobile phone to maintain a good connection depends on the distance from the base station: more power is needed for great distances from the base station within a cell.

The power output is less when the base station is close to the phone user. Hence, base stations are being placed closer together, to make it simpler for a phone and a base station to communicate reliably and to minimize the power output of a mobile phone.

This fact suggests particular checks of power level during cellular phone calls in areas with a low volume of use, because a great distance from the base station could increase the power output of a typical mobile phone working.

Measurements were carried out in South-Italy to check that the power density at 1-2 centimetres from some cellular phones was lesser than 9 $W/m^2$ (resulting from the expression f / 200 as to the frequency of 1800 MHz) in line with the Guidelines for public exposure limits to electromagnetic fields [18].

Analogue checks were performed with respect to the electric and magnetic components of the electromagnetic field.

The magnetic field component H should be lesser than 111 mA/m (as to 900 MHz band) and 159 mA/m (as to 1800 MHz band), resulting from the expression $H < 0.0037\ f^{1/2}$ ($Am^{-1}$) reported on **Table 7** of the mentioned Guidelines. Finally, the intensity of the electric field component E must not exceed the limit of 59 V/m resulting from the expression $E < 1.375 f^{1/2}$ [18].

Several measures were performed by spectrum analysis mode of Narda SRM 3000 to find the exact frequency values where the highest peaks occur during a call, connecting with local phone networks such as Vodafone or Wind. A representative spectrum analysis of the electric field component measured at 2 cm from a mobile phone Nokia 1208 during a call is shown in **Figure 1**.

**Figure 1** shows as the radiation emitted by a mobile phone working consists of a number of peaks at different frequencies close to 1800 MHz, whose intensities change continuously during the conversation, due to the continuous connections to the local base station as above specified. In particular, the spectrum represented in **Figure 1** shows that the limit of 59 V/m for the electric component was exceeded at the frequency of 1766 MHz during a measurement. Nevertheless the peak intensities of EMF frequencies change continuously during mobile phone working, as it can be observed by time analysis mode.

A typical time analysis of the magnetic field component due to the MWs emitted by the same mobile phone during a conversation is represented in **Figure 2** with respect to a frequency centred at 1757 MHz, where appeared that the limit of 159 mA/m was not exceeded during an exposure of 5 minutes at that fixed frequency.

Microwave oven is another common device often used at home. The source of the radiation in a microwave oven is the magnetron tube, which converts powerline electric current to electromagnetic radiation around 2450 MHz.

The high voltage (about 3,000 or 4,000 volt) which powers the magnetron tube is produced by a step-up transformer rectifier, and filter which converts the AC of line voltage to 4 kV DC.

The microwave energy from the magnetron is transferred to the oven cavity through a waveguide section. Heat is produced when the water molecules in the food vibrate (at a rate of 2,450,000,000 times per second) when the food absorbs the microwave radiation. The movement of the molecules produce friction which causes heat.

Microwave ovens are heavily shielded to stop leakage and shut off automatically if the door is opened. Nonetheless, microwave ovens use a lot of grid electricity and produce high levels of power frequency EMF as much as 200 mG at 50 centimeters.

Typical levels of radiation leakage from microwave ovens is about 0.2 $mW/cm^2$.

A spectrum analysis was acquired at 30 cm from the door of a working Whirlpool AVM 541/WP/WH. Spectrum analysis of the electric component was represented in **Figure 3(a)**, in which a maximum appears around 2470 MHz within a range of exposure from 2400 to 2480 MHz. Spectrum analysis of magnetic component was represented in **Figure 3(b)**, as well. Such results showed that electric and magnetic components related to the MW radiation do not reach high values during microwave ovens working, as confirmed by other measurements carried out on the microwave ovens devices listed in section 2.

Furthermore, the relative measured power frequency electromagnetic field was lesser than 100 $mW/m^2$, as shown in **Figure 4** at the same exposure conditions.

 

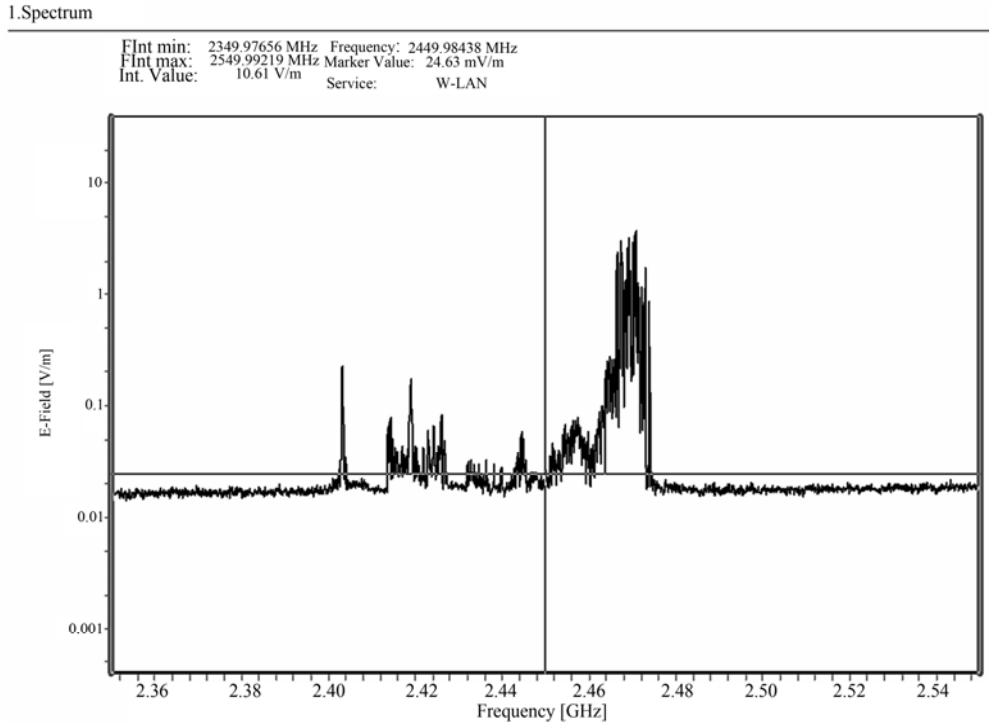


(a)

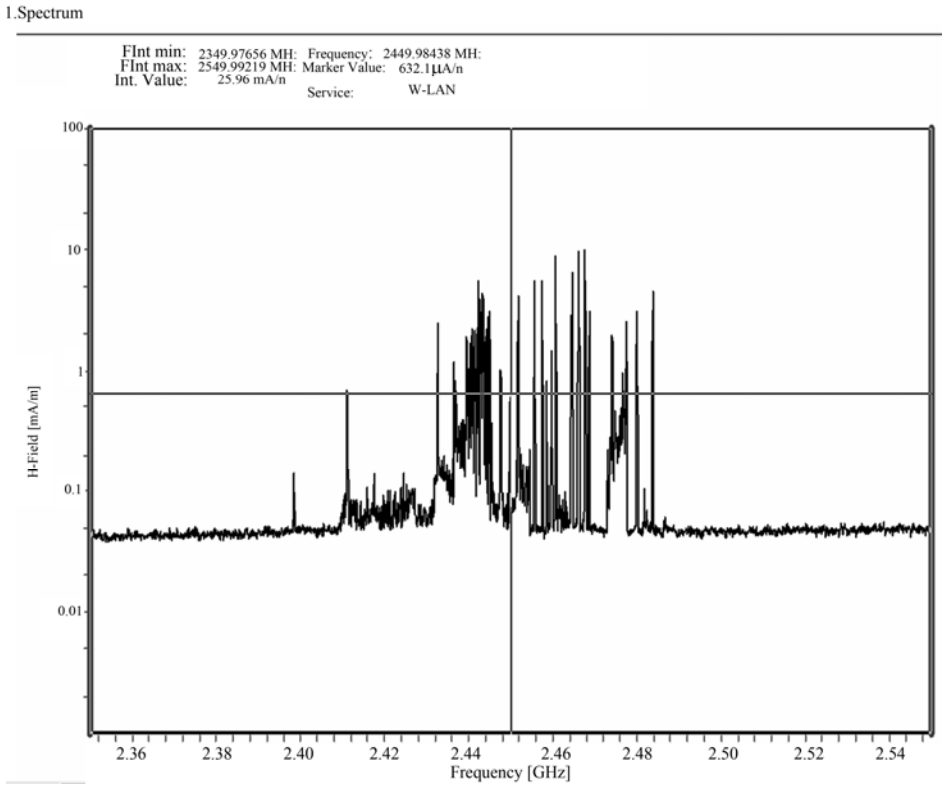


(b)

**Figure 3. (a) A representative spectrum analysis performed by Narda SRM 3000 in the range of 2400-2500 MHz of the electric component related to MW radiations generated by a working microwave oven Whirlpool Model AVM 541/WP/WH, acquired at 30 cm from the door's device; (b) Spectrum analysis of the magnetic component emitted by a microwave oven Whirlpool Model AVM 541/WP/WH at the same exposure conditions illustrated for Figure 3(a).**

 

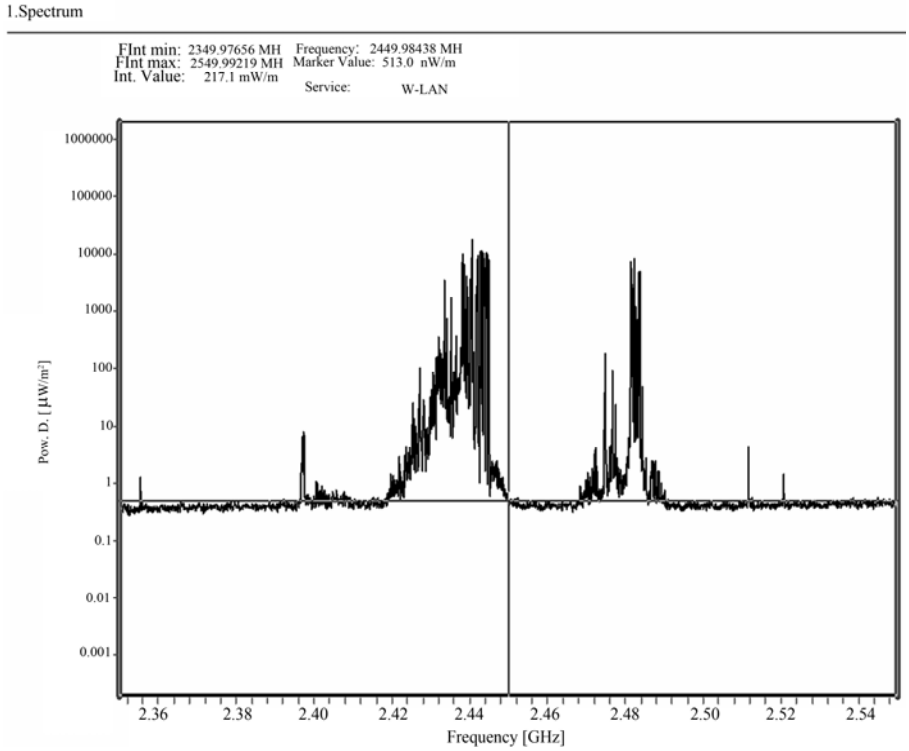


**Figure 4. A typical spectrum analysis of the relative power density emitted by a microwave oven Whirlpool Model AVM 541/WP/WH, measured at the same exposure conditions indicated for Figure 3(a) and Figure 3(b).**

Some standards applied to microwave ovens sets safe exposure limits as follows.

In U.S.A. the ANSI/IEEE-C95.1-1991 stated that the power density of a microwave oven should not exceed 1.6 mW/cm$^2$ at 2450 MHz for human exposure in uncontrolled environments.

Otherwise the IRPA (International Radiation Protection Association) Guidelines recommends exposure limit of 5 mW/cm$^2$ for RF workers and 1 mW/cm$^2$ for the general public. These exposure limits are averaged over 6 minutes period.

Regarding cordless telephone system the handset is not wired to its base unit, but wireless communication techniques between a remote handset and its base unit is used, permitting a user to move freely and not be physically restricted by a telephone cord.

The base unit provides a wireless connection to a handset. The handset is capable of receiving and transmitting signals over a wireless link to the base unit. The handset can be removed from the base unit and used within a predetermined range, which is limited by the RF signal strength and not cord length. Cordless telephones typically operate over a RF portion of the spectrum set aside for general public use. The frequency band is broken up into a number of channels that may be used by the handset and base station. Only a relatively small portion of the radio spectrum has been allocated to cordless telephones and these telephones operate on a selected band of a relatively few channels, as can be observed in **Figures 5(a),(b)**.

The RF link either transmits the voice signals between the base unit and the remote handset using frequency modulation techniques or using digital techniques such as quadrature amplitude modulation or frequency shift keying. The RF link between the handset and the base unit is typically divided into two portions, such as an uplink from the handset to the base unit at a first frequency, and a downlink from the base unit to the handset at a second frequency.

DECT base stations transmit signals permanently, 24 hours a day, even when the phone is not being used. The small installation works just like a big one with pulsed radio signals, pulsed at 100 Hz in the low frequency range and high-performance in the HF typical range between 1800 and 1900 MHz. Spectral analysis of power density and magnetic component of MW emitted by the model Brondi DC3010 are shown in **Figure 5(a)** and **Figure 5(b)**, respectively.

It was verified that the limit of [18] was not exceeded and that the exposure occurs within a narrow frequency range from 1880 and 1890 MHz.

The increase of temperature in cordless devices is gene-

 

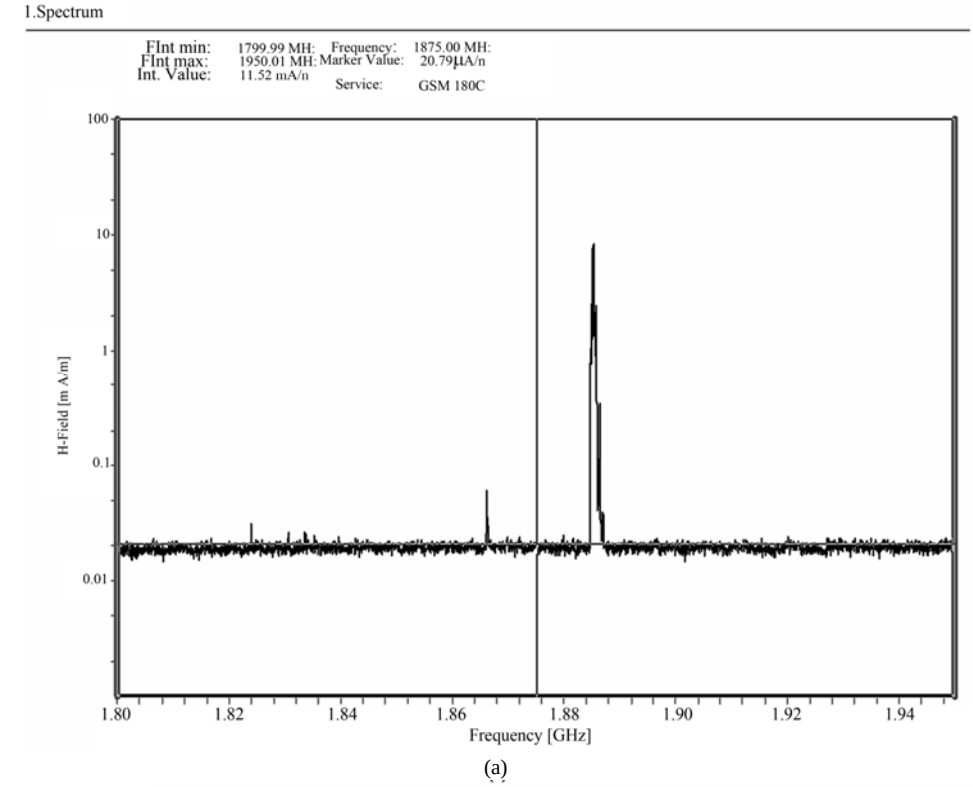


(a)

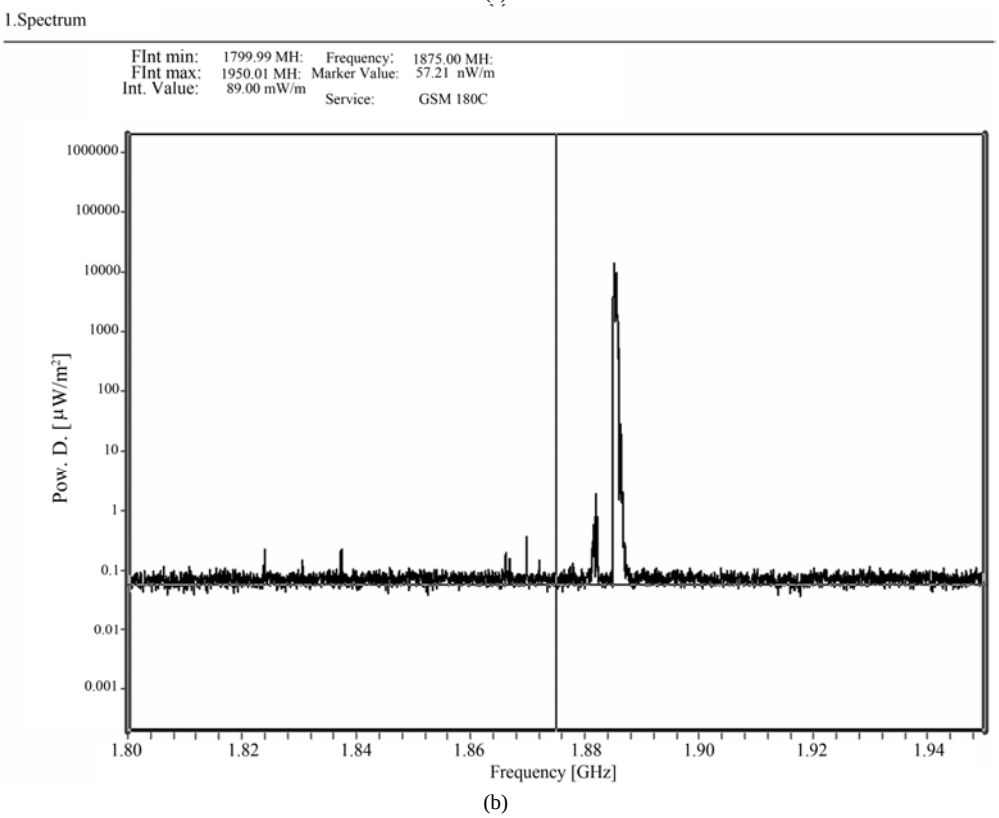


(b)

**Figure 5. (a) A typical spectrum analysis of magnetic component of microwaves emitted by a cordless Brondi DC3010, acquired by Narda SRM 3000. (b) A typical spectrum analysis of power density of microwaves emitted by a cordless Brondi DC3010, acquired by Narda SRM 3000.**

 

rally lesser than that produced by mobile phones batteries. This may be wrongly interpreted by users as a lack of warning about eventual long-term effects on health.

## 4. Conclusions

This brief study has provided measuring methods to quantify high frequency electromagnetic radiation levels coming from artificial sources in a typical house. Spectrum and time analysis modes performed on mobile phones microwaves showed that the limits recommended by the I.C.N.I.R.P. can be exceeded during a conversation, depending on the distance of the user from the local base station. Analogue measures relative to high frequencies radiations of some cordless telephones evidenced microwave radiation emissions in a narrow band close to 1900 MHz, within those suggested exposure limits. Spectrum analysis performed on some working microwave ovens showed a large frequency range exposure from 2400 to 2500 MHz, not exceeding the limits recommended by some international guidelines. Nevertheless such result can not be considered negligible. Our measurements and other previous studies performed so far suggest to monitor RF-MW intensities in our living environment. However, further research is needed to find reliable protective effectiveness relative to high frequencies home devices.

## REFERENCES


[1] T. Q. Huang, M. S. Lee, E. Oh, B. T. Zhang, J. S. Seo and W. Y. Park, "Molecular Responses of Jurkat T-Cells to 1763 MHz Radiofrequency Radiation," *International Journal of Radiation Biology*, Vol. 84, No. 9, 2008, pp. 734-741.

[2] K. Makker, A. Varghese, N. R. Desai, R. Mouradi and A. Agarwal, "Cell Phones: Modern Man's Nemesis?" *Reproductive Biomedicine Online*, Vol. 18, No. 1, 2009, pp. 148-157.

[3] Scientific Committee on Emerging and Newly Identified Health Risks (SCENIHR), "Possible Effects of Electromagnetic Fields (EMF) on Human Health," 21 March 2007.

[4] G. J. Hyland, "Physics and Biology of Mobile Telephony," *The Lancet*, Vol. 356, No. 9244, 2000, pp. 1-8.

[5] T. A. Marks, C. C. Ratke and W. O. English, "Strai voltage and Developmental, Reproductive and Other Toxicology Problems in Dogs, Cats and Cows: A Discussion," *Vet Hum Toxicol*, Vol. 37, No. 2, 1995, pp. 163-172.

[6] W. Löscher and G. Käs, "Conspicuous Behavioural Abnormalities in a Dairy Cow Herd near a TV and Radio Transmitting Antenna," *Practical Veterinary surgeon*, Vol. 29, No. 5, 1998, pp. 437-444.

[7] R. C. Beasond and P. Semm, "Responses of Neurons to an Amplitude Modulated Microwave Stimulus," *Neuroscience Letters*, Vol. 333, No. 3, 2002, pp. 175-178.

[8] H. Lai , A. Horita, C. K. Chou and A. W. Guy, "Low-level Microwave Irradiation Affects Central Cholinergic Activity in the Rat," *J. Neurochem.* Vol. 48, 1987, pp. 40-45

[9] G. Thuroczy, I. Hernadj and L. Kelleny, "Activity and Learning Memory Task of the Rat," *Bioelectromagnetics*, Vol. 27, 2001.

[10] K. Fritze, C. Sommer, B. Schmitz, G. Mies, K. Hossman, M. Kiessling *et al.*, "Effect of Global System for Mobile Communication (GSM) Microwave Exposure on Blood-Brain Barrier Permeability in Rat," *Acta Neuropathol* (Berlin), Vol. 94, No. 5, 1997, pp. 465-470.

[11] F. Töre, P. E. Dulou, E. Haro, B. Veyret and P. Aubineau, "Two-hour Exposure to 2 W/kg, 900 MHz GSM Microwaves Induces Plasma Protein Extravasation in Rat Brain," In: Proceedings from the 5th Int. Congress of the European Bioelectromagnetics Association, 6 September 2001. *Finnish Institute of Occupational Health*, Helsinki , 2001, pp. 43-45.

[12] L. G. Salford, A. E. Brun, J. L. Eberhardt, L. Malmgren and B. R. Persson, "Nerve Cell Damage in Mammalian Brain after Exposure to Microwaves from GSM Mobile Phones," *Environmental Health Perspectives*, Vol. 111, No. 7, 2003, pp. 881-883.

[13] A. Karinen, S. Heinävaara, R. Nylund and D. Leszczynski, "Mobile Phone Radiation Might Alter Protein Expression in Human Skin," *BMC Genomics*, 2008.

[14] E. Calabrò, S. Condello, M. Currò, N. Ferlazzo, D. Caccamo, S. Magazù and R. Ientile, "Modulation of HSP Response in SH-SY5Y Cells Following Exposure to Microwaves of a Mobile Phone," submitted, 2010.

[15] I. Y. Belyaev, C.B. Koch, O. Terenius, K. Roxstrom-Lindquist, L.O. Malmgren, W.H. Sommer, L.G. Salford and B.R. Persson, "Exposure of Rat Brain to 915MHz GSM Microwaves Induces Changes in Gene Expression but not Double Stranded DNA Breaks or Effects on Chromatin Conformation," *Bioelectromagnetics*, Vol. 27, No. 4, 2006, pp. 295-306.

[16] E. Diem, C. Schwarz, F. Adlkofer, O. Jahn and H. Rudiger, "Non-thermal DNA Breakage by Mobile-Phone Radiation (1800MHz) in Human Fibroblasts and in Transformed GFSH-R17 Rat Granulosa Cells *in vitro*," *Mutation Research*, Vol. 583, No. 2, 2005, pp. 178-183.

[17] R. R. Tice, G. G. Hook, M. Donner, D. I. McRee and A. W. Guy, "Genotoxicity of Radiofrequency Signals. Investigation of DNA Damage and Micronuclei Induction in Cultured Human Blood Cells," *Bioelectromagnetics*, Vol. 23, No. 2, 2002, pp. 113-126.

[18] International Commission on Non-Ionizing Radiation Protection, "Guidelines for Limiting Exposure to Time-Varying Electric, Magnetic, and Electromagnetic Fields (up to 300 GHz)," *Health Physics*, Vol. 74, No. 4, 1998, pp. 494-522.


 

Call for Papers


# Journal of Electromagnetic Analysis and Applications

ISSN: 1942-0730 (Print), 1942-0749 (Online)
www.scirp.org/journal/jemaa

Journal of Electromagnetic Analysis and Applications(JEMAA) is a professional journal in the field of electromagnetic analysis, testing and application. The goal of this journal is to provide an international platform for engineers and academicians all over the world to promote, share, and discuss various new issues and developments in the field of electromagnetic. This journal is edited to encourage deeper understanding and greater effectiveness in theory analysis, testing, numerical calculation and engineering application that relevant electromagnetic fields.

## Editors-in-Chief



## Subject Coverage

JEMAA publishes four categories of original technical reports: papers, communications, reviews, and discussions. Papers are well-documented final reports of research projects. Communications are shorter and contain noteworthy items of technical interest or ideas required rapid publication. Reviews are synoptic papers on a subject of general interest, with ample literature references, and written for readers with widely varying background. Discussions on published reports, with author rebuttals, form the fourth category of JEMAA publications. Topics of interest include, but are not limited to:

- Electromagnetic Numerical Analysis
- Multiphysics Coupled Problems
- Electromagnetic Inverse Problems
- Electromagnetic Structure Optimization
- Test Electromagnetic Analysis Method
- Workshop Benchmark Problems
- Electromagnetic Devices
- Electromagnetic Compatibility
- Electromagnetic Nondestructive Testing
- Electromagnetic Material Modelling

## Notes for Intending Authors

Submitted papers should not be previously published nor be currently under consideration for publication elsewhere. Paper submission will be handled electronically through the website. All papers will be peer reviewed. For more derails about the submissions, please access the website.

## Website and E-Mail

http://www.scirp.org/journal/jemaa jemaa@scirp.org

*J. Electromagnetic Analysis & Applications*, 2010, 2, 513-579
Published Online September 2010 in SciRes (http://www.SciRP.org/journal/jemaa)

# TABLE OF CONTENTS

**Volume 2 Number 9** **September 2010**



 